

## ABSTRACT

Title of thesis:       Simulation of Coaxial Rotor  
                          Interactional Aerodynamics  
                          using Coupled CFD-CSD

Bradley Passe, Masters of Science, 2015

Thesis directed by:  Dr. James Baeder  
                          Department of Aerospace Engineering

Performance and range requirements for next-generation rotary-wing aircraft have sparked renewed interests in the coaxial rotor configuration, augmented with lift and/or thrust compounding. Often, thrust augmentation is provided in the form of a propeller or jet engine to counteract the airframe and rotor drag in high speed forward flight. A notional X2TD coaxial compound configuration has been chosen to perform numerical simulations in forward flight with CFD-CSD coupling. The delta loose coupling method is used to couple the CFD and CSD models. Using the CFD results to correct the reduced order aerodynamics in this loose coupling framework will drive toward a deeper understanding of rotor-rotor and rotor-fuselage interactions in the forward flight regime. Using unrestricted data of the X2TD flight test program the in-house CSD code (PRASADUM) was validated against both CAMRAD II and flight test data results. Helios, using both OVERFLOW and NSU3D as near-body solvers was used as the CFD solver for the CFD-CSD coupling framework. The CFD-CSD coupling framework was used for several key

flight conditions of the X2TD, namely 55, 100, and 150 knots. A comparison study at both 55 and 150 knots was conducted between an isolated coaxial rotor system case, and 3 other cases incorporating three different fuselage models to the CFD analysis: a simple fuselage body, a complex fuselage body containing horizontal and vertical stabilizers, and lastly the complex fuselage body with the added inclusion of the rotor mast.

Simulation of Coaxial Rotor  
Interactional Aerodynamics using Coupled CFD-CSD

by

Bradley Passe

Thesis submitted to the Faculty of the Graduate School of the  
University of Maryland, College Park in partial fulfillment  
of the requirements for the degree of  
Masters of Science  
2015

Advisory Committee:  
Dr. James Baeder, Chair/Advisor  
Dr. Inderjit Chopra  
Dr. Christopher Cadou

© Copyright by  
Bradley Passe  
2015

## Acknowledgments

I want to thank my advisor, Dr. James Baeder, for giving me the opportunity to pursue meaningful academic research and for providing me with a wonderful educational experience. He has been an invaluable mentor and I enjoyed the countless discussions regarding contemporary issues in both CFD and rotorcraft fields; as well as his steady guidance and insight with navigating through various research problems that arose while completing this work. I would also like to thank my thesis committee members, Dr. Christopher Cadou and Dr. Inderjit Chopra, for spending time to serve on my committee and for their feedback on my research. I also want to thank Dr. Rajneesh Singh, the Army Research Lab , and NASA Ames CREATE AV: Helios Team, for providing their computational resources as well as technical guidance and personal time. It was instrumental in allowing me to finish this research project as thoroughly as possible and on time.

To both my friends and fellow colleagues, thank you for helping to guide and advise me through these past two years of graduate school in both an academic and personal way. Lastly, I want to thank my parents as I would not have gotten to this point without their constant encouragement and support.

# Table of Contents

List of Tables	v
List of Figures	vi
1 Introduction	1
1.1 Motivation and Literature Review . . . . .	1
1.2 Thesis Contributions . . . . .	10
1.3 Scope and Organization of Thesis . . . . .	12
2 CFD-CSD Framework Theory and Methodology	14
2.1 Overview . . . . .	14
2.2 CFD Methodology . . . . .	14
2.2.1 Off-Body Solver . . . . .	15
2.2.2 Near-Body Solvers . . . . .	16
2.2.3 Framework Integration . . . . .	17
2.3 CFD Numerical Modeling and Theory . . . . .	18
2.3.1 Governing Equations . . . . .	18
2.3.2 Non-Dimensionalization . . . . .	22
2.3.3 RANS Model . . . . .	23
2.4 CSD Methodology and Theory . . . . .	24
2.4.1 CSD Aerodynamic Models . . . . .	25
2.4.2 CSD Trim Analysis . . . . .	26
2.5 CFD-CSD Coupling . . . . .	28
3 Notional X2 Model Validation	33
3.1 Overview . . . . .	33
3.2 Notional X2 Vehicle Configuration . . . . .	34
3.2.1 Vehicle Layout . . . . .	37
3.2.2 Main Rotor Blade Structural Properties . . . . .	41
3.2.3 Main Rotor Design . . . . .	44
3.2.4 2D Aerodynamic Look up Tables . . . . .	46
3.3 CSD Code Notional X2 Model Validation . . . . .	47

3.4	Notional X2 Model CFD Implementation . . . . .	51
3.4.1	Structured Blade Grid Generation . . . . .	51
3.4.2	Unstructured Fuselage Grid Generation . . . . .	53
3.4.3	Overset Meshing, Co-ordinate System, and Sign Conventions .	57
4	Forward Flight Results: Isolated Rotor System	63
4.1	Overview . . . . .	63
4.2	55 Knots . . . . .	64
4.3	100 Knots . . . . .	79
4.4	150 Knots . . . . .	93
4.5	Airspeed Trends . . . . .	106
4.6	Rotor-Rotor Interference: Single vs Coaxial . . . . .	109
4.7	Hubloads . . . . .	118
5	Forward Flight Results: Rotor System And Fuselage	121
5.1	Overview . . . . .	121
5.2	55 Knots Comparison . . . . .	122
5.3	150 Knots Comparison . . . . .	129
6	Conclusion	135
6.1	Summary . . . . .	135
6.2	Observations . . . . .	138
6.3	Contributions . . . . .	141
6.4	Recommendations . . . . .	143
	Bibliography	146

## List of Tables

1.1	Comparison of X2TD and XH-59A aircraft and rotor properties (Ref. [4]) . . . . .	7
3.1	Notional X2 Vehicle Configuration . . . . .	37
3.2	Notional X2 model airfoil cross sections . . . . .	45
3.3	Fine level Cartesian Off-body domain extents in units of blade root chord lengths . . . . .	58
3.4	Deformed frame aerodynamic loads: sign convention . . . . .	62
4.1	Comparison between initial CSD and CFD-CSD trim solutions at 55 knots . . . . .	65
4.2	Comparison between initial CSD and CFD-CSD trim solutions at 100 knots . . . . .	80
4.3	Comparison Between Initial CSD And CFD-CSD Trim Solutions At 150 Knots . . . . .	93
5.1	Comparison of trim controls between isolated coaxial rotor and rotor + fuselage cases at 55 knots . . . . .	123
5.2	Comparison of integrated quantities between isolated coaxial rotor and rotor + fuselage cases At 55 knots . . . . .	124
5.3	Comparison of trim controls between isolated coaxial rotor and rotor + fuselage cases at 150 knots . . . . .	129
5.4	Comparison of integrated quantities between isolated coaxial rotor and rotor + fuselage cases at 150 knots . . . . .	130



## List of Figures

1.1	Illustration of various physical and engineering problems imposing limitations on conventional helicopter design (Ref. [25]) . . . . .	2
1.2	Illustration of advancing blade concept and its advantageous lift distribution over conventional single rotor (Ref. [9]) . . . . .	3
1.3	Underestimation of ABC rotor power factor at low speed (Ref. [9]) . . . . .	5
1.4	XH-59A and X2TD (Ref. [33]) . . . . .	6
1.5	Comparison of XH-59A and X2TD blade planform shape (Ref. [4]) . . . . .	9
2.1	CSD solver global flow chart . . . . .	26
2.2	CSD solver rotorcraft trim flow chart . . . . .	27
2.3	CSD solver rotorcraft aero-trim coupling flow chart . . . . .	27
2.4	CFD-CSD loose coupling flow chart . . . . .	30
3.1	Sikorsky X2TD vehicle configuration and auxiliary propeller (Ref. [5]) . . . . .	34
3.2	Sikorsky X2TD power curves for flight tests normalized to 4,000 ft density altitude (Ref. [5]) . . . . .	35
3.3	X2TD variation of rotor-rotor tip clearance and LOS with airspeed (Ref. [5]) . . . . .	36
3.4	Three notional X2 fuselage CAD models . . . . .	40
3.5	Notional X2 main rotor fan plot . . . . .	42
3.6	Notional X2 main rotor blade structural frequencies . . . . .	43
3.7	X2TD main rotor blade geometry implemented into notional X2 model (Ref. [4]) . . . . .	44
3.8	UH-60 main rotor power required at 3,670 ft density altitude . . . . .	48
3.9	UH-60 predicted $C_n M^2$ from Run 45, Point 37 . . . . .	48
3.10	Prescribed LOS control vs. X2TD flight test . . . . .	49
3.11	Predicted Propeller Power vs. Forward Speed . . . . .	50
3.12	Predicted Total Rotor Power vs. Forward Speed . . . . .	51
3.13	Notional X2 O-O blade mesh . . . . .	52
3.14	Example of prismatic boundary layer cell growth off body surface . . . . .	55
3.15	Unstructured simple fuselage mesh . . . . .	55
3.16	Unstructured complex fuselage mesh . . . . .	56
3.17	Unstructured complex fuselage with mast mesh . . . . .	57

3.18	Comparison between X2TD and CFD notional X2 model . . . . .	59
3.19	CFD overset mesh system for notional X2 . . . . .	61
3.20	Blade Airloads co-ordinate system . . . . .	62
4.1	Predicted vs. measured coaxial rotor power for the Sikorsky X2 . . .	64
4.2	Convergence of rotor controls (deg) with CFD-CSD iterations at 55 knots . . . . .	67
4.3	Convergence Of $C_C M^2$ at 55 Knots . . . . .	68
4.4	Convergence Of $C_n M^2$ at 55 Knots . . . . .	69
4.5	Convergence Of $C_m M^2$ at 55 Knots . . . . .	70
4.6	Contour plots of $C_c M^2$ for initial CSD and final CFD-CSD at 55 knots	72
4.7	Contour plots of $C_n M^2$ for initial CSD and final CFD-CSD at 55 knots	73
4.8	Contour plots of $C_m M^2$ for initial CSD and final CFD-CSD at 55 knots	74
4.9	Line plots of $C_C M^2$ between initial CSD and final CFD-CSD at 55 knots . . . . .	76
4.10	Line plots of $C_n M^2$ between initial CSD and final CFD-CSD at 55 knots . . . . .	77
4.11	Line plots of $C_m M^2$ between initial CSD and final CFD-CSD at 55 knots . . . . .	78
4.12	Convergence of rotor controls (deg) with CFD-CSD iterations at 100 Knots . . . . .	81
4.13	Convergence of $C_c M^2$ at 100 knots . . . . .	82
4.14	Convergence of $C_n M^2$ at 100 knots . . . . .	83
4.15	Convergence of $C_m M^2$ at 100 knots . . . . .	84
4.16	Contour plots of $C_c M^2$ for initial CSD and final CFD-CSD at 100 knots	86
4.17	Contour plots of $C_n M^2$ for initial CSD and final CFD-CSD at 100 knots . . . . .	87
4.18	Contour plots of $C_m M^2$ for initial CSD and final CFD-CSD at 100 knots . . . . .	88
4.19	Line plots of $C_c M^2$ between initial CSD and final CFD-CSD at 100 knots . . . . .	90
4.20	Line plots of $C_n M^2$ between initial CSD and final CFD-CSD at 100 knots . . . . .	91
4.21	Line plots of $C_m M^2$ between initial CSD and final CFD-CSD at 100 knots . . . . .	92
4.22	Convergence Of Rotor Controls (deg) With CFD-CSD Iterations At 100 Knots . . . . .	94
4.23	Convergence of $C_c M^2$ at 150 Knots . . . . .	95
4.24	Convergence of $C_n M^2$ at 150 Knots . . . . .	96
4.25	Convergence of $C_m M^2$ at 150 Knots . . . . .	97
4.26	Contour plots of $C_c M^2$ for initial CSD and final CFD-CSD at 150 knots	99
4.27	Contour plots of $C_n M^2$ for initial CSD and final CFD-CSD at 150 knots . . . . .	100
4.28	Contour plots of $C_m M^2$ for initial CSD and final CFD-CSD at 150 knots . . . . .	101

4.29	Line plots of $C_c M^2$ between initial CSD and final CFD-CSD at 150 knots . . . . .	103
4.30	Line plots of $C_n M^2$ between initial CSD and final CFD-CSD at 150 knots . . . . .	104
4.31	Line plots of $C_m M^2$ between initial CSD and final CFD-CSD at 150 knots . . . . .	105
4.32	$C_n M^2$ for upper rotor (CCW) at advance ratios of $\mu = 0.15, 0.27,$ and $0.41$ . . . . .	107
4.33	$C_n M^2$ for lower rotor (CW) at advance ratios of $\mu = 0.15, 0.27,$ and $0.41$ . . . . .	107
4.34	$C_m M^2$ for upper rotor (CCW) at advance ratios of $\mu = 0.15, 0.27,$ and $0.41$ . . . . .	108
4.35	$C_m M^2$ for lower rotor (CW) for advance ratios $\mu = 0.15, 0.27,$ and $0.41$	108
4.36	Isolated rotors vs. coaxial: comparison of $C_c M^2$ at 55 knots . . . . .	111
4.37	Isolated rotors vs. coaxial: comparison of $C_n M^2$ at 55 knots . . . . .	112
4.38	Isolated rotors vs. coaxial: comparison of $C_m M^2$ at 55 knots . . . . .	113
4.39	Isolated rotors vs. coaxial: comparison of $C_c M^2$ at 150 knots . . . . .	115
4.40	Isolated rotors vs. coaxial: comparison of $C_n M^2$ at 150 knots . . . . .	116
4.41	Isolated rotors vs. coaxial: comparison of $C_m M^2$ at 150 knots . . . . .	117
4.42	Centerline vorticity magnitude and wake structure at $\mu = 0.15$ (left) and $\mu = 0.41$ (right) . . . . .	118
4.43	Comparison of 4/rev hub loads (lb, ft-lb) : initial CSD vs. CFD-CSD	119
4.44	Comparison of 8/rev hub loads (lb, ft-lb) : initial CSD vs. CFD-CSD	119
5.1	Line plots of $C_c M^2$ between isolated coaxial rotor and rotor + fuselage cases at 55 knots . . . . .	126
5.2	Line plots of $C_n M^2$ between isolated coaxial rotor and rotor + fuselage cases at 55 knots . . . . .	127
5.3	Line plots of $C_m M^2$ between isolated coaxial rotor and rotor + fuselage cases at 55 knots . . . . .	128
5.4	Line plots of $C_c M^2$ between isolated coaxial rotor and rotor + fuselage cases at 150 knots . . . . .	132
5.5	Line plots of $C_n M^2$ between isolated coaxial rotor and rotor + fuselage cases at 150 knots . . . . .	133
5.6	Line plots of $C_m M^2$ between isolated coaxial rotor and rotor + fuselage cases at 150 knots . . . . .	134

## List of Symbols and Abbreviations

$C_c M^2$	non dimensional deformed frame chordwise force
$c_d$	coefficient of drag for airfoil
$c_l$	coefficient of lift for airfoil
$c_m$	moment coefficient for airfoil
$C_m M^2$	non dimensional deformed frame pitching moment
$C_n M^2$	non dimensional deformed frame normal force
$c/R$	non dimensional blade chord to radius ratio
$e$	Internal Energy
$E$	Kinetic Energy
$F, G, H$	Flux Vectors
$\gamma$	ratio of specific heats
$M$	Mach Number
$\mu$	Ratio of forward speed to rotor tip speed
$P$	Pressure
$Pr$	Prandtl Number
$\psi$	Rotor azimuth angle
$Q$	Vector of Conserved Variables
$r/R$	Non dimensional blade radial station
$R$	Rotor Radius
$Re$	Reynolds Number
$/rev$	Per rotor revolution
$\rho$	Density
$t/c$	non dimensional airfoil thickness to chord ratio
$u, v, w$	Cartesian flow velocity components
ABC	Advancing Blade Concept
Advance Ratio	Ratio of forward speed to rotor tip speed
AMR	Adaptive Mesh Refinement
CCW	Counter Clockwise Rotation
CW	Clockwise Rotation
CFD	Computational Fluid Dynamics
Coaxial Rotor	Upper and lower Rotor that rotate in opposite directions to each other
CSD	Computational Structural Dynamics
FET	Finite Element in Time
FVL	Future Vertical Lift Program
GRP	Sikorsky Generalized Rotorcraft Performance Methodology
HPC	High Performance Computing systems or clusters
I/O	Input, Output File transfer
JMR	Joint Multi-Role Technical Demonstrator Program
LE	Leading Edge of a wing or airfoil
LES	Large Eddy Simulations
LOS	Lift Offset is lateral displacement of lift vector from hub center line
M	Mach Number
RANS	Reynolds-Averaged Navier-Stokes
rpm	revolutions per minute
SA	Spalart-Allmaras
Solidity	Ratio of blade area to rotor disk area
TE	Trailing Edge of a wing or airfoil
X2TD	X2 Technology Demonstrator

## Chapter 1: Introduction

### 1.1 Motivation and Literature Review

The conventional single main rotor with tail rotor helicopter was initially conceptualized as a vehicle capable of vertical flight with limited forward flight capabilities. To expand its flight envelope to larger maximum top speeds, significant design changes are necessary to work around the limiting physical phenomena of compressibility effects on the advancing side and blade stall on the retreating side of the rotor disk( see Fig. 1.1). To maintain trimmed steady forward flight at large advance ratios, the blades on the advancing and retreating sides operate at severely compromised conditions. Beyond a certain advance ratio, trim might still be possible but excessive vibrations impose additional barriers to achieving higher forward speed. These two issues were a key barrier in realizing high speed forward flight.

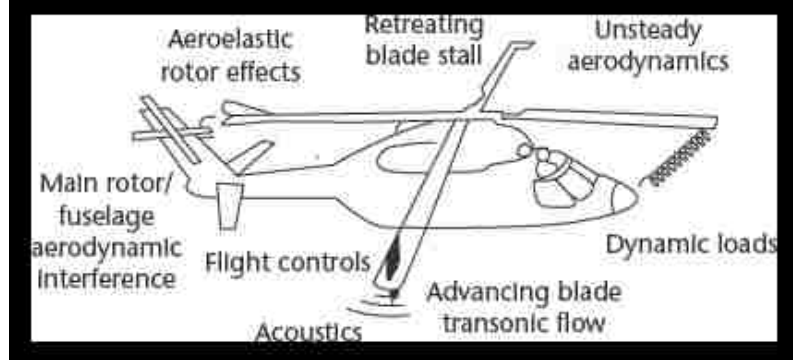


Figure 1.1: Illustration of various physical and engineering problems imposing limitations on conventional helicopter design (Ref. [25])

## Development of the ABC Rotor

Sikorsky (Ref. [8] [26]) attempted to solve this problem with the Advancing Blade Concept (ABC) in the 1970's. The ABC rotor system is a stiff, rigid coaxial rotor configuration as seen in Fig. 1.2. To solve the retreating side blade stall and still maintain vehicle roll moment balance in level flight, a coaxial rotor system forms the basis of the ABC rotor. The ABC gets its name from leveraging the significant rotor lift available on the advancing side of the rotor disk at high speeds. With two counter-rotating rotors, the retreating sides of each rotor are offloaded and the lift is generated on the respective advancing sides. This allows the vehicle to exploit the large dynamic pressures that exist on the advancing sides while simultaneously maintaining roll moment balance. Since the retreating sides of each rotor are no longer required to produce thrust, the advancing sides can operate at optimal angles of attack. Of course, a consequence of this rotor design is that increased lift on the advancing sides causes each rotor to have increasing individual roll moments. To

avoid having these large rolling moments causing the tips of the upper and lower rotor blades to hit each other, the blades are designed to be significantly stiffer than conventional helicopter blades.

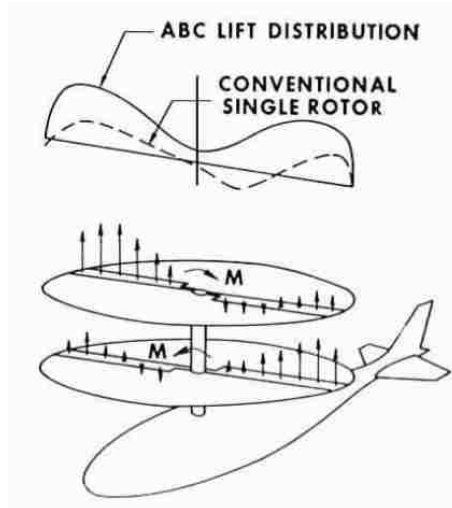


Figure 1.2: Illustration of advancing blade concept and its advantageous lift distribution over conventional single rotor (Ref. [9])

A secondary consequence of using a coaxial main rotor system is the elimination of a tail rotor, as two counter-rotating main rotors can provide torque balance and yaw control. This reduction in empty weight allows for propulsive thrust augmentation, which can then solve the advancing blade compressibility problem by alleviating the rotor thrust requirements at high forward speeds. As the forward flight speed increases, compressibility and transonic effects become prominent on the advancing sides of the rotors. This phenomena can cause flow separation on the airfoils, dynamic stall events, as well as high vibratory loads. To avoid this from occurring, instead of having the rotor as the primary provider for both lift and propulsive thrust, the rotor can be complimented with either a jet engine or a

propeller to provide extra propulsive thrust. This allows the rotor to share significantly less of the propulsive thrust required for the vehicle. Further more, it allows for the rotors rotational speed to be slowed down at high forward speeds to avoid running into sonic conditions on the advancing side blades. Thus, similarly to fixed wing vehicles, the ABC rotors flight envelope is now only limited by two quantities: available power and structural load limits of the blades (Ref. [8]).

## First Experiments and Research of Coaxial Rotor Helicopters

Research on coaxial designs in the USA, was first started in the 1950's with the experimental measurements of the Harringtons scaled rotors in the Langley full scale wind tunnel (Ref. [9]). These experiments focused on hover performance of coaxial designs. Sikorsky, beginning in 1965, started preliminary research into the ABC rotor system, a coaxial rotor design (Ref. [9]). This eventually led to the development of the XH-59A test program. The XH-59A rotor was tested in the NASA Ames (40 x 80 ft) wind tunnel, which covered flight conditions from 0.21 to 0.91 advance ratio (Refs. [22], [7]). Subsequently, flight tests of the XH-59A were also conducted (Ref. [9]) and it was found that scale model predictions were significantly different from actual flight. This was due to the deficiency in predictive capabilities used for performance analysis. The Glauert type correction term used to define the inflow variation was severely underestimated as seen in Fig. 1.3 (Ref. [9]).

After pure helicopter mode flight testing, the XH-59A then added two turbojet engines for thrust compounding in high speed flight. The investigations and



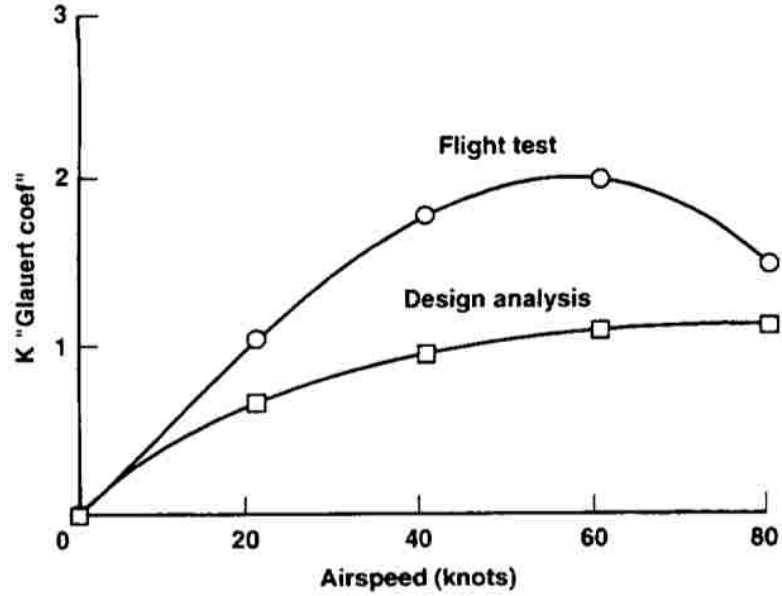


Figure 1.3: Underestimation of ABC rotor power factor at low speed (Ref. [9])

subsequent analysis of the XH-59A primarily focused on integrated rotor loads and performance metrics (Refs. [22], [7]) and less investigation of interactional aerodynamics and blade loading distributions. While the compound coaxial aircraft configuration was realized, the XH-59A never became a production aircraft due to heavy vibrations, drive train complexities, and lack of market interest.

It was Sikorsky again, after several decades, that revisited the ABC concept and built the X2 Technology Demonstrator (X2TD), a modern compound coaxial rotorcraft. Using experimental data and lower order model correlation results from the XH-59A, a redesign and optimization of the ABC concept was completed and culminated in the X2TD aircraft. This vehicle underwent its own flight test program (Refs. [32], [33]). There were many lessons learned from the XH-59A test program that made its way into the design of the X2TD. From a dynamics perspective, the XH-59A had very high vibrations. Of special note was the 3/rev cockpit vibration

at high speeds (Ref. [5]). The X2TD design incorporated active vibration control, and switched to a 4 bladed configuration to eliminate 3/rev rotor excitation (Refs. [4], [5]). The XH-59A also had high fuel consumption, low rotor efficiency, and issues varying rotor rpm at high speeds (Ref. [4]). The X2TD program set out to mitigate and or eliminate the deficiencies discovered in the XH-59A program, as well as introduce modern analysis and design into the ABC concept. Pictures of these two aircraft can be seen in Fig. 1.4.



(a) XH-59A in flight



(b) X2TD in flight

Figure 1.4: XH-59A and X2TD (Ref. [33])

## Modern Coaxial Rotor Helicopter Design

The X2TD is a smaller and lighter aircraft than its predecessor and is a 4 bladed coaxial design instead of the previous 3 bladed. The X2TD also used a

propeller for auxiliary propulsion instead of the twin turbojet engine design of the XH-59A. A single engine drives the main rotors and the propeller (Ref. [4]). A comparison illustrating differences in rotor design between the X2TD and XH-59A is shown in Table 1.1.

Attribute	XH-59A	X2TD
<b>GW</b> ( <i>lb</i> )/Accommodation	13,300/ 2 Side-by-side	5,3000/ 2 Tandem
<b>R</b> ( <i>ft</i> )	18.0	13.2
<b>Nb</b> / $\sigma$ <b>TW</b> (Total)	3 + 3 / 0.1275	4 + 4 / 0.1441
<b>DL</b> ( <i>lb/ft<sup>2</sup></i> )	13.07	11.14
<b>Hub Type</b>	Rigid Coaxial (upper CCW)	Rigid Coaxial (upper CCW)
<b>Vtip</b> ( <i>ft/s</i> )	650.0	620.45
<b>M</b> (Adv. Lmt.)	0.85 (0.95 achieved)	0.9
<b>Power Plant</b> (s)	2 P&W J60-P-3A (6,600lb T) 1 P&W PT6t-3 Twin Pack ( 1,600 shp)	LHTEC T800-LHT-801( 1,452 shp)

Table 1.1: Comparison of X2TD and XH-59A aircraft and rotor properties (Ref. [4])

While the X2TD was a coaxial helicopter configuration, Sikorsky used their GRP methodology for the X2TD main rotor design which could not simulate coaxial designs (Ref. [4]). This limitation meant that the aerodynamic design of the X2TD main rotors was done simulating it as a single coplanar rotor configuration. Further, during the design stage, Sikorsky was unable to simulate or account for rotor-rotor interference (Ref. [4]).

Starting from a scaled XH-59A as a baseline, it became apparent that an evolutionary rotor blade design was required. The scaled XH-59A blade was found to suffer from high profile losses on the retreating side, as well as some compressibility

issues for the high speed envelope of the X2TD vehicle (Ref. [4]). A prominent suggestion from previous XH-59A studies that made its way into the new X2TD blade was the use of double ended elliptically shaped airfoils at the root sections, to decrease the high profile losses these sections suffered on the retreating side during XH-59A tests. Therefore, the X2TD main rotor blades transition from double ended airfoils at the root sections, to modern sharp trailing edge high lift airfoils, to transonic airfoil sections at the tip of the blade.

Aside from this variation in airfoil geometry, the X2TD also possesses a unique twist distribution. All modern conventional helicopters have a negative twist gradient along the span due to its superior increase in rotorcraft performance. The X2TD, however, has a positive twist gradient over the inner 40% of the blade before reverting to the classical negative twist gradient all the way out to the tip. The reason for having the positive twist gradient in the inboards sections was to alleviate the negative lift and high profile drag in the reverse flow regions (Ref. [4]). The positive twist gradient achieved this by lowering the angle of incidence of the airfoil shapes to the local flow velocities (Ref. [4]).

The X2TD blade planform was generated from iterative parametric studies off of a scaled XH-59A and is shown in Fig. 1.5. The target of the blade planform was to maintain the same rotor solidity but maximize lift and minimize drag. It was found that shifting the blade area from the root sections more toward the outer parts of the blade planform accomplished this goal and consequently the X2TD blade took on a more elliptical shape (Ref. [4]).

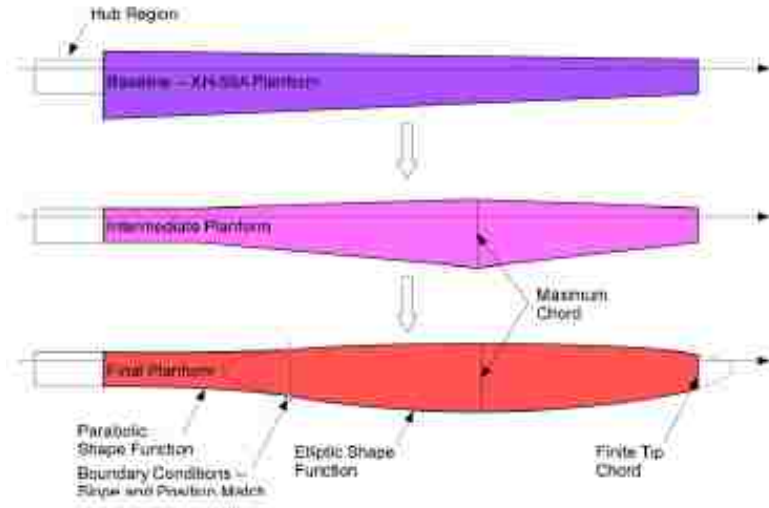


Figure 1.5: Comparison of XH-59A and X2TD blade planform shape (Ref. [4])

When designing the X2TD main rotors, lower order models and methods were used and while consideration of both aerodynamic and structural criteria occurred, the detailed interactional aerodynamics was not simulated, studied, or used during the design phase. As a consequence, much of the literature focuses on integrated performance metrics of the X2TD design. After successful flight tests, (Ref. [33]) investigative work has been done by some authors to go back and look at interactional aerodynamics and its effect on blade vibratory loads.

While most of these studies, such as (Ref. [36]) used rotorcraft comprehensive analysis codes with 2D aerodynamic table look ups and linear inflow models, some have looked at ABC helicopter designs using a free wake model (Ref. [17]). These studies focused on the rotor systems and global design trends for airloads and structural loads based on lift offset and blade planform shape. They did not attempt to quantify interactional aerodynamics and its role in aerodynamic loads. High fidelity

CFD analysis of coaxial helicopter designs has been performed for hover (Ref. [18]), however there is a considerable lack of publications focusing on the forward flight regime. Some work was done looking at a compound coaxial helicopter configuration at Glasgow University (Ref. [17]), however the work completed was a hybrid design of the XH-59A and X2TD aircraft and did not attempt to benchmark to any flight test data. While interactions between the rotors, fuselage, and propeller were studied, the nature of the free wake code only led to a lower order approximation of the phenomena and inherently can not capture the complex viscous interactions and phenomena that are the primary physical mechanisms behind component interactions and their effects on blade aerodynamic loads.

## 1.2 Thesis Contributions

The purpose of this thesis is to explore in greater detail the interactional effects of coaxial compound rotorcraft using CFD-CSD coupling, specifically focusing on rotor-rotor and rotor-fuselage aerodynamic interference in forward flight. By using high fidelity CFD coupled with a structural dynamics model, the fluid-structure interactions can be captured with a method closer to a first principles basis. Further, the direct effect on vehicle integrated performance, trim condition, and blade aerodynamic loading can be analyzed.

In order to provide reliable and believable data and results, a coaxial compound rotorcraft vehicle configuration for this study should match as closely as possible a current real world design. Further, the framework should be able to match closely

any available flight test data in public domain. For these reasons, a notional X2TD coaxial compound configuration has been chosen to perform numerical simulations in forward flight with CFD-CSD coupling. The delta loose coupling method is used to couple the CFD and CSD models. Using the CFD results to correct the reduced order aerodynamics in this loose coupling framework will drive toward a deeper understanding of rotor-rotor and rotor-fuselage interactions in the forward flight regime.

Using unrestricted data of the X2TD flight test program (Ref. [32]), the in-house CSD code (PRASADUM) was validated against both CAMRAD II (Ref. [15]) and flight test data results for integrated performance metrics. Helios, using both OVERFLOW and NSU3D as near-body solvers (Refs. [6] [31] [20]) was used as the CFD solver for the CFD-CSD coupling framework. The CFD-CSD coupling framework was used for several key flight conditions of the X2TD, namely 55, 100, and 150 knots. A comparison study at 150 knots was conducted between an isolated coaxial rotor system case, and 3 other cases incorporating three different fuselage models to the CFD analysis: a simple fuselage body, a complex fuselage body containing horizontal and vertical stabilizers, and lastly the complex fuselage body with the added inclusion of the rotor mast.

The contributions of this work is to provide a robust CFD-CSD framework for further analysis of ABC helicopter vehicle designs as well as further the understanding of the complex aerodynamic environment the vehicle operates in during forward flight. This work will contribute to the analysis of rotor-rotor and rotor-fuselage interactional aerodynamics and its impact on blade aerodynamic loading. By con-

ducting this study using a notional X2 based on available public domain data of X2TD, this work can be further expanded, and validated against real world results by other researchers, making this a significant contribution to the advancement of the field by providing both a numerical framework as well as a vehicle configuration for continuing study.

### 1.3 Scope and Organization of Thesis

This thesis is focused on studying interactional aerodynamics of a notional X2, specifically focusing on rotor-rotor and rotor-fuselage interactions across a broad range of forward flight speeds. The rest of the thesis is organized as follows:

- The second chapter describes the CFD-CSD framework used for this study as well as brief overviews of the codes used in this framework, namely PRASADUM and Helios. This chapter also details how the CFD codes solve the Reynolds Averaged Navier Stokes (RANS) equations as well as how the CSD code performs and calculates vehicle trim in forward flight.
- The third chapter highlights the building of the notional X2 vehicle configuration based on public domain information of the X2TD test program as well as validation of the CSD model using X2TD flight test data.
- The fourth chapter covers the isolated coaxial rotor system cases for 55, 100, and 150 knots. These cases highlight the key performance differences between a single and coaxial rotor system and quantify the interactional aerodynamic effects on blade airloads in the absence of a fuselage.



- The fifth chapter covers in detail a comparison study of rotor-fuselage interactional aerodynamic effects at two flight speeds, 55 and 150 knots, between 3 different fuselage models. These test cases illustrate the changes in flow field between the isolated rotor compared to the rotor and fuselage model together. The three fuselage models tested are a simple fuselage model, a complex fuselage model, and a complex fuselage model with the inclusion of the rotor mast. The complex fuselage model includes the empennage geometry as well as the lower hub fairing and the complex fuselage model with rotor mast simply adds the rotor mast to the complex fuselage model geometry.
- The sixth chapter summarizes all of the work conducted in this study and provides a roadmap and recommendations for future continuation of this analysis.

## Chapter 2: CFD-CSD Framework Theory and Methodology

### 2.1 Overview

This chapter covers the methodology of the CFD-CSD loose coupling framework. It presents brief explanations of the numerical methods of both the CFD and CSD solvers used in this work as well as a detailed explanation of the vehicle free flight trim process and loose coupling framework. As mentioned previously, the framework used for these simulations was the CREATE AV Helios framework which incorporated two near-body CFD solvers, OVERFLOW and NSU3D. The CSD solver was an in house code developed by Dr. Ananth Sridharan called PRASADUM and was integrated into the existing Helios Framework by I/O files.

### 2.2 CFD Methodology

The Helios framework consists of several separate modules that are wrapped with python bindings to create a seamless integrated toolset for solving various rotorcraft problems (Ref. [34]). The Helios framework uses SAMARC for off-body cartesian background grids which solve the Euler Equations (Ref. [34]). SAMARC is a combination of the SAMRAI code from Lawrence Livermore National Labs (Ref.

[13] [35]) and NASA’s ARC3D code (Ref. [24]). For near-body solvers, Helios has incorporated an unstructured RANS solver that is second-order accurate in space, NSU3D (Ref. [20]), as well as a higher order structured RANS solver, OVERFLOW (Ref. [6]). The unstructured near-body solver NSU3D was used for the fuselage grids for this work and OVERFLOW was used for the blade grids.

All notional X2 simulations were performed using similar runtime inputs. OVERFLOW meshes were run using second order (BDF2) time stepping with 20 sub iterations. OVERFLOW was run with fourth order central differencing for fluxes and used ARC3D diagonalized Beam-Warming scalar penta-diagonal scheme. OVERFLOW meshes used the SA turbulence model. Any simulations with a fuselage (where both NSU3D and OVERFLOW were used as near-body solvers) retained the same OVERFLOW inputs mentioned above for the OVERFLOW rotor blade grids; however, the NSU3D meshes were run using a CFL of 0.8 with a dissipation coefficient of 20 with 20 near-body sub-steps. The NSU3D solver also used the SA turbulence model and used central differencing for the fluxes. In all cases, the off-body grids were run in SAMARC and the off-body grids were the same grid size and grid type for all cases (including cases with fuselage meshes). SAMARC ran with fifth order accuracy and an off-body CFL of 1.0.

### 2.2.1 Off-Body Solver

SAMARC is used as the off-body CFD solver inside the Helios framework, which was used for all the computational CFD-CSD coupling cases of the notional

X2. SAMARC is a block-structured Euler equations solver that uses nested Cartesian background grids with increasing grid refinement (Ref. [34]). The Euler equations are solved using central differencing schemes that can maintain up to sixth order accuracy. Each refinement level of the nested Cartesian background grids maintains uniform spacing within each level with grid spacing on the order of two to four cells between levels (Ref. [34]). The off-body solver also has the ability to do adaptive mesh refinement (AMR) however that feature was not leveraged for this work.

### 2.2.2 Near-Body Solvers

Two near-body CFD solvers contained in the Helios framework were utilized for this work. Since the fuselage geometry is a complex non-uniform shape, it was easiest to build an unstructured grid around this topology for CFD to maximize conformance to underlying geometry without resorting to complex overset structured surface meshes. Therefore, the fuselage meshes were generated as unstructured meshes, solved by NSU3D, a second order unstructured finite volume RANS code (Ref. [34]). NSU3D is a vertex-based solver where the fluid and turbulence variables are stored at the vertices of the mesh and the fluxes are computed along the faces of the cell volumes (Ref. [34]). The unstructured fuselage meshes used by NSU3D contain prismatic cells in the boundary layer before transitioning to isotropic tetrahedra. The single equation Spalart-Allmaras turbulence model (SA model)(Ref. [29]) was used in NSU3D for these cases.

The second near-body CFD solver utilized for this work is the structured RANS code OVERFLOW (Ref. [6]). This solver uses a structured single block and/or Chimera overset grid system and solves RANS equations using various right hand side and left hand side schemes. There are many turbulence model options also available in the code however only the 1 equation SA model was used. OVERFLOW was chosen as the near-body solver for the blade meshes in the CFD simulation as the blades are highly structured geometry in nature and were generated with an O-O grid topology. Using higher order accuracy schemes with OVERFLOW, the blade grid solutions would yield the best possible results for blade aerodynamic load calculations to be sent back to CSD solver as well as ensure convection of higher order captured blade shed wake structures to the off-body CFD grids (solved by SAMARC).

### 2.2.3 Framework Integration

The three CFD solvers were tied into the Helios framework with python bindings and wrapper API scripts. Each CFD solver is an interface to the overall Helios framework. The other interfaces are the Domain Connectivity Function (DCF), which couples the near-body and off-body solvers using Chimera overset grid hole cutting approach at each time step, (Ref. [34]) and the Software Integration Framework (SIF) which is the main interface module for communication of the various other interfaces (ref. [34]).

The CSD code PRASADUM is run separate from the Helios framework and

the coupling between CFD and CSD occurs through I/O files. Helios will output aerodynamic blade loads to a file that PRASADUM will read and use for the next CSD iteration of the CFD-CSD coupling process and will write a blade deflection file that Helios will read for the next iteration of blade motions for CFD. These solvers are then run on modern high performance computing (HPC) platforms.

## 2.3 CFD Numerical Modeling and Theory

The CFD solvers numerically integrate the RANS equations, which is a system of nonlinear partial differential equations for unsteady, compressible flow. This is done in an Eulerian frame of reference. The governing equations are thus a system of hyperbolic conservation laws for a given fluid control volume where the conservation of mass, momentum, and energy laws of physics is met. The CFD solvers thus use the 3 dimensional Navier-Stokes equations (Ref. [12]) where the flow quantities are separated into their mean value and fluctuating part and solve only for the mean quantities of the flow. This simplified approximation of the direct Navier-Stokes equations introduces an additional tensor called the Reynolds stress tensor and closure is then achieved using a turbulence model.

### 2.3.1 Governing Equations

The general formulation of the governing Navier-Stokes equation in Cartesian coordinates is given below:

$$\frac{\partial Q}{\partial t} + \frac{\partial F_i}{\partial x} + \frac{\partial G_i}{\partial y} + \frac{\partial H_i}{\partial z} = \frac{\partial F_v}{\partial x} + \frac{\partial G_v}{\partial y} + \frac{\partial H_v}{\partial z} + S \quad (2.1)$$

$Q$  is a vector of the the conserved variables,  $F_i$ ,  $G_i$  and  $H_i$  are the inviscid flux vectors, and  $F_v$ ,  $G_v$  and  $H_v$  are the viscous flux vectors.  $S$  is the body forces source term. The various terms represented in the above equation are expressed in detail below.

The vector of conserved variables is

$$Q = \begin{bmatrix} \rho \\ \rho u \\ \rho v \\ \rho w \\ E \end{bmatrix} \quad (2.2)$$

The inviscid flux vectors are

$$F_i = \begin{bmatrix} \rho u \\ \rho u^2 + p \\ \rho uv \\ \rho uw \\ (E + p)u \end{bmatrix} \quad (2.3)$$

$$G_i = \begin{bmatrix} \rho v \\ \rho v u + p \\ \rho v u + p \\ \rho v w \\ (E + p)v \end{bmatrix} \quad (2.4)$$

$$H_i = \begin{bmatrix} \rho w \\ \rho w u + p \\ \rho w u + p \\ \rho w w \\ (E + p)w \end{bmatrix} \quad (2.5)$$

The viscous flux vectors are

$$F_v = \begin{bmatrix} 0 \\ \tau_{xx} \\ \tau_{yx} \\ \tau_{zx} \\ u\tau_{xx} + v\tau_{yx} + w\tau_{zx} - q_x \end{bmatrix} \quad (2.6)$$

$$G_v = \begin{bmatrix} 0 \\ \tau_{xy} \\ \tau_{yy} \\ \tau_{zy} \\ u\tau_{yx} + v\tau_{yy} + w\tau_{zy} - q_y \end{bmatrix} \quad (2.7)$$



$$H_v = \begin{bmatrix} 0 \\ \tau_{xz} \\ \tau_{yz} \\ \tau_{zz} \\ u\tau_{zx} + v\tau_{zy} + w\tau_{zz} - q_z \end{bmatrix} \quad (2.8)$$

Here, the density is  $\rho$ , the flow velocity components along each Cartesian direction are  $u, v, w$  and  $e$  is the internal energy per unit mass.

$q_x, q_y$  and  $q_z$  are heat conduction terms expressed as a function of temperature ( $T$ ) and coefficient of thermal conductivity ( $k$ ) given by Fouriers Law:

$$q_j = k \frac{\partial T}{\partial x_j} (j = x, y, z) \quad (2.9)$$

Pressure can be derived using the equation of state for a calorically perfect gas with  $\gamma$  (the ratio of specific heats) set to 1.4, as all the simulations are using air as the working fluid at standard pressure and temperature.

$$p = (\gamma - 1) \left[ e - \frac{1}{2} \rho (u^2 + v^2 + w^2) \right] \quad (2.10)$$

Temperature ( $T$ ) is obtained from the density and pressure where  $R$  is the gas constant:

$$T = \frac{p}{\rho R} \quad (2.11)$$

The viscous stress tensor for Newtonian fluids,  $\tau_{ij}$ , is given by Stokes' hypothesis:

$$\tau_{ij} = \mu \left[ \left( \frac{\partial u_i}{\partial x_j} \right) + \frac{\partial u_i}{\partial x_j} - \frac{2}{3} \frac{\partial u_i}{\partial x_j} \delta_{ij} \right] \quad (2.12)$$

where,  $\delta_{ij} = 1$  if  $i = j$   $\delta_{ij} = 0$  if  $i \neq j$  and  $\delta_{ij}$  is the Kronecker delta function.

The coefficient of molecular viscosity is given by Sutherland's law as follows:

$$\mu = \frac{C_1 T^{(3/2)}}{(T + C_2)} \quad (2.13)$$

where,  $C_1 = 1.4 \times 10^{-6} kg/(ms\sqrt{K})$  and  $C_2 = 110.4K$  for air at standard temperature and pressure.

### 2.3.2 Non-Dimensionalization

The Navier-Stokes equations are typically solved in a non-dimensional form so that all variables have similar scaling and thus avoid overflow and underflow truncation. The non-dimensionalization procedure is illustrated below where the non-dimensional parameters are identified with the superscript \*. Non-dimensionalization typically is done with respect to either free stream conditions (subscript  $\infty$ ) or a characteristic quantity such as speed of sound ( $a$ ) or length of the root chord of the blade ( $L$ ).

$$\begin{aligned} t^* &= \frac{ta_\infty}{L}, \quad (x^*, y^*, z^*) = \frac{(x, y, z)}{L}, \quad (u^*, v^*, w^*) = \frac{(u, v, w)}{a_\infty}, \\ \rho^* &= \frac{\rho}{\rho_\infty}, \quad T^* = \frac{T}{T_\infty}, \quad p^* = \frac{p}{\rho a_\infty^2}, \quad e^* = \frac{e}{\rho a_\infty^2}, \quad \mu^* = \frac{\mu}{\mu_\infty} \end{aligned} \quad (2.14)$$

The new non-dimensional parameters that are formed as a result of non-dimensionalization are given below:

$$\text{Reynolds number : } Re_\infty = \frac{\rho_\infty u_\infty L}{\mu_\infty} \quad (2.15)$$

$$\text{Mach number : } M_\infty = \frac{u_\infty}{a_\infty} \quad (2.16)$$

$$\text{Prandtl number : } Pr_\infty = \frac{\mu C_p}{k} \quad (2.17)$$

For air at standard temperature and pressure, the Prandtl number is set to  $Pr = 0.72$  and  $V_\infty$  is the free-stream velocity magnitude which is given by  $\sqrt{u_\infty^2 + v_\infty^2 + w_\infty^2}$ . Lastly, upon non-dimensionalization the mean stresses and thermal conduction terms are re expressed as the following where the superscript \* is now removed for clarity:

$$\tau_{ij} = \frac{\mu M_\infty}{Re_\infty} \left[ \left( \frac{\partial u_i}{\partial x_j} + \frac{\partial u_j}{\partial x_i} \right) - \frac{2}{3} \frac{\partial u_k}{\partial x_k} \delta_{ij} \right] \quad (2.18)$$

$$q_j = - \frac{\mu M_\infty}{Re_\infty Pr (\gamma - 1)} \frac{\partial T}{\partial x_j} \quad (2.19)$$

### 2.3.3 RANS Model

Solving the Navier-Stokes equations directly is computationally infeasible due to the fine cell resolution and rather large number of grid points required to accurately resolve all scales of turbulence. One approach to simplify the problem is the use of Large Eddy Simulation (LES), where only the large scales of turbulence are captured and the small scales are statistically modelled. This method however is still rather costly and not feasible for rotorcraft simulations. The only practical

method at this time is RANS. The RANS equations, as mentioned previously, split the flow quantities into mean  $\bar{\phi}$  and fluctuating parts  $\phi'$ , i.e.,

$$\phi = \bar{\phi} + \phi' \quad (2.20)$$

When applying this method to the Navier-Stokes equations (Eq. 2.1) and performing time-averaging, an additional tensor called the Reynolds Stress Tensor is introduced:

$$(\overline{\tau_{ij}})_{turb} = -\rho \overline{u_i u_j} = \frac{\mu M_\infty}{Re_\infty} \left[ \left( \frac{\partial u_i}{\partial x_j} \right) + \frac{\partial u_i}{\partial x_j} - \frac{2}{3} \frac{\partial u_i}{\partial x_j} \delta_{ij} \right] \quad (2.21)$$

This Reynolds Stress Tensor is a function of turbulent fluctuating quantities. To achieve model closure, an additional set of equations is required, referred to as turbulence models. The 1 equation SA turbulence model is used for this work.

## 2.4 CSD Methodology and Theory

The CSD solver used for this work is a comprehensive analysis code that was developed in house at the University of Maryland. This code is based on finite element methodology (Ref. [30]) and the rotor blades are modelled as flexible rotating Euler-Bernoulli beams with flap, lag and torsion. Rotor blades are modeled using quasi-steady aerodynamics and table look up for angle of attack and Mach number. The CSD solver incorporates two rotor inflow models:

1. Dynamic Inflow
2. Maryland Free Wake

Given input blade geometry, structural properties, and aerodynamic look up tables for lift, drag, and pitching moment, the CSD solver can run using either a dynamic inflow model or a free wake model (Ref. [11]) to get a converged propulsive trim solution for a given flight condition. This can be done either with Finite Element in Time (FET) or Harmonic Balance method for azimuthal resolution of the rotating beam modes. For this work, the CSD code was run using a free wake and the Harmonic Balance method. The CSD code outputs blade loads, blade motions (as deflection files that can be read by CFD), rotor controls, and fuselage attitude. The CSD solver for all cases was run with 96 azimuthal sampling points for rotor loads, using the first 6 modes with 8 azimuthal harmonics.

### 2.4.1 CSD Aerodynamic Models

A Free Vortex Wake analysis allows for numerical calculation of the radial variations in inflow distribution including the distributions caused by inviscid blade-vortex interactions. Since this work focuses on a notional X2 coaxial configuration, the free wake model was used in the CSD solver due to the expected aerodynamic interaction between both rotor blades on each other as well as interactions between each rotors trailed wake with the other rotor. Details of the in house free vortex wake methodology implemented in the CSD solver can be found in (Refs. [19], [2]).

## 2.4.2 CSD Trim Analysis

This section briefly explains the trim procedure used in the CSD solver. In rotorcraft, rotor trim is achieved by ensuring that given constant controls, the rotor blade response is periodic and the hub forces and moments, when averaged over one revolution, do not change over successive cycles. This criterion is then coupled with the zero acceleration condition for the vehicle in the vehicle body axes frame from classical fixed wing vehicle trim to get the definition for rotorcraft trim. For steady level forward flight, the vehicle acceleration components along the body axes must be zero and the rotor response must be periodic for a rotorcraft solution to be in trim. The global flow chart of the CSD solver is presented in Fig. 2.1.

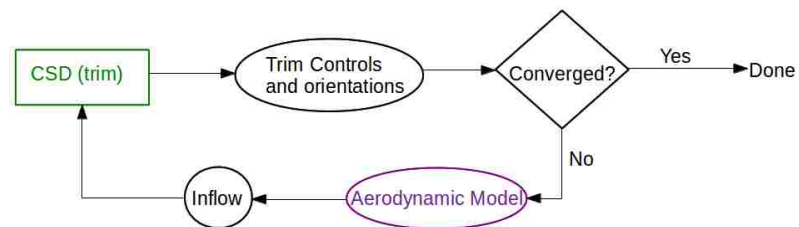


Figure 2.1: CSD solver global flow chart

Trim is achieved by finding the pilot controls and fuselage pitch and roll attitudes that yield steady level flight with zero body axes acceleration while maintaining a periodic rotor response. This trim process is detailed in (Ref. [30]). A flow chart of this trim process inside the CSD solver is shown in Fig. 2.2.

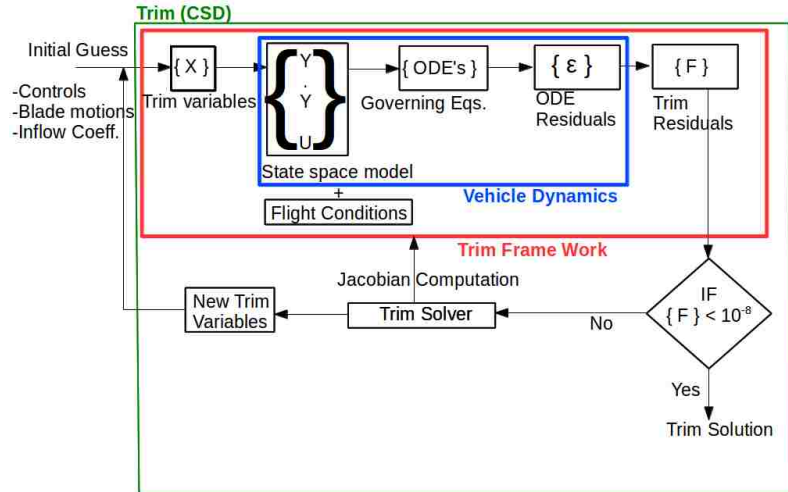


Figure 2.2: CSD solver rotorcraft trim flow chart

When using the free wake model, the structural dynamics and aerodynamic look up tables are loosely coupled to the free wake code. A flow chart of this coupling process is shown in Fig. 2.3. After satisfying the trim conditions with dynamic inflow, the main rotor inflow equations are removed from the trim conditions and the loose coupling information transfer between the free wake model and the flight dynamics begins and will run to iterative convergence. This process is further detailed in (Ref. [14]).

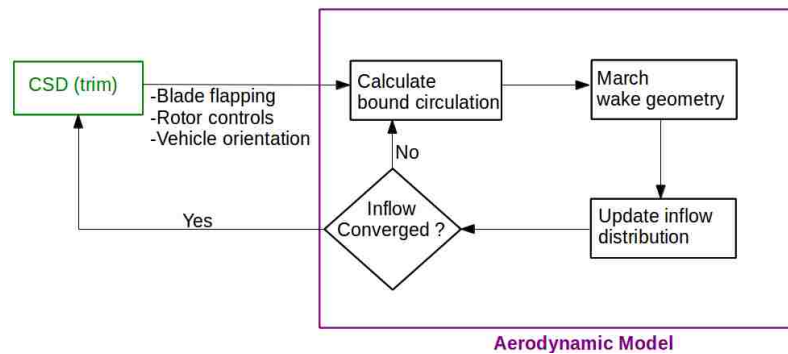


Figure 2.3: CSD solver rotorcraft aero-trim coupling flow chart

## 2.5 CFD-CSD Coupling

The work presented in this thesis uses CFD-CSD coupling to obtain high fidelity solutions of the notional X2 vehicle configuration at various forward flight speeds. CFD-CSD coupling can be done via two different approaches, loose coupling or tight coupling. The loose coupling methodology involves coupling CFD with the CSD solver that includes a lower order aerodynamic model based on look up tables. This decouples the CFD from the trim process that occurs in the CSD solver. CSD will perform rotor trim and then prescribed blade motions from the CSD solver will be fed to the CFD solver. The CFD solver will then feed airloads as delta corrections back to the CSD solver's aerodynamic look up tables. This process is usually done every rotor revolution. This means that, in theory, the lower order aerodynamics with corrections from CFD will move the trim solution to be in line with the CFD predictions and convergence can be achieved in typically 6-10 coupling iterations.

In contrast to loose coupling, tight coupling is done every time step and not every rotor revolution. This means that tight coupling the CFD and CSD solvers will introduce more complexity in assuring time accuracy of the solutions and typically results in the need for costly sub iterations between time steps. This process is also not necessarily straightforward unless the trim controls are known ahead of time.

While there have been many validations of the loose coupling CFD-CSD approach on other aircraft configurations, notably the UH-60 (Refs. [23], [10]) and HART II (Ref. [1]), there is limited work in the public domain literature of this process being used to evaluate compound coaxial vehicles like the notional X2. The



loose coupling approaches from Ref. [23] for the UH-60, coupled the CFD and CSD solvers every rotor revolution and used a simple uniform inflow model in the CSD solver for trim.

For this work, the loose coupling CFD-CSD approach is used and the CFD and CSD solvers exchange information every 2 rotor revolutions instead of 1 rotor revolution. It was found that coupling back every single rotor revolution with a coaxial rotor system, in some cases, was not sufficient to dampen out the transient responses from the new blade motions from the CSD solver. Therefore, to ensure robustness and further encourage a steady state periodic CFD solution is sent to the CSD solver, 2 rotor revolutions were run with CFD before coupling back to CSD.

Further, the CSD solver is using the free wake model instead of the simpler dynamic or uniform inflow models during trim. The lower order inflow models had trouble converging to a trimmed solution. This issue is hypothesized to stem from the unique differences between the notional X2 vehicle design compared to conventional helicopters that have been analysed using the CFD-CSD loose coupling process. Namely, unlike the UH-60 or other conventional helicopters, the notional X2 tends to have an aft tilt of the rotor disk at forward speeds. The added auxiliary propeller also causes the 2 main rotors to be in a unpowered auto-rotative state at very high speeds.

This combination of induced rotor downwash and a descent like state of the main rotors is believed to be why the simpler dynamic inflow models failed to reach coupled trim convergence easily without the free wake method. These issues, along with the complex interacting wake structure and interference of two closely spaced

main rotors invalidates some of the assumptions that are made in these reduced order models that the free wake method is able to capture more accurately.

A flow chart of the CFD-CSD loose coupling framework used for the forward flight cases in this work is illustrated in Fig. 2.4.

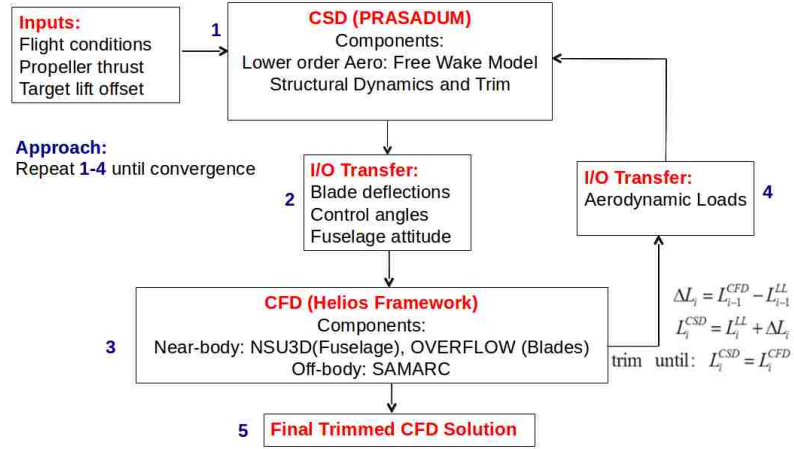


Figure 2.4: CFD-CSD loose coupling flow chart

Step (1) is to input the given flight condition and relevant parameters to the CSD solver; which already contains structural dynamic properties, vehicle configuration properties and geometry, and 2D aerodynamic look up tables containing sectional lift, drag, and pitching moment for the various airfoil sections along the rotor blades. Then, the CSD solver will use the existing look up tables and a built in lower order aerodynamic model, in this case free wake, to obtain an initial trimmed solution. Step (2) transfers blade deflections, control angles, and fuselage attitude to the CFD solver. The CFD solver will then run with the given vehicle flight attitude at the same flight conditions and run for 2 revolutions with the prescribed blade motions sent from the CSD solver. Step (4) transfers blade aerodynamic loads

and send them back to the CSD solver for a new trimmed solution. Steps 1-4 will run until convergence is achieved. For convergence criteria there are many quantities to look at; namely, the rotor controls should have steadied over the coupling process; the integrated quantities of rotor thrust, rotor thrust fraction, and total vehicle thrust and power should match closely between CFD and CSD; and lastly, the airloads predicted by CFD and by the CSD code should match satisfactorily for both rotor systems across all radial stations.

The convergence process (Steps 1-4) is carried out via information transfer between the two codes using I/O files. The aerodynamic loads that CFD outputs after each 2 rotor revolutions are completed is used by the CSD code to generate a delta airloads file. This means that the 2D aerodynamic properties the CSD code uses for the next trim cycle will contain the original 2D aerodynamic values from the tables with corrections from the previous CFD run. The delta airloads file is generated by subtracting the CSD airloads from the CFD airloads.

To generate the delta airloads file, the CSD code will first trim to a given flight condition and send the blade motions and vehicle attitude to CFD for a prescribed CFD run of 2 revolutions. While this is occurring, the CSD code will be run again with the exact same fixed controls and blade motions it had sent to CFD. Then, when the CFD has finished running, the delta airloads file will be generated by subtracting the CSD runs fixed controls and blade motions aerodynamic loads from the CFD's aerodynamic loads. Therefore, each CFD-CSD coupling cycle consists of 2 runs of the CSD solver:

1. To get the newest trimmed solution conditions based on the previous iterations delta airloads file.
2. To get the new baseline CSD uncorrected aerodynamic loads given this new trim states fixed controls and blade motions.

The CFD is run for 2 rotor revolutions to get new updated CFD airloads that will then, combined with the airloads from the 2nd run of the CSD solver, generate a delta airloads file that will be used to update to the next CFD-CSD iterations trimmed state. This process is repeated until a satisfactory final converged solution is obtained, which typically occurs in around 4-6 coupling iterations.

## Chapter 3: Notional X2 Model Validation

### 3.1 Overview

This chapter covers in detail the physical configuration, geometry, and dynamic characteristics of the notional X2 model used in this study. The notional X2 model was built from existing public-domain knowledge of the X2TD flight test program supplemented by engineering assumptions. The first section will detail the notional X2 main rotor geometry, vehicle layout, fuselage geometry, and estimation of the structural properties. This section also presents the 2D aerodynamic look up tables generated from 2D CFD, and how the structural solver and trim process were modified to include the pusher propeller for this work.

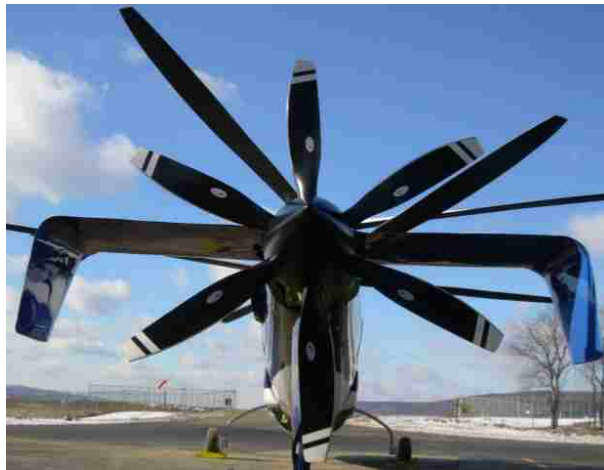
The second piece of this chapter will cover how the notional X2 model implemented into the CSD code, PRASADUM, was validated against both available X2TD data and a CAMRAD II model that was built by Dr. Wayne Johnson at NASA Ames (Ref. [16]). The final section covers the implementation of the notional X2 model into CFD solvers, namely, the mesh generation process of the blade and fuselage grids, the overall mesh system and co-ordinate reference system, and the sign conventions for the deformed frame airloads and deflections that are exchanged between both the CFD solver and the CSD solver.

## 3.2 Notional X2 Vehicle Configuration

There are several papers that have been published concerning the Sikorsky X2TD flight test program (Refs. [4], [32], [33], [5]). As mentioned earlier, the X2TD was a demonstrator aircraft and Sikorsky's latest ABC methodology helicopter design successor to the XH-59A. The X2TD is a 5,000 lb class vehicle that has a 8 bladed coaxial main rotor (4 blades per rotor) as well as a 6 bladed auxiliary propeller mounted at the rear (Ref. [5]) and is shown in Fig. 3.1.



(a) X2TD vehicle configuration



(b) X2TD auxiliary propeller

Figure 3.1: Sikorsky X2TD vehicle configuration and auxiliary propeller (Ref. [5])

Test data for integrated performance, tip clearance, and rotor lift offset ob-

tained from flight tests were used to guide model creation and determine trim targets. Sikorsky provided in Ref. [5], flight test data of integrated total rotor power, propeller power, and on board power available over all the flight test forward speed conditions. This data is normalized to a density altitude of 4,000 ft even though the raw data points (not provided in literature) were done at varying density altitude conditions and is shown in Fig. 3.2 (Ref. [5]). In order to benchmark the notional X2 model, it was chosen to run simulations at a density altitude that matched the integrated power data; therefore, both the CSD and CFD solvers were run at various forward flight speeds at a 4,000 ft density altitude.

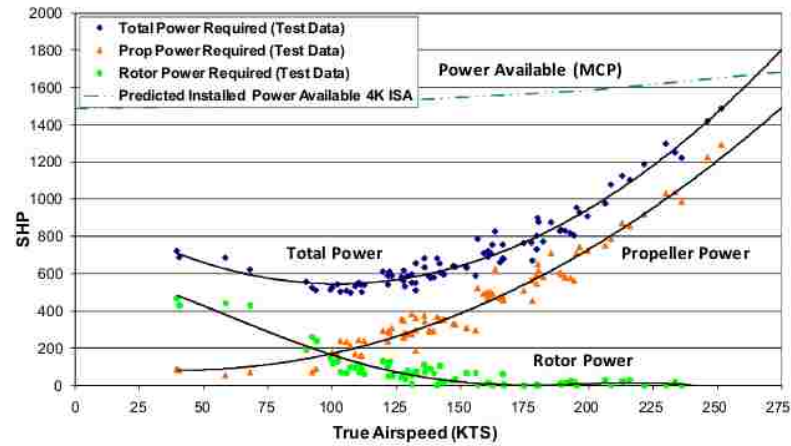
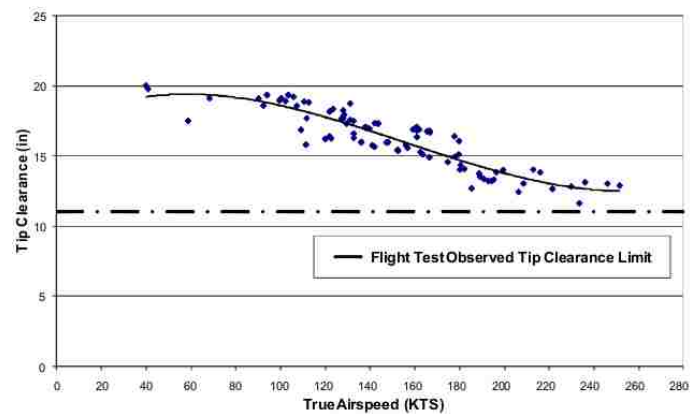


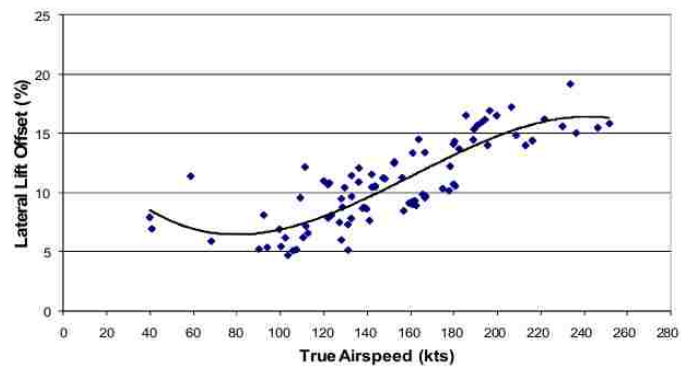
Figure 3.2: Sikorsky X2TD power curves for flight tests normalized to 4,000 ft density altitude (Ref. [5])

Data was also available regarding observed tip clearance between the upper and lower main rotor blades and was used as a guide in ensuring that the structural dynamics model of the notional X2 design would conform to the same tip clearance limit. Therefore, both the notional X2 model and the actual X2 have an observed

tip clearance limit of 11 inches and the notional X2 model was able to adhere to that minimum clearance requirement across the entire flight envelope from 0-250 knots. Data regarding the selected LOS for each flight test point was also provided in Ref. [5], and it was chosen that the notional X2 model would have a prescribed linear fit through this data. These quantities are detailed in Fig. 3.3



(a) X2TD tip clearance



(b) X2TD lift offset

Figure 3.3: X2TD variation of rotor-rotor tip clearance and LOS with airspeed (Ref. [5])



### 3.2.1 Vehicle Layout

As previously mentioned, the X2TD is a 5,000 lb aircraft and the design limit load according to Ref. [4] was 6,000 lbs. Therefore, the Notional X2 model was given a gross weight of 5,955 lbs. The main rotor radius remains the same as the X2TD at 13.2 ft and retains the 8 bladed coaxial main rotor. The notional model also has the lower rotor rotating CW and the upper rotor rotating CCW just like the X2TD. The notional X2 vehicle configuration details are noted in Table 3.1.

<b>Parameter</b>	<b>Value</b>
GW (lb)	5955
R (ft)	13.2
Hub Type	Hingeless Coaxial (upper CCW)
Vtip (ft/s)	620
Rotor Spacing (in)	18
Flight Altitude (ft)	4000

Table 3.1: Notional X2 Vehicle Configuration

The main rotor rpm for the X2TD is constant from hover to 200 knots forward speed before being reduced to hold the effective Mach number at the tip on the advancing sides to 0.9 M. The notional X2 model retains the hover rpm (446 rpm) from hover to 200 knots. Then, the rpm is linearly reduced from 446 rpm to a final slowed speed of 360 rpm at 250 knots. This main rotor rpm schedule for the notional X2 closely mimics the X2TD by ensuring the effective Mach number at

the tip on the advancing sides remains below 0.9 M. The shaft tilt of the X2TD is never mentioned in literature, however in Ref. [4] it is stated that the XH-59A had a shaft tilt between -4 and +2 degrees and that the X2TD would have a similar range. The shaft tilt for the main rotor on the notional X2 model is therefore set to be 0 degrees. The rotor spacing between the two coaxial main rotors was fixed at 1.5 ft.

## Empennage

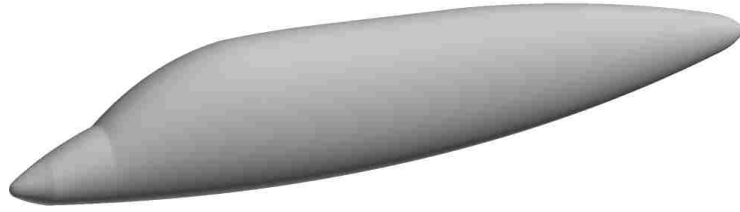
The notional X2 model also follows the empennage design of the X2TD. It contains both a horizontal and a vertical tail. It was noted that during flight test at high speeds, the X2TD had some instabilities in static vehicle pitch and a secondary horizontal tail was designed and implemented on the vertical tail (Ref. [5]). This is not implemented on the notional X2 model. The notional X2 model has a single horizontal tail with an equivalent flat plate surface area of  $34 \text{ ft}^2$  and a single vertical tail with an equivalent flat plate surface area of  $15.4 \text{ ft}^2$ . Further, the horizontal tail was given an initial incidence angle of positive 5 degrees relative to the fuselage in the notional X2 model.

## Fuselage Geometry

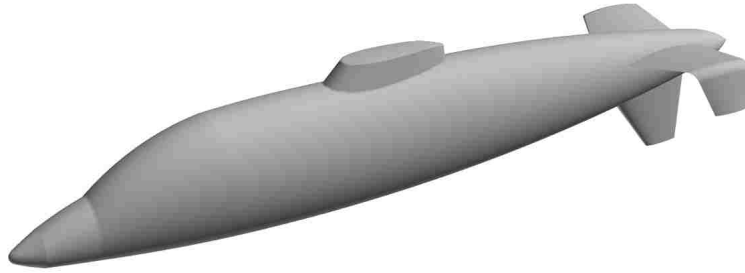
Three fuselage designs were generated in CAD to approximate the X2TD fuselages generic shape, and these CAD geometries were used to generate three fuselage meshes:

1. Simple Fuselage
2. Complex Fuselage
3. Complex with Mast Fuselage

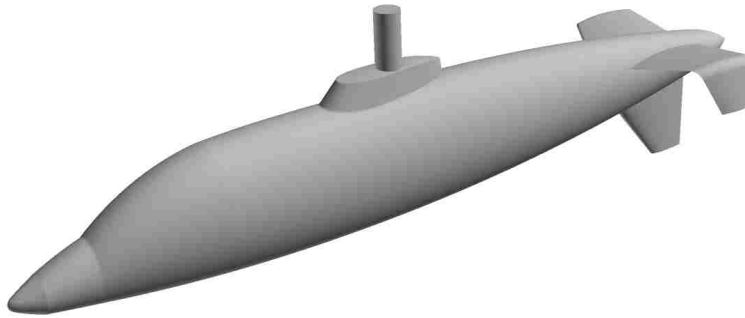
All three fuselage designs have the same overall dimensions (44.58 root chord lengths long and a diameter of 7.1 chord lengths at its thickest point). The simple fuselage geometry only retained the X2TD main fuselage body (cigar-like) shape and does not include the tail geometry, rotor mast, or hub fairing. The complex fuselage retains the same generic shape as the simple fuselage and also includes the horizontal and vertical tail surfaces as well as the hub fairing between the fuselage and the lower rotor. Finally, the third fuselage model includes a representative cylindrical rotor shaft that runs from the fuselage to the upper rotor hub. The root cut out region and complex swash plate and hub geometry are not modeled or represented. The CAD surfaces of these fuselage models are illustrated in Fig. 3.4.



(a) Simple Fuselage



(b) Complex Fuselage



(c) Complex with Mast Fuselage

Figure 3.4: Three notional X2 fuselage CAD models

The X2TD features a 6 bladed auxiliary propeller mounted at the tail. For this work, the propeller is not modeled in the CFD flow field and is only represented as a prescribed thrust in the CSD code. It is possible, in future work, to generate a notional propeller model in CAD and implement it into the CFD solver as well as potentially generate structural properties and model the propeller as more than a simple prescribed thrust in the CSD code.

### 3.2.2 Main Rotor Blade Structural Properties

The X2TD structural main rotor blade properties are not publicly available; however, in Ref. [4] Bagai asserts that in designing the X2TD main rotor blades, it was a scaled and evolutionary derivative of the XH-59A. The only information provided was a fan plot of the X2TD main rotor blade frequencies (Ref. [5]). The blade structural properties (flap bending, lag bending and torsion stiffness) distributions along the span were tuned to match the X2TD fan plots as closely as possible.

An assumption was made that the CG-EA offset was set to zero for the notional X2 model in the absence of any other info. This assumption effectively uncouples flap and lag bending from torsion for an elastic axis passing through the quarter chord. A parametric sweep was conducted by varying the flap, lag, and torsional stiffness distributions of a baseline XH-59A main rotor blade. Stiffness distributions that were obtained matched reasonably well with X2TD blade frequencies from Ref. [5]. Dr. Wayne Johnson at NASA Ames had used a similar approach for his study of the X2TD in CAMRAD II (Ref. [16]) and our notional X2 structural model was compared to the actual X2TD and his CAMRAD II model for blade frequencies.

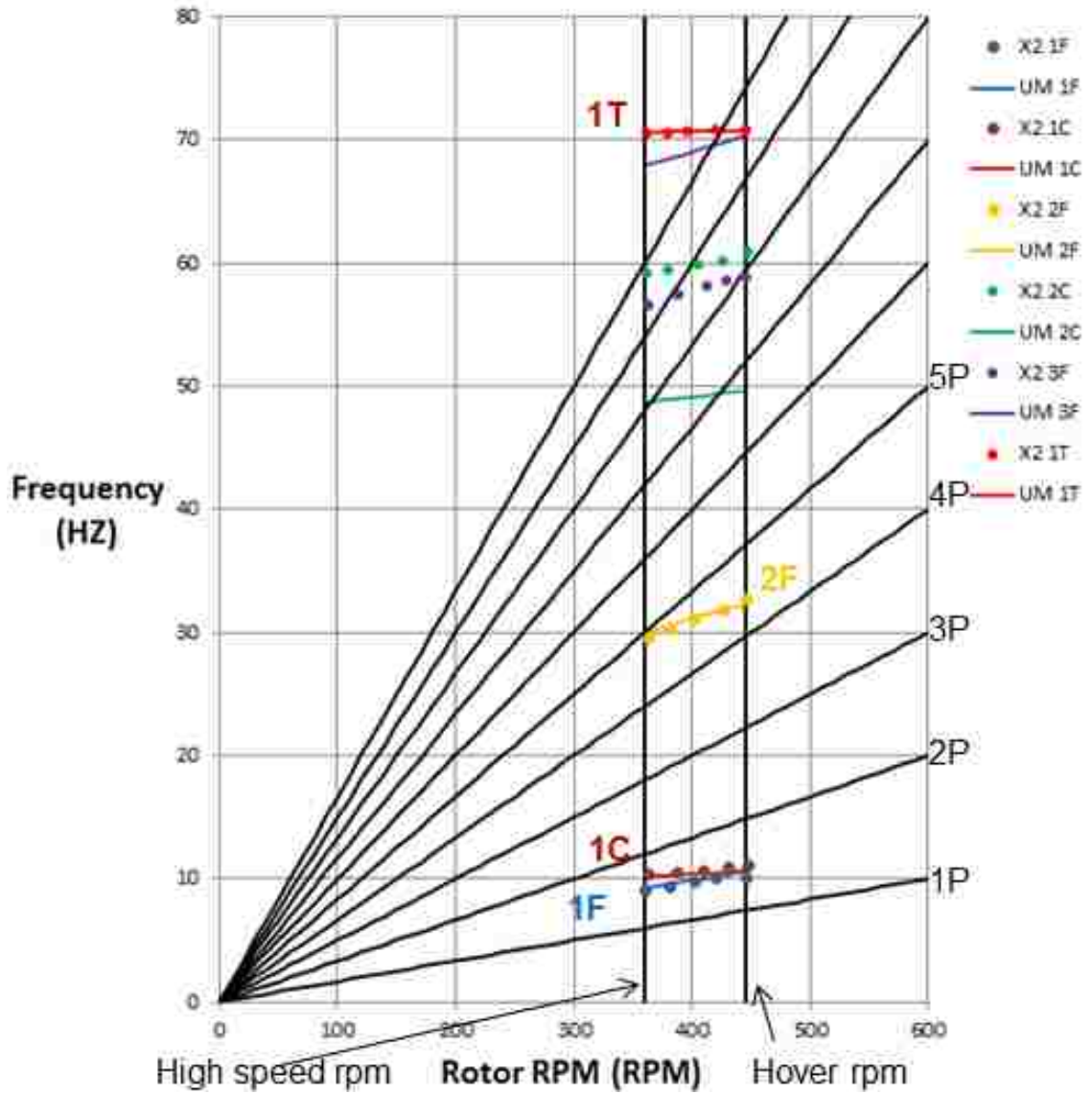


Figure 3.5: Notional X2 main rotor fan plot

As can be seen from the notional X2 fan plot in Fig. 3.5, the notional X2 rotating natural frequencies for the main rotor blades derived off of the XH-59A have very good agreement with the X2TD data for the first flap, first chord, second flap, and first torsion frequencies. The second chord and third flap exhibit noticeable

error with respect to the X2TD data from Ref. [5]. However, these higher flap and chord frequencies match well with Ref. [16], and these estimates should be adequate for this study. Since the X2TD uses a rigid coaxial hub, the CSD solver models it as a hingeless rotor. It should be noted that the CAMRAD II data was digitized and replotted and due to that process there may be "spurious" wiggles that appear in the data on some of the plots in Fig. 3.6.

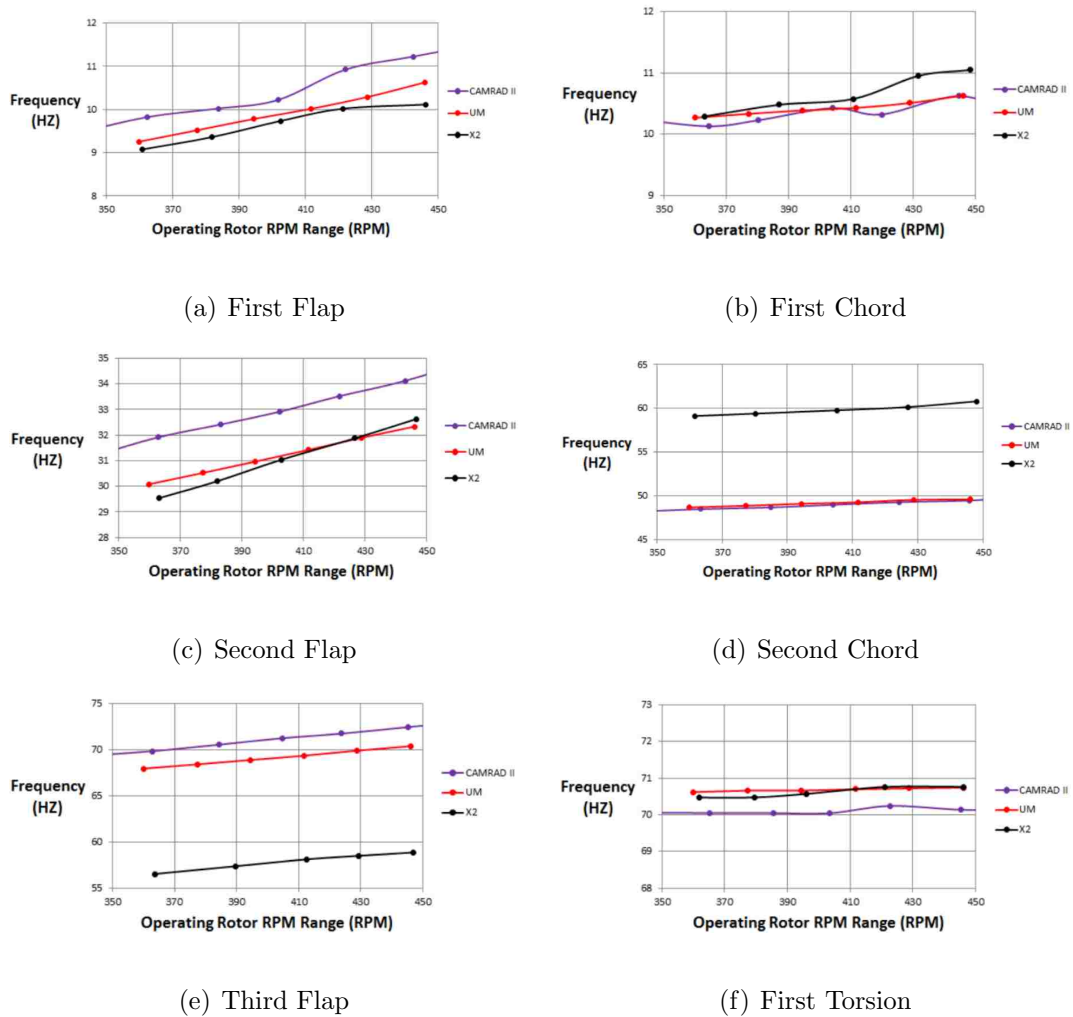


Figure 3.6: Notional X2 main rotor blade structural frequencies

### 3.2.3 Main Rotor Design

The X2TD main rotor design was detailed by Bagai in Ref. [4] and the notional X2 model attempted to match this as closely as possible. The notional X2 configuration maintains the same number of blades (4 per rotor) and the blade radius at 13.2 ft. The root chord of the blade was 0.687 ft, giving the blade an aspect ratio of 19.193857. The twist distribution,  $c/R$ , and  $t/c$  distributions provided in Ref. [4] are also incorporated into the main rotor design of the notional X2 model and shown in Fig. 3.7.

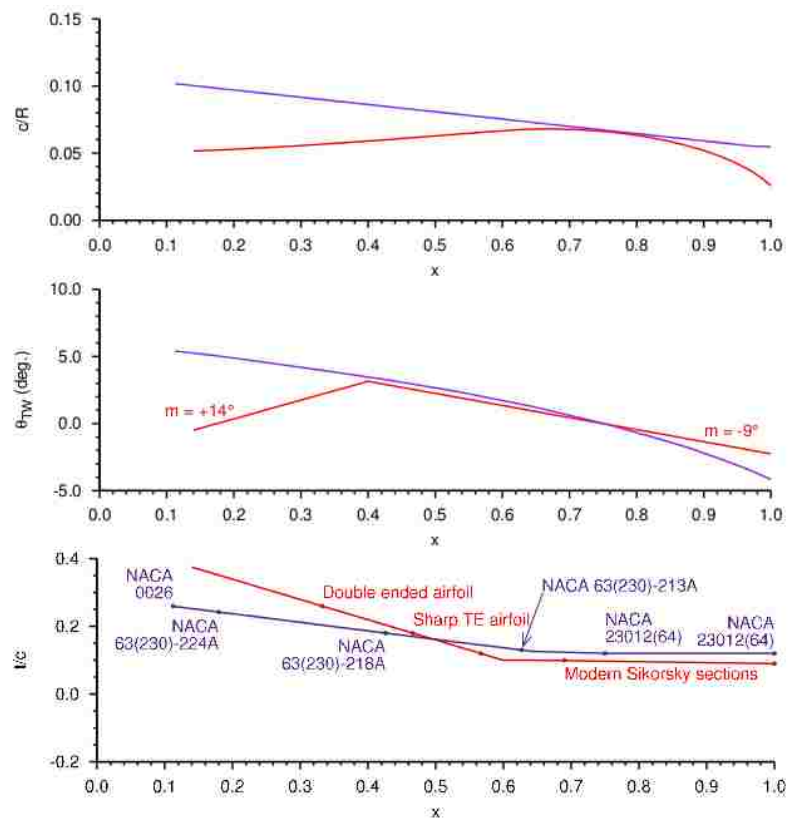


Figure 3.7: X2TD main rotor blade geometry implemented into notional X2 model (Ref. [4])



Unfortunately, there was no published information regarding the specific airfoil shapes used on the actual X2TD; however, generic airfoil profile shapes along the span were obtained from both the published literature and inferred from engineering estimates given its design goal. The X2TD main rotor blade was designed to mitigate drag in the reverse flow region of the inboard sections of the blade, therefore it is well known that double ended airfoils were used on the inner parts of the blades (Ref. [4]). The airfoil cross section would then vary from the double ended elliptic sections to a sharp TE high lift airfoil section in the midspan regions before transitioning again to a transonic airfoil cross section at the tip (Ref. [4]).

Given the information above, the cross sectional airfoil profiles chosen for the notional X2 main rotor blade along the span are illustrated below in Table 3.2.



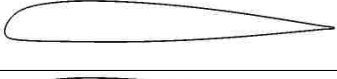



<b>Radial Location (r/R)</b>	<b>Airfoil Section Type</b>	<b>Airfoil Shape</b>
0.142	modified DBLN-526	
0.331	modified DBLN-526	
0.468	modified SC1012-R8	
0.568	modified SC1012-R8	
0.6	modified SSCA-09	
1.0	modified SSCA-09	

Table 3.2: Notional X2 model airfoil cross sections

The main rotor blades retain the same root cut out region of 14.2 % of blade radius as the X2TD. For the first inner third of the main rotor blade, the notional X2

model uses a slightly modified DBLN-526 airfoil cross section and then transitions to the SC1012-R8 over the midspan before transitioning again in the outer third of the blade to the transonic SSCA-09 airfoil shape. These airfoil shapes were chosen due to the similar design characteristics that the expected airfoils would most likely exhibit on the real X2TD configuration. To ensure the blade planform,  $c/R$ , and  $t/c$  matched as closely as possible to Ref. [4], these airfoil shapes had to be slightly modified to ensure smoothness in the blade surface. Therefore, the notional X2 models main rotor blades appear almost exactly the same as the X2TD main rotor blades, sharing the same characteristic features and distributions; however, some engineering inference was done in selecting the detailed profiles.

### 3.2.4 2D Aerodynamic Look up Tables

Comprehensive Analysis codes rely on lower order aerodynamic models and look up tables to obtain time efficient trimmed solutions. No 2D aerodynamic look up tables for the X2TD exist in the public domain and so these tables for the notional X2 had to be generated for the CSD solver. To generate these tables, 2D RANS CFD calculations were performed for various angle of attacks and Mach numbers for each of the airfoil sections in the main rotor blade. The in house code, TURNS (Ref. [28]), was used to perform these 2D CFD calculations to get  $c_l$ ,  $c_d$ , and  $c_m$  for each airfoil cross section along the blade.

These 2D CFD calculations were performed using RANS with the SA turbulence model in time accurate mode with dual time stepping and Newton sub-

iterations to obtain converged solutions. Each of the 6 airfoils along the span of the notional X2 main rotor blade was run with angle of attacks from -15 to + 15 degrees for Mach numbers from 0.3 to 0.9. A list of high angle tables (-180 to +180) was already implemented into the CSD code and was borrowed for the notional X2 model to provide representative data for the inboard sections.

For the horizontal and vertical tails of the notional X2 model,  $c_l$  and  $c_d$  look up values were calculated using finite-wing theory (Ref [3]). Lastly, the fuselage body drag coefficient was calculated from an equivalent flat plate area which was  $4.6 \text{ ft}^2$  based on Ref. [16]. As previously mentioned, the auxiliary propeller on the X2TD is not modeled in the CFD and for the CSD solver it is also not modeled. Instead, a propeller efficiency of 0.85 was assumed similar to Ref. [16]. A prescribed propeller thrust value was calculated from measured propeller power. This calculated thrust varies with airspeed and is provided as a prescribed input for the CSD solver. The auxiliary propeller remains ineffective until a forward speed of 50 knots is reached.

### 3.3 CSD Code Notional X2 Model Validation

The CSD solver used in this study, PRASADUM, has already been extensively used and validated for conventional single rotor configurations such as the HART II and the UH-60. Generally, the CSD code can predict integrated loads with high accuracy in forward flight. A sample correlation between predicted power against test data is shown in Fig. 3.8 for an altitude of 3,670 ft. Excellent agreement is obtained at all airspeeds.

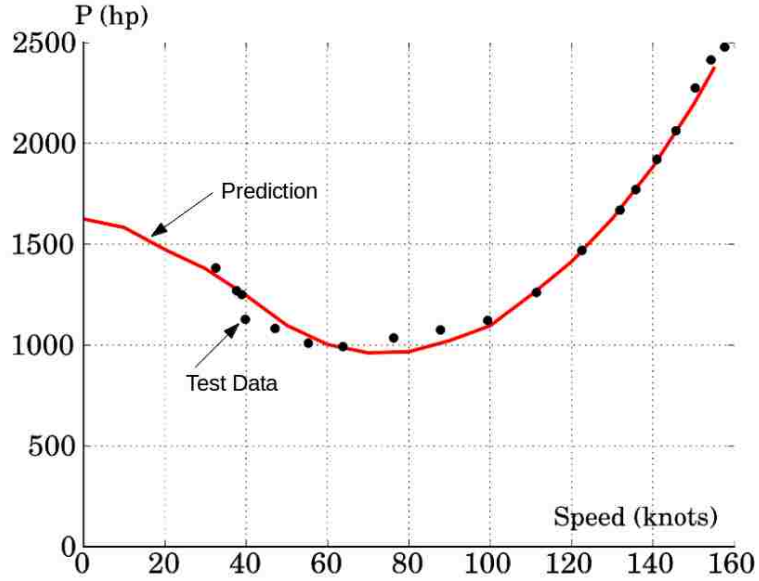
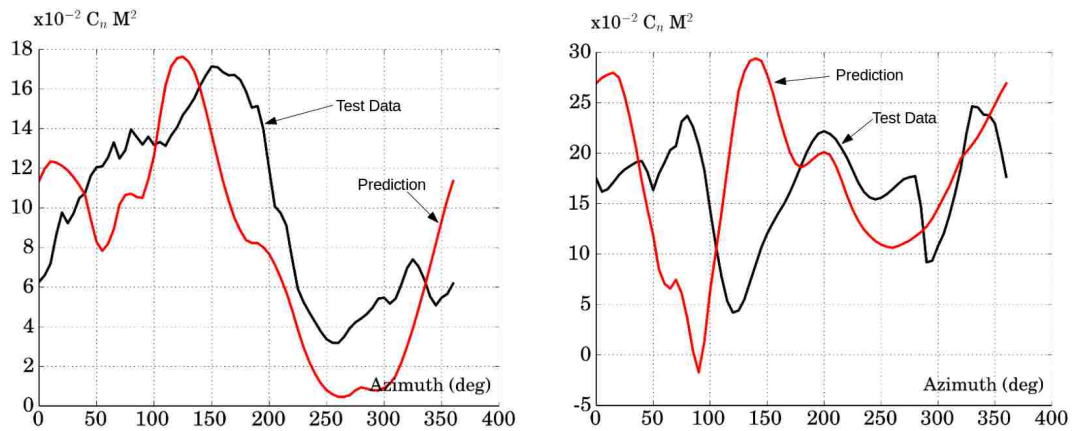


Figure 3.8: UH-60 main rotor power required at 3,670 ft density altitude

Further, this CSD solver also provides good estimates of aerodynamic loads. A sample comparison for the UH-60 comparing predicted with test data for Run 45, Point 37 from the UH-60 NASA Ames wind tunnel test (Ref. [21]) is shown in Fig. 3.9.



(a) 40% Span Normal Force

(b) 77.5% Span Normal Force

Figure 3.9: UH-60 predicted  $C_n M^2$  from Run 45, Point 37

The notional X2 model was implemented into the CSD solver and rotor performance was compared to measured data from flight tests. The methodology for getting trimmed flight condition for this model was to first prescribe the LOS for each flight condition as shown in Fig. 3.10. Then, a propeller power would be chosen that would yield a predicted rotor power from the trimmed solution that would correlate to the rotor power from the flight test at the given flight condition similar to Ref. [16]. For the LOS control, both PRASADUM and CAMRAD II models chose to have a linear prescribed LOS vs forward speed through the test data.

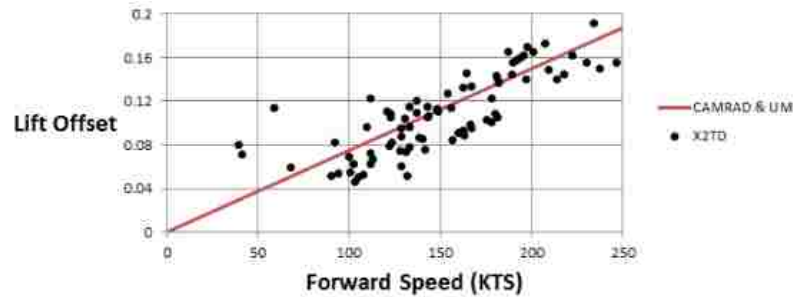


Figure 3.10: Prescribed LOS control vs. X2TD flight test

A speed sweep was performed with the CSD solver from hover to 250 knots and the total main rotor shaft power and propeller power were compared both to predictions from CAMRAD II and X2TD flight test data. For the propeller power, CAMRAD II predictions lie on the upper bound of test data scatter. PRASADUM was able to predict total rotor power with as much fidelity to test data as CAMRAD II but the associated propeller power fit better to the propeller power flight test data. The predicted propeller power vs. forward speed is shown in Fig. 3.11 and the predicted total rotor power vs. forward speed is shown in Fig. 3.12.

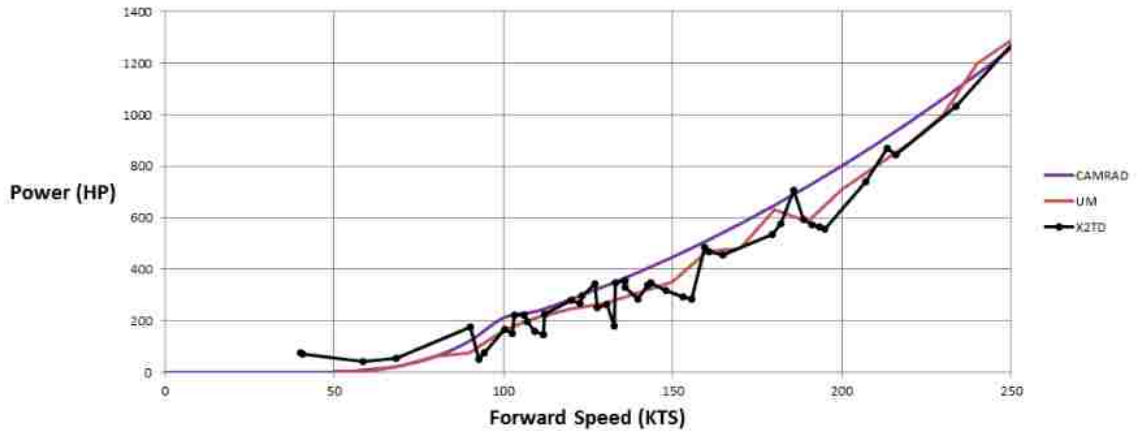


Figure 3.11: Predicted Propeller Power vs. Forward Speed

Both CAMRAD II and PRASADUM satisfactorily predict total rotor power for all flight conditions. The CSD solver was run using the free wake model. The code was run with 96 azimuthal sampling points for rotor loads, using first 6 modes with 8 azimuthal harmonics. The hover condition requires maximum rotor power. As forward speed is increased, the total rotor power decreases. Unlike conventional single main rotor helicopters, the compound coaxial has an auxiliary propeller to provide thrust. Thus, by 150 knots, the coaxial main rotors are in a near autorotative state. The notional X2 model closely follows this trend.

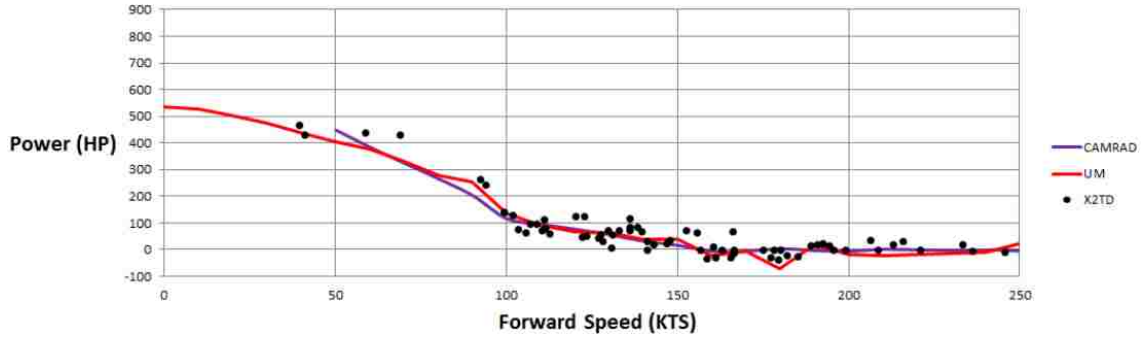


Figure 3.12: Predicted Total Rotor Power vs. Forward Speed

### 3.4 Notional X2 Model CFD Implementation

The notional X2 model was also incorporated into the CFD solvers. As previously mentioned, the notional X2 main rotor blades were modeled as structured CFD grids and flow simulations were performed using the OVERFLOW near-body solver in the Helios framework. The CAD geometry of the fuselage formed the basis for generating unstructured fuselage grids, and were run using NSU3D near-body solver. For all cases, SAMARC was used to generate both the off-body grid and acted as the off-body flow solver in the Helios Framework. For all forward flight cases, the off-body Cartesian background grids remained the same. The blade grids also remained the same for all forward flight cases as well.

#### 3.4.1 Structured Blade Grid Generation

The notional X2 main rotor blade grids were generated using an in house 3D algebraic O-O grid generator. The mesh dimensions were 125x129x55. There were

125 points in the wrap around direction, 129 points in the spanwise direction, and 55 points in the normal direction. This yielded 886,875 points per blade mesh and the blade mesh is shown in Fig. 3.13.

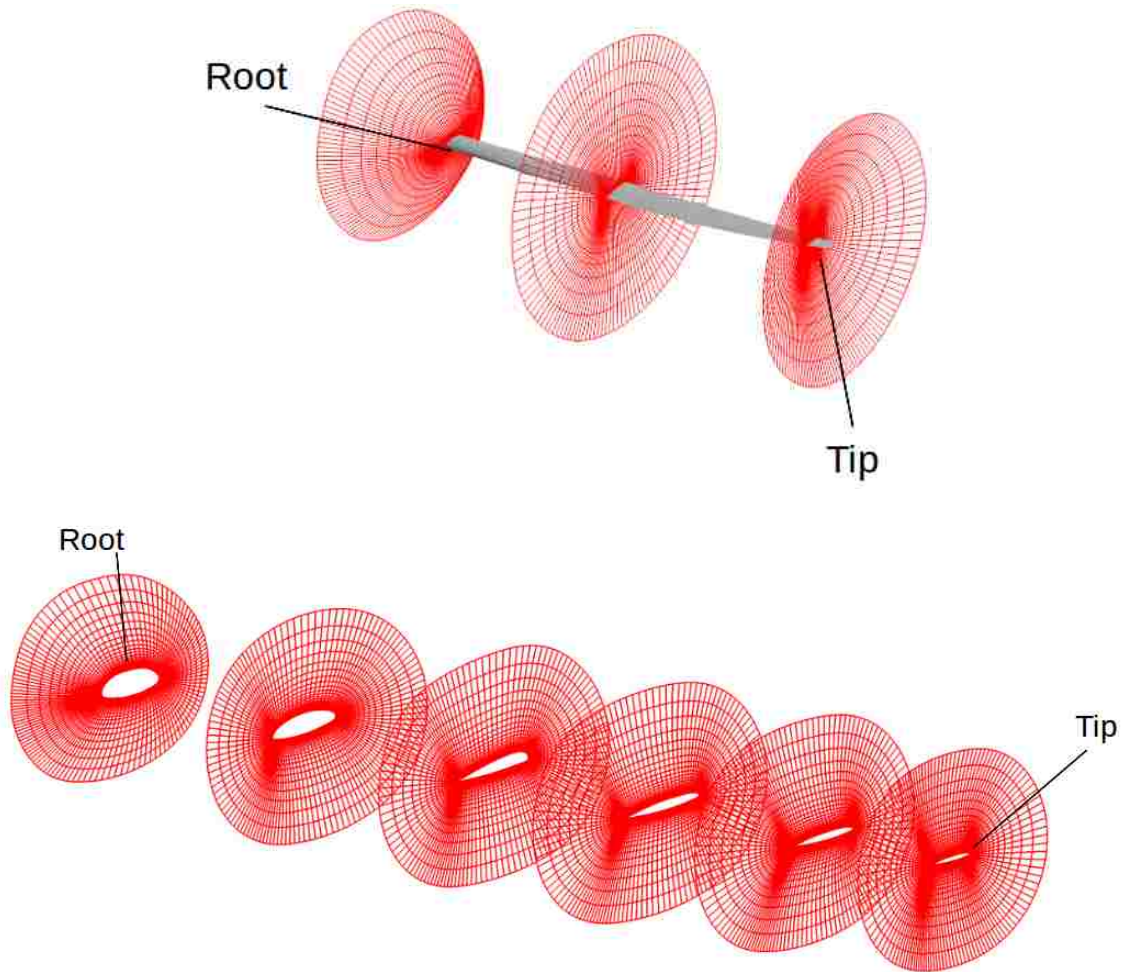


Figure 3.13: Notional X2 O-O blade mesh

A structured topology was chosen for the rotor blades for several reasons. Structured solvers, by nature, run faster than unstructured solvers and rotorcraft blade geometry is relatively straightforward to mesh with a single block structured grid. Secondly, structured solvers have higher order spatial schemes (up to 5<sup>th</sup> order) that can be taken advantage of at run time where as unstructured codes can at best



only achieve  $3^{rd}$  order or an effective  $2^{nd}$  order accuracy. Finally, since the CFD-CSD coupling process requires high fidelity resolution of aerodynamic loads on the main rotor blades, a structured solver was required.

An O-O mesh topology was chosen over a C-O grid topology due to inherent advantages exhibited by how the O-O meshes deal with the blade root and tip regions. With a C-O grid, highly skewed cells in the wake cut region and at the back of the TE may occur as the C mesh closes around the tip and root regions of the blade. Since the rotor blade tip region is where the trailed tip vortices and vortex roll up occurs, it is extremely important to ensure the grid system in this region has the highest mesh cell quality attainable to accurately capture this key physical phenomenon. The O-O mesh generator was found to do a better job at resolving this region than the C-O mesh generator. Further, the O-O grid generator does not need a wake cut region behind the airfoil like the C grid topologies. Removing this restriction allows for optimization of grid points around the airfoil surface and reduction in the total number of mesh points. Tip and root cap meshes or (collar meshes) were not found to be needed for the current calculations.

### 3.4.2 Unstructured Fuselage Grid Generation

The three fuselage geometries of the notional X2 from CAD were used to generate unstructured volume meshes. The fuselage geometry was modeled with unstructured grids due to the ease of generating fast and accurate grids around complex geometries. An equivalent structured grid would be a multi-block surface

mesh (and sometimes overset), requiring more points and considerably more time to generate. While the unstructured solver has a reduced order of accuracy compared to the structured solver, it is not expected to affect the fuselage aerodynamics to as great an extent as the rotor. This is because the fuselage meshes in the CFD were included in the flow solution to see their global interactional effect on the main rotor wake structure (captured by the Cartesian off-body grids) as well as if those effects changed the rotor blades aerodynamic loading. Since the CFD-CSD coupling process was only updating the main rotor blade aerodynamic look up tables, the order of accuracy given by the unstructured solver was deemed more than adequate for the role the fuselage is playing in these simulations.

The unstructured fuselage grids were generated from a baseline triangular unstructured surface mesh of the CAD geometry. From this surface mesh, an unstructured volume mesh was generated. The volume mesh grows prismatic cells off the fuselage surface to ensure adequate resolution of the boundary layer for viscous flows, and marches out from the boundary layer surface until the rest of the volume grid can be populated by isotropic tetrahedra. This topology is represented in Fig. 3.14. Since the Cartesian off-body meshes is designed to capture the interactional and wake effects between the rotor system blade meshes and the fuselage mesh, the fuselage volume mesh only extends 1 blade root chord length off of the surface.

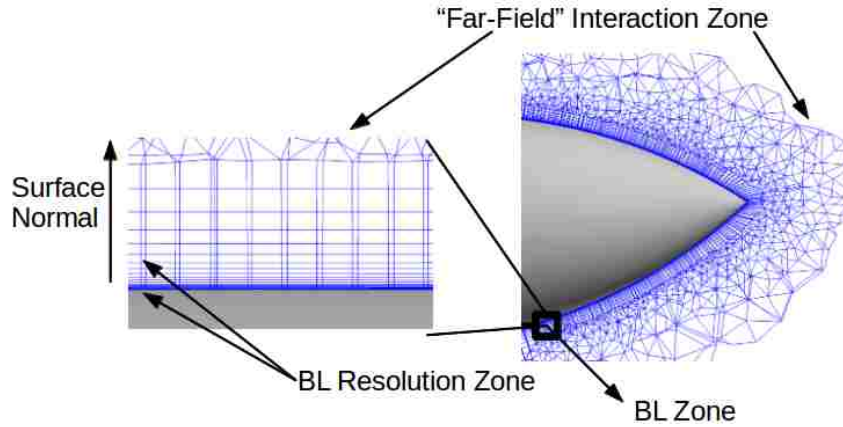


Figure 3.14: Example of prismatic boundary layer cell growth off body surface

At run time, the Cartesian background grids, fuselage mesh, and blade meshes all form an overset group and the flow solver will move the blade meshes and use Implicit Hole Cutting techniques with donor and receiver points to exchange information across flow fields various overset meshes in the CFD solver.

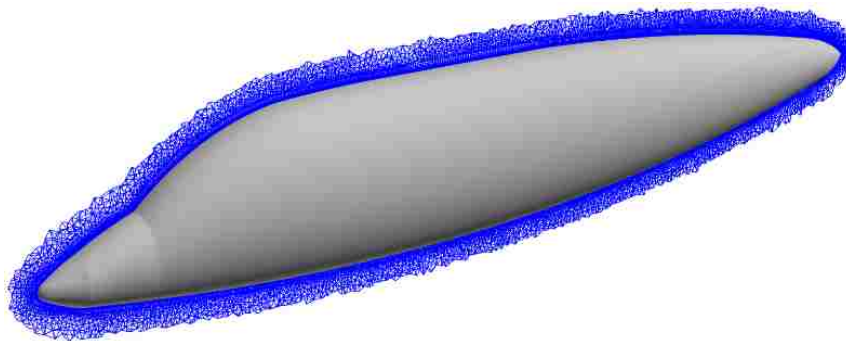


Figure 3.15: Unstructured simple fuselage mesh

The first fuselage considered in this study contains 5.8 million nodes and 12.5 million elements and is shown in Fig. 3.15. The second fuselage shape adds the lower hub fairing between the lower rotor and the fuselage body as well as the horizontal and vertical tails. To ensure high cell quality and adequate surface resolution for

the tail geometries, the number of nodes increases to 11 million with 66 million elements in this mesh. Finally, the third fuselage configuration adds a cylindrical mast between the rotor hubs. This mesh also has 11 million nodes and 66 million elements. The second and third fuselage meshes are shown in Figs. 3.16 and 3.17 respectively.

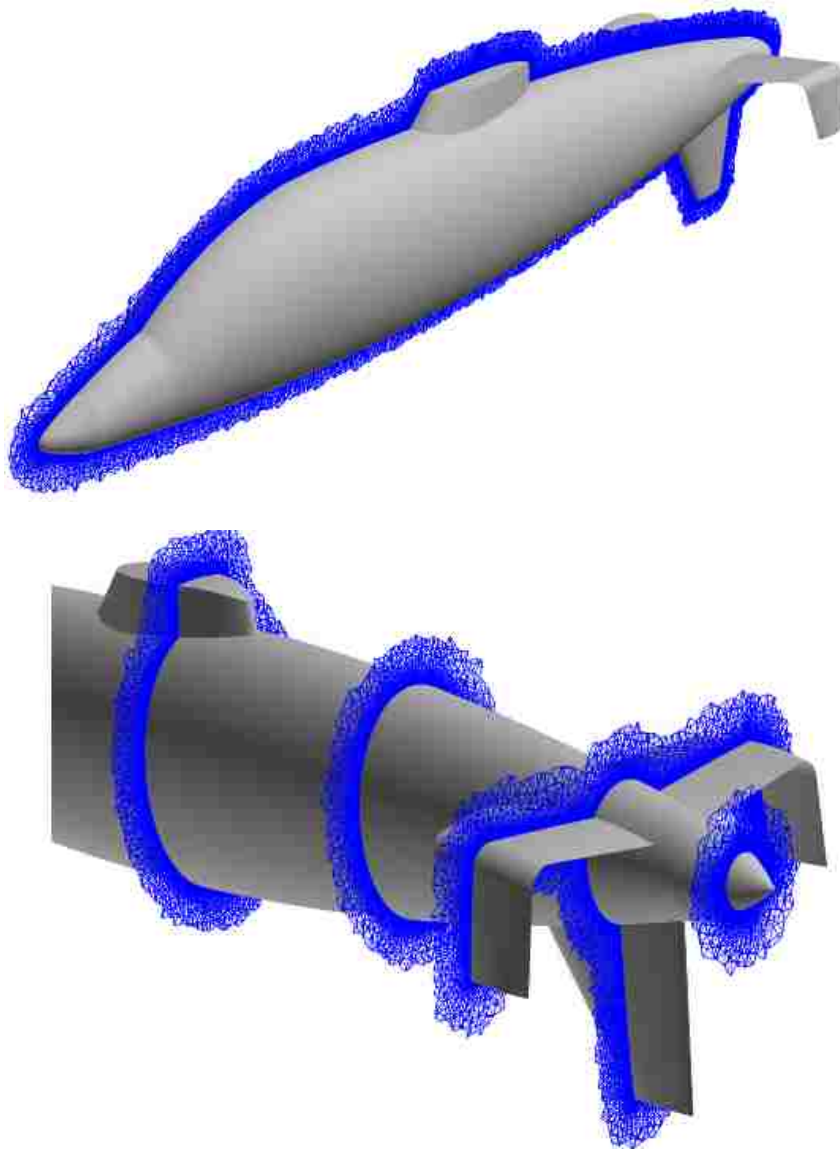


Figure 3.16: Unstructured complex fuselage mesh

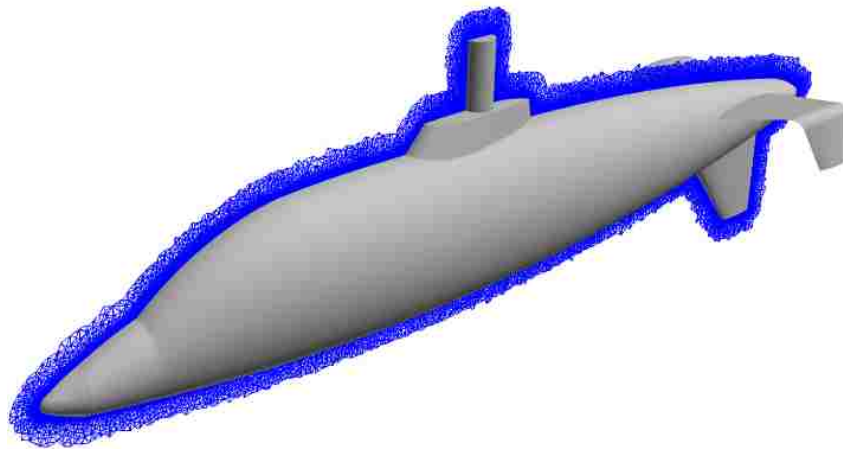
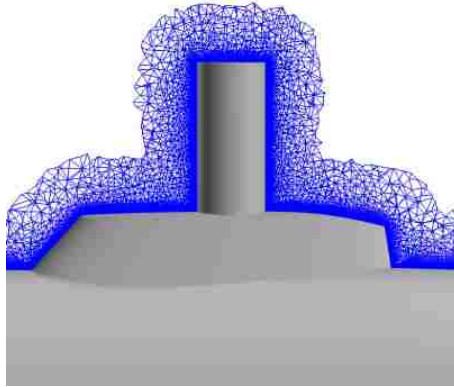


Figure 3.17: Unstructured complex fuselage with mast mesh

### 3.4.3 Overset Meshing, Co-ordinate System, and Sign Conventions

The notional X2 model in the CFD solver consists of the 8 bladed coaxial rotor system and a choice of one of the three associative fuselage mesh. The 8 rotor blade meshes and fuselage mesh are overset with the off-body Cartesian background grids. The blade meshes will rotate and deform at each time step according to the prescribed blade motions obtained from the CSD solver. Implicit hole cutting of the overset grids is also performed at each time step to interconnect the various overset grids via donor and receiver mesh point tagging ensuring domain connectivity.

The off-body nested cartesian meshes remain the same for all the forward flight cases in this study. The center of the lower rotor hub is the global (0,0,0) origin of the CFD simulation. The farfield boundaries are 154 blade root chord lengths in the x, y, z direction from the origin with an equal outer cell spacing of 6.5 blade root chords. There are then 7 refinement levels of constant cell spacing before reaching the fine level inner Cartesian mesh that encompasses the rotor system. The finest level Cartesian off-body mesh has an equal size cell spacing of 0.1 chords. The domain extent of this fine region is shown in Table 3.3.

<b>Xmin</b>	-24	<b>Xmax</b>	40
<b>Ymin</b>	-24	<b>Ymax</b>	-24
<b>Zmin</b>	-20	<b>Zmax</b>	8

Table 3.3: Fine level Cartesian Off-body domain extents in units of blade root chord lengths

The total number of mesh points for all 8 blade grids is 7.1 million. There are 115.2 million total mesh points in the off-body Cartesian meshes and roughly 66 million elements in the more detailed fuselage meshes. Having all three components in the CFD domain brings the total simulation mesh points to 188.3 million.

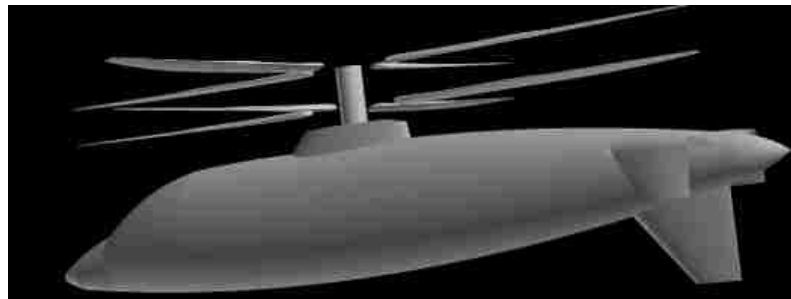
The auxiliary propeller is not included in the CFD model and is only represented as a single thrust vector in the CSD solver. This was done to greatly simplify the overall CFD-CSD coupling process and avoided having to build a notional propeller model. A disadvantage of modeling the propeller in the CFD is the penalty taken with time accuracy. For all these simulations in forward flight, a CFD time

step is every 1/4 degree of rotor azimuth. Since the propeller is spinning at a greater rate than the main rotor system, the CFD time step would have to be reduced by an order of magnitude to ensure time accuracy if a full propeller model was included. Adding a propeller model would also complicate the overset meshing and would add more points, slowing down simulation time. It is for these reasons that a propeller model was chosen to be excluded from the CFD simulation at this time, and this study only looks at rotor-rotor and rotor-fuselage interactional aerodynamics. A comparison between the X2TD and the notional X2 CFD model is shown in Fig.

3.18



(a) X2TD



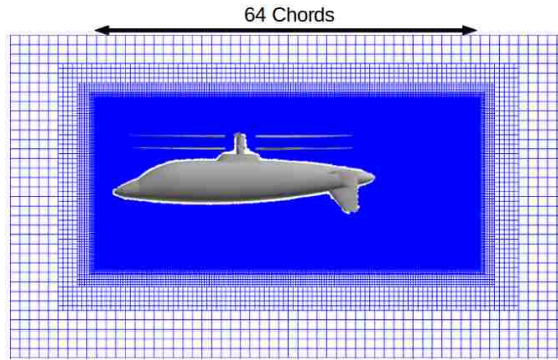
(b) Notional X2 CFD model

Figure 3.18: Comparison between X2TD and CFD notional X2 model

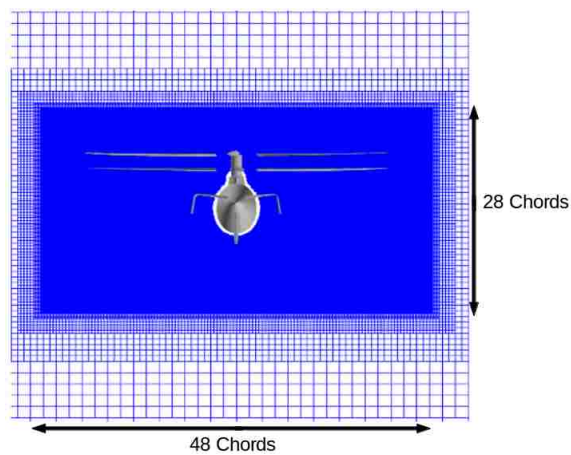
The 8 bladed coaxial rotor and the fuselage mesh are overset on the off-body

Cartesian meshes and the finest level contains the vehicle. This fine region has equal spacing of 0.1 chord lengths in order to reasonably capture the trailed wake from the rotor system as well as any interactional aerodynamics between the various components, while still being a relatively fast and efficient computation. A finer cell size could have been run in theory but the allowable wait time for simulation results would be unacceptable. Thus, the finest level  $dx$  of 0.1 chord lengths was chosen as a compromise between cell resolution and simulation time and available compute resources. The overset mesh system is illustrated in Fig. ??.





(a) Side View



(b) Rear View

Figure 3.19: CFD overset mesh system for notional X2

??

## Sign Conventions

Blade aerodynamic loads for both the CSD and the CFD solvers follow the same rotating blade deformed co-ordinate system and sign convention which is shown in Fig 3.20. Airloads transfer occurs in the deformed frame of reference, which is the reference system for the blade cross sections. The non-dimensional blade aerodynamic loads are  $C_c M^2$  (chordwise force),  $C_n M^2$  (normal force), and  $C_m M^2$

(pitching moment). To make it simple, both solvers share the same sign convention for these three deformed forces and both CCW and CW rotors also share the same sign convention (see Table 3.4.

Force	CSD (+ve)	CFD (+ve)	CSD (-ve)	CFD (-ve)
$C_c M^2$	towards LE	towards LE	towards TE	towards TE
$C_n M^2$	Up	Up	Down	Down
$C_m M^2$	nose-up	nose-up	nose-down	nose-down

Table 3.4: Deformed frame aerodynamic loads: sign convention

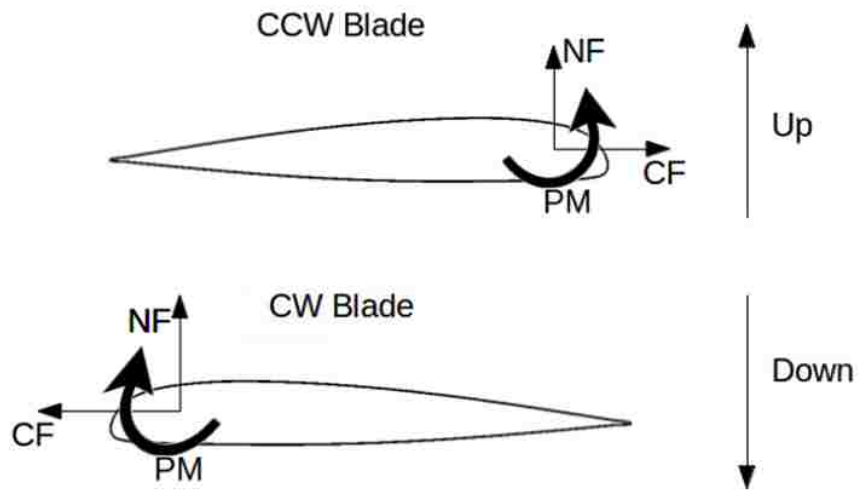


Figure 3.20: Blade Airloads co-ordinate system

## Chapter 4: Forward Flight Results: Isolated Rotor System

### 4.1 Overview

Three forward flight speeds, 55, 100, 150 knots were carried out on HPC clusters parallelized through MPI using 240 processors per run. It took 5 hours per rotor revolution on the AFRL and ARL HPC clusters. For all these forward flight cases, convergence was achieved after 4 CFD-CSD coupling cycles, or a total of 8 simulated rotor revolutions in CFD per flight condition (9,600 CPU hours). An isolated coaxial rotor system (i.e. no fuselage model in CFD) was simulated at these three flight speeds to quantify rotor-rotor interactional aerodynamics. Aside from these cases, at 55 and 150 knots, single isolated rotor runs were also executed. These runs took the same flow field conditions and exact same prescribed blade motions as the coaxial rotor cases, however the upper and lower rotors were run in isolation to remove the interference effect. These were then compared to the coaxial rotor cases to illustrate the inter rotor interactional effects on blade aerodynamic loads at both a low speed condition (55 knots) and a moderately high speed condition (150 knots).

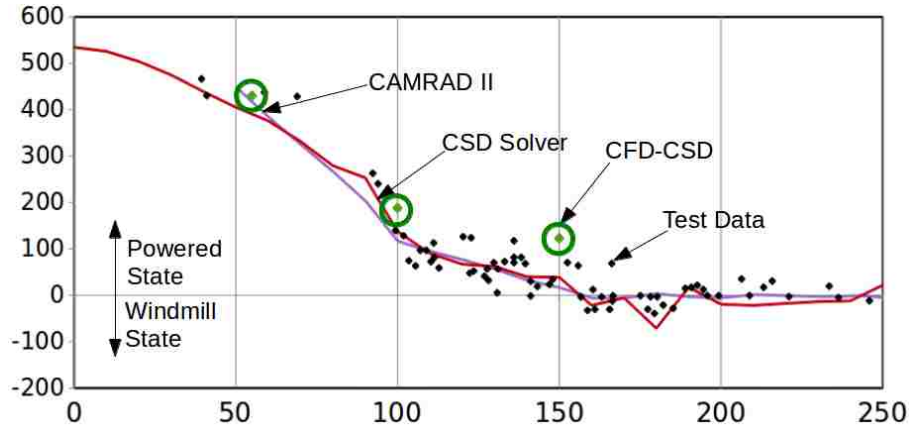


Figure 4.1: Predicted vs. measured coaxial rotor power for the Sikorsky X2

As can be seen from Figure 4.1, the CFD-CSD predicted power at 55, 100, and 150 knots have good agreement with the baseline CSD prediction and lie within the Sikorsky X2 test data scatter. The 150 knots CFD-CSD coupled case has the poorest correlation of the three runs and further parametric studies need to be conducted at this flight speed, it is hypothesized that at this flight condition the propeller (currently not modeled in the CFD) is becoming the dominant component that drives both vehicle trim and total rotor power.

## 4.2 55 Knots

The first coupled forward flight simulation performed was at 55 knots. The advance ratio is 0.15, which lies outside of the transition flight zone for conventional single main rotor helicopters. Due to the low vertical spacing between the upper and lower rotors (18 inches), it is expected that the upper rotor wake will intersect the rear half of the lower rotor producing noticeable interference effects. As the advance

ratio increases, it is expected that the rotor wake trajectories will change, as they will be increasingly blown backwards by stronger free stream velocities. This should then lower the rotor-rotor interference as forward speed increases.

<b>55 Knots</b>	<b>CSD</b>	<b>CFD-CSD</b>
<b>Collective (deg)</b>	8.61 (CCW)	9.45 (CCW)
	9.26 (CW)	9.39 (CW)
<b>Cyclic <math>\theta_{1C}</math> (deg)</b>	4.44 (CCW)	3.29 (CCW)
	4.44 (CW)	3.29 (CW)
<b>Cyclic <math>\theta_{1S}</math> (deg)</b>	-2.95 (CCW)	-3.65 (CCW)
	2.52 (CW)	3.16 (CW)
<b>Fuselage Pitch (deg)</b>	-0.43	-0.44
<b>Total Thrust (lbs)</b>	5913.2	5908.6
<b>Total Power (hp)</b>	431	430

Table 4.1: Comparison between initial CSD and CFD-CSD trim solutions at 55 knots

The rotor controls for both the initial CSD and final CFD-CSD Trim solutions at 55 knots are shown in Table 4.1. The upper rotor (CCW) has an increase in collective from the initial CSD trim solution, bringing both rotors to nearly identical collective pitch settings. The cyclic pitch  $\theta_{1C}$  decreases which indicates a shift in the longitudinal bias of rotor thrust towards the inboard sections. The lateral pitch  $\theta_{1S}$  contains both the lift offset control and the flight dynamic control. The flight dynamic control remains mostly unchanged, however the lift offset control magnitude

increased. The increased magnitude in lift offset control reflects a redistribution of the airloads to the blade tips on the advancing sides. The fuselage pitch is mostly driven by the propeller thrust, horizontal tail lift, and rotor forces and pitching moments. At 55 knots, the propeller is effectively inactive and the horizontal tail lift is negligible. It is no surprise then, that the fuselage pitch attitude stays nearly the same between initial CSD and final CFD-CSD. Total rotor power remains unchanged and is indicative of the comprehensive analysis ability to capture time-averaged quantities for design considerations.

## CFD-CSD Convergence

There are many metrics to examine for CFD-CSD convergence. The rotor controls should converge over coupling iterations as well as the airloads. The delta of the delta airloads should also drive to zero. Figure 4.2 shows rotors controls, collective and cyclics, vs. coupling iteration. The controls monotonically converge during the coupling iterations, with the upper rotor (CCW) seeing a slight increase in collective. The Largest changes occur between the first and second coupling iterations with relatively small changes between the third and fourth coupling iterations. Thus, four runs with CFD seem to be sufficient for convergence of the rotor controls.

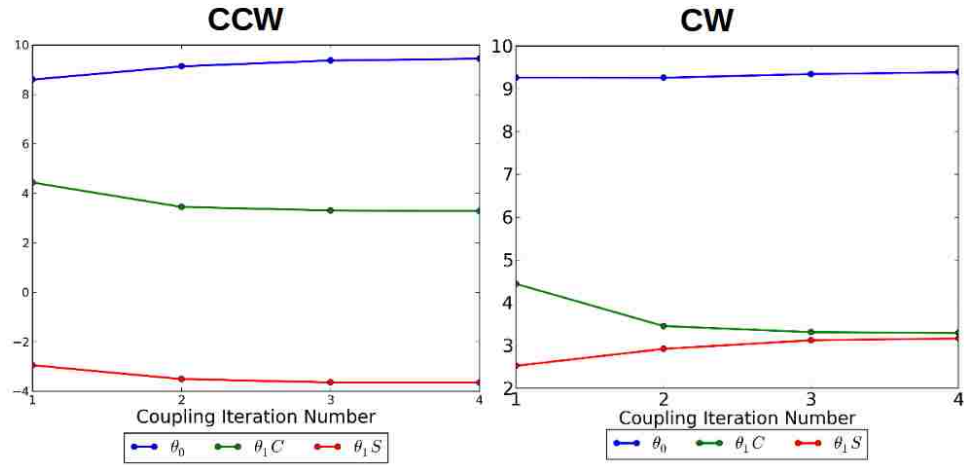


Figure 4.2: Convergence of rotor controls (deg) with CFD-CSD iterations at 55 knots

Figures 4.3, 4.4, and 4.5 illustrate deformed frame convergence of the unsteady aerodynamic time histories of chord force, normal force, and pitching moments at various span-wise stations at 55 knots. Each coupling iteration contains two revolutions of CFD and by revolution 8, all span wise locations across all three aerodynamic sectional forces/moments have converged. It should be noted that the x axis denotes the azimuth in the CCW direction. This means that for the CW rotor plots, the advancing side is 360-180 degrees on the x axis. This convention will be used throughout the thesis for all line plots for which the x axis is azimuth in degrees.

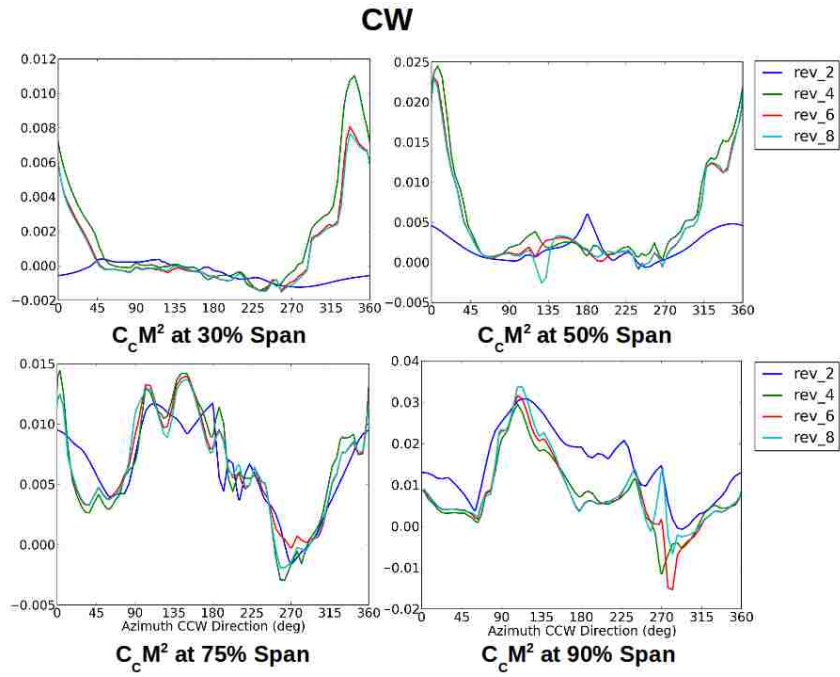
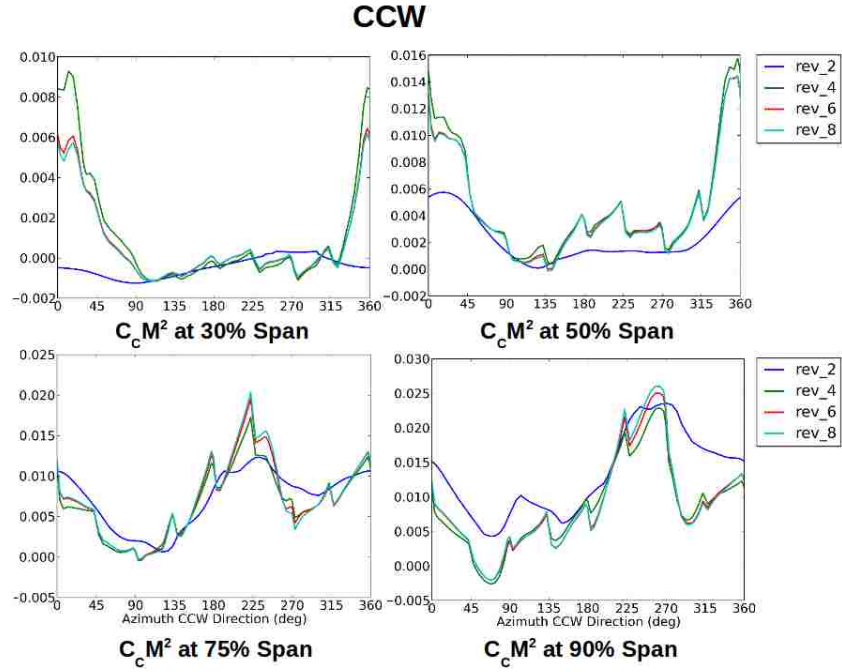


Figure 4.3: Convergence Of  $C_c M^2$  at 55 Knots



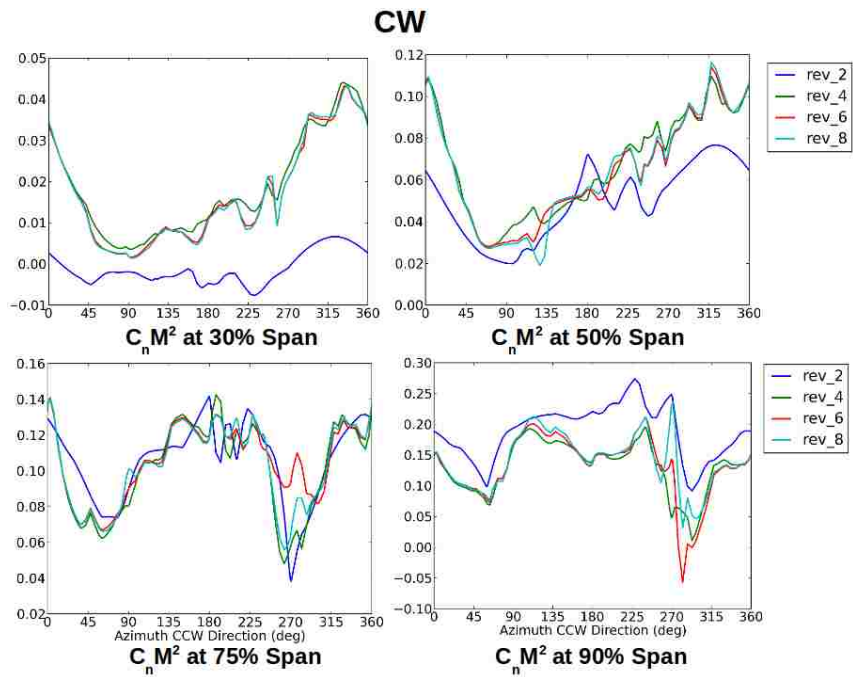
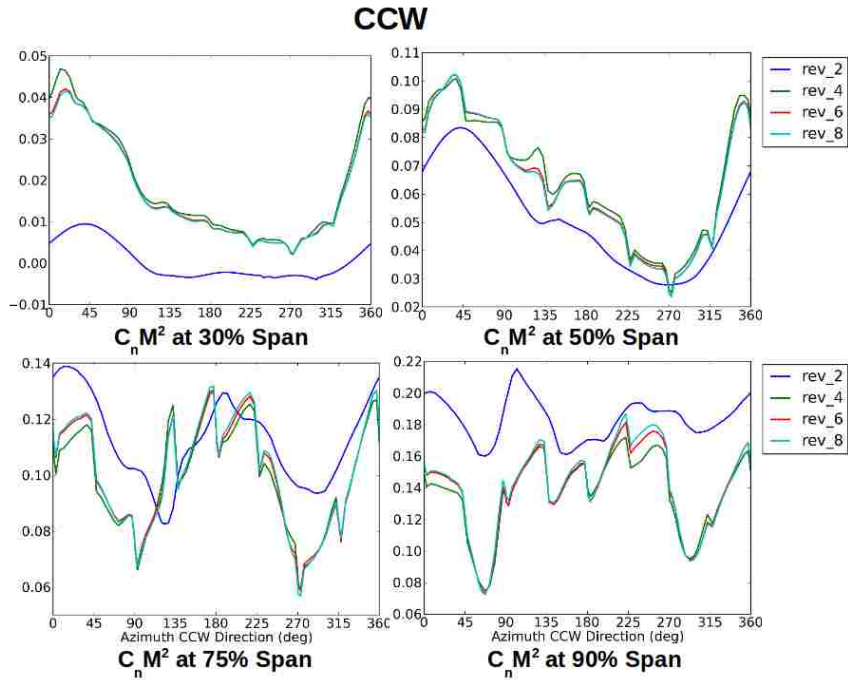


Figure 4.4: Convergence Of  $C_n M^2$  at 55 Knots

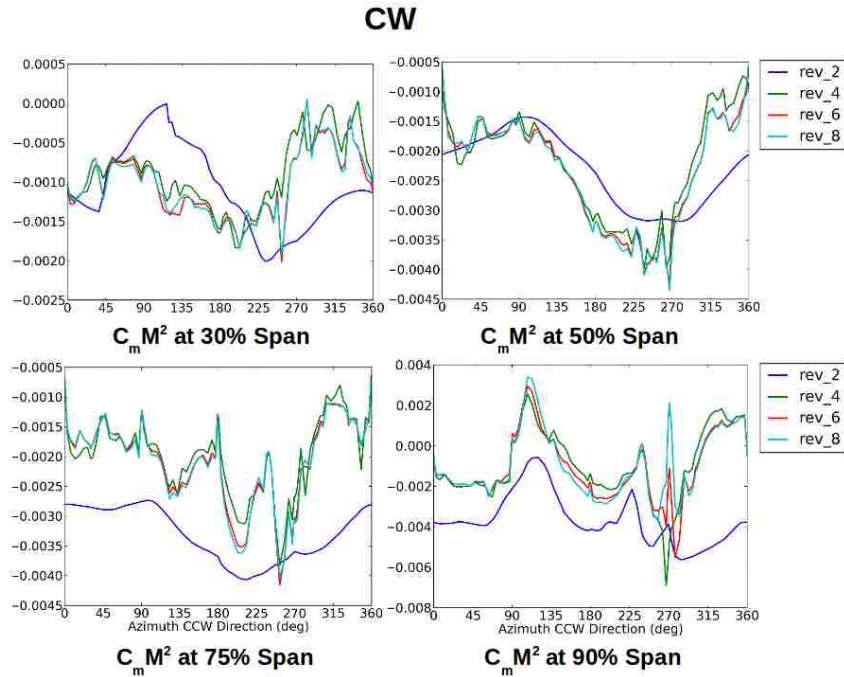
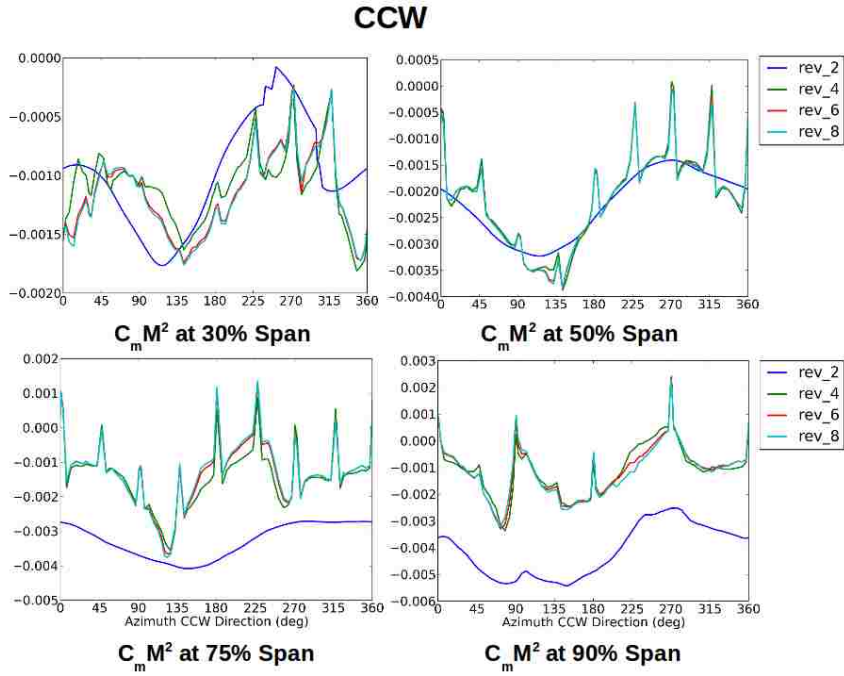


Figure 4.5: Convergence Of  $C_m M^2$  at 55 Knots

## Initial CSD vs Final CFD-CSD Rotor Aerodynamic Loads

A comparison was done between the initial CSD predicted airloads using a free wake model and the final converged CFD-CSD predicted airloads. The goal was to quantify what CFD brings in terms of predicting improved blade aerodynamic loads. From the contour plots in Figures 4.6, 4.7, and 4.8 it is apparent that the initial CSD solution does not pick up any of the impulsive  $8/\text{rev}$  content where as the CFD is able to capture this. This periodic impulsive force is most noticeable in the upper (CCW) rotor pitching moment. The  $8/\text{rev}$  signal is from blade passage events where the blades of the upper rotor and lower rotor cross over one another. There is also a reduction in normal force for the lower rotor on the advancing side with CFD-CSD over what the initial CSD solution predicts. The CFD also tends to exhibit smoother radial variations of spanwise loads across the regions of airfoil transition. The initial CSD solution can not achieve this due to the finite nature of the distinct 2D aerodynamic tables defined at discrete points along the span.

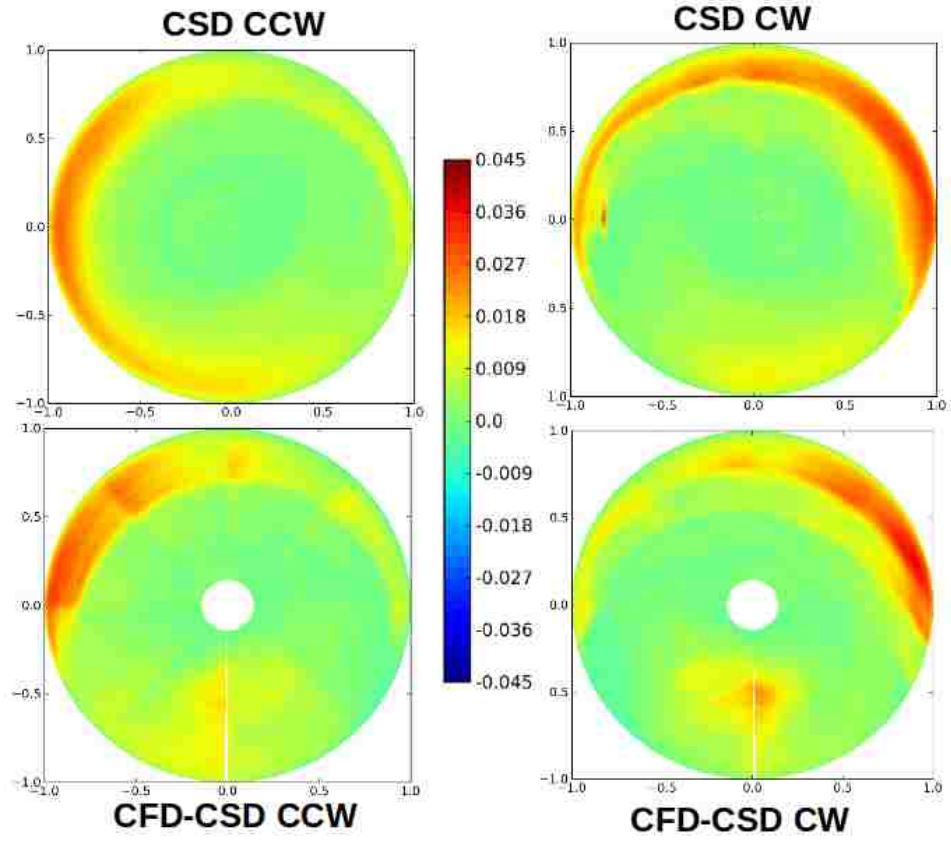


Figure 4.6: Contour plots of  $C_c M^2$  for initial CSD and final CFD-CSD at 55 knots

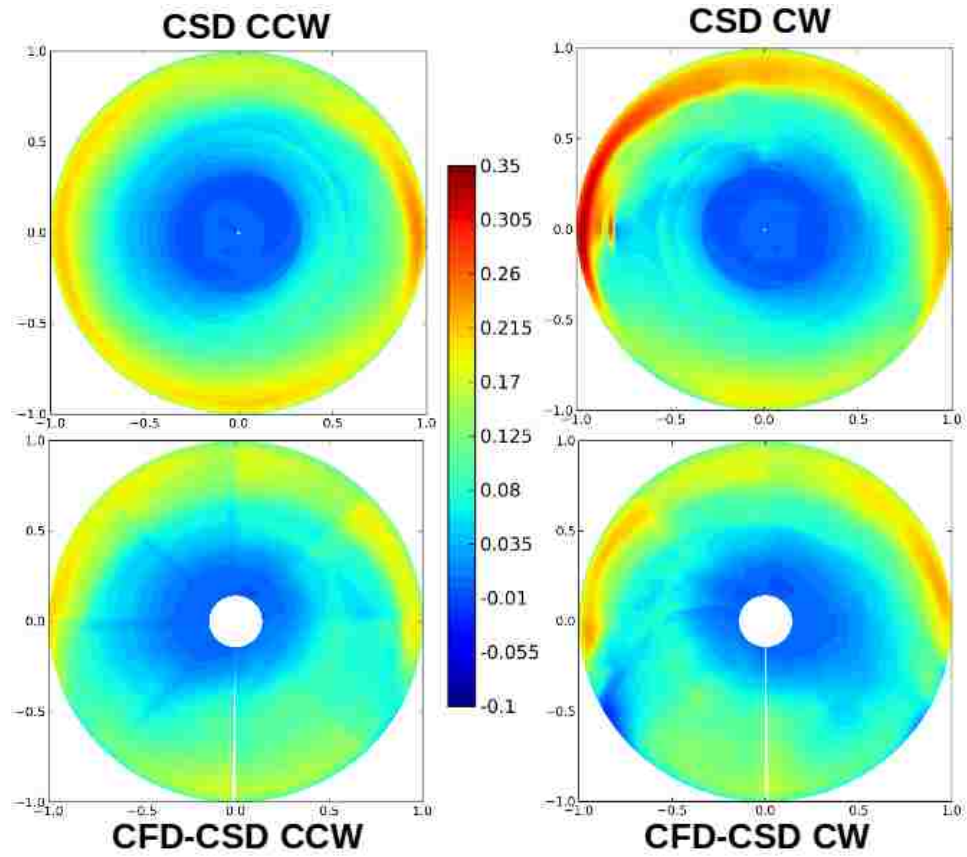


Figure 4.7: Contour plots of  $C_n M^2$  for initial CSD and final CFD-CSD at 55 knots

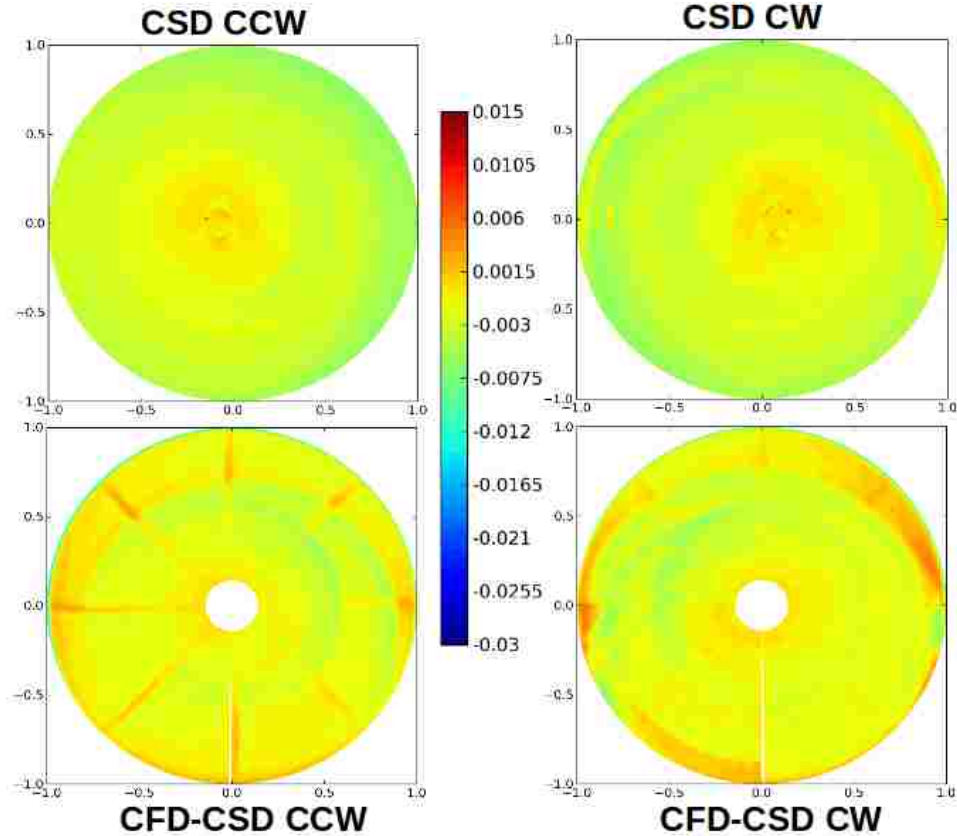
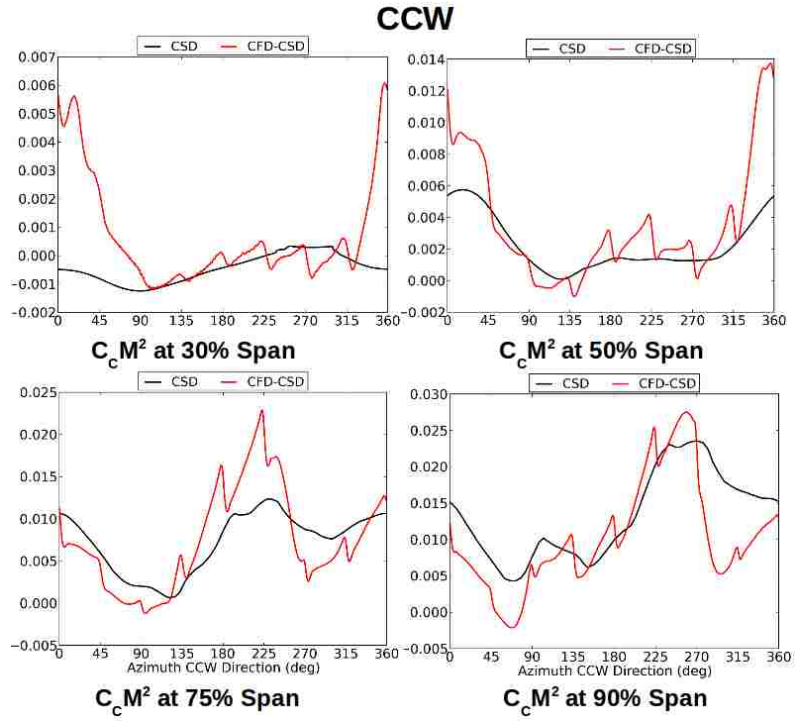


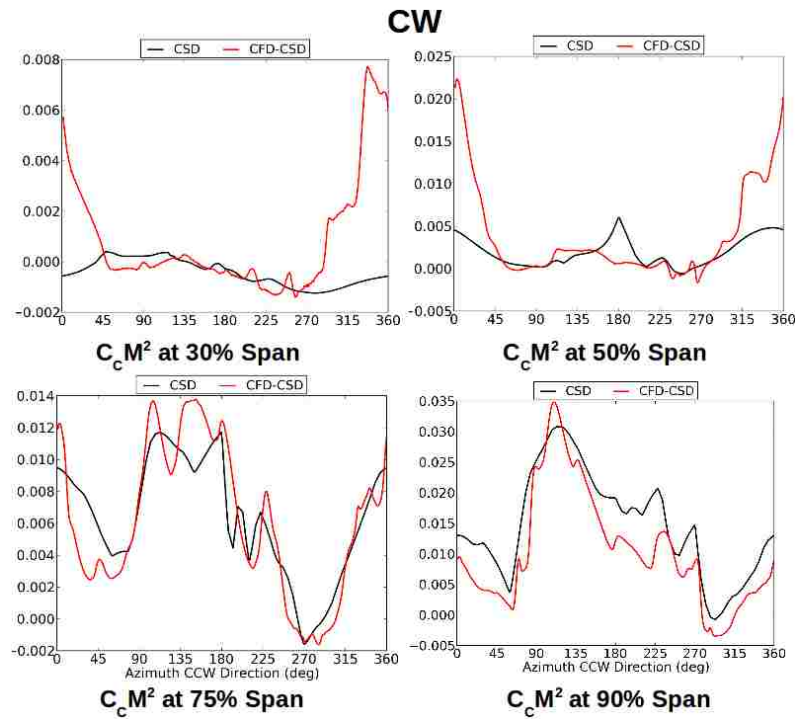
Figure 4.8: Contour plots of  $C_m M^2$  for initial CSD and final CFD-CSD at 55 knots

Line plots comparing the converged solutions between CSD using free wake and CFD-CSD provides insight into the accuracy (and deficiencies) of lower order aerodynamic methods for coaxial systems. Non-dimensional chordwise force, normal force, and pitching moment variations along the azimuth at discrete spanwise locations are shown in Figures 4.9, 4.10, and 4.11. Predictions in chordwise force show good agreement overall between the initial CSD with free wake and the CFD-CSD solution for the low frequency content (steady and 1/rev, with limited 2/rev and 3/rev content). The largest discrepancy is over the back of the rotor disk in the tail region at inboard stations. In this region, the CFD predicts much higher chordwise

force for both rotors. It was found that the upper rotor wake persists between the rotor planes near  $\Psi = 0$  (over the tail) and may be responsible for this phenomena. The free wake is unable to capture these interactions. As previously mentioned, the higher harmonic content corresponding to blade passage events is totally missed by the free wake model.



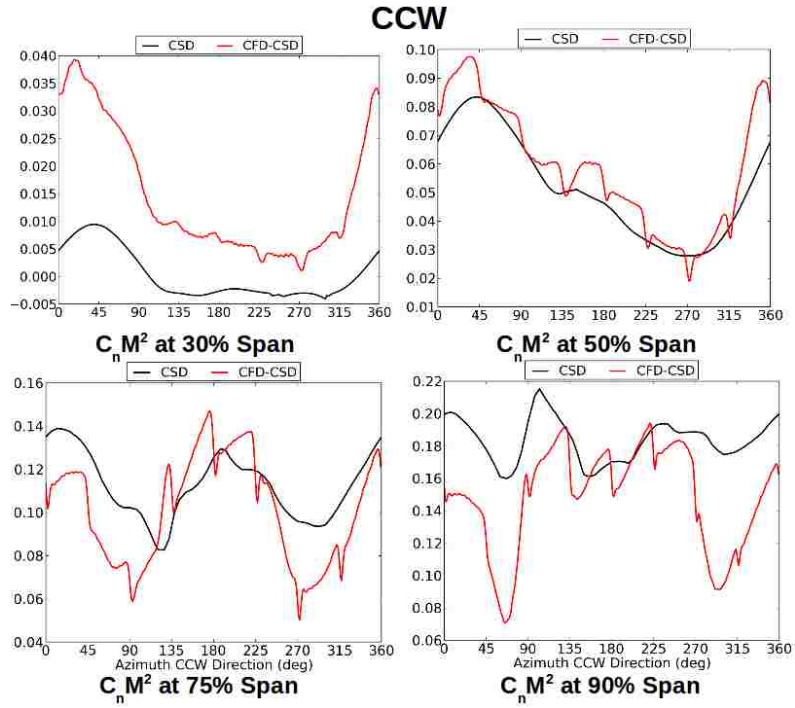
(a) Upper Rotor



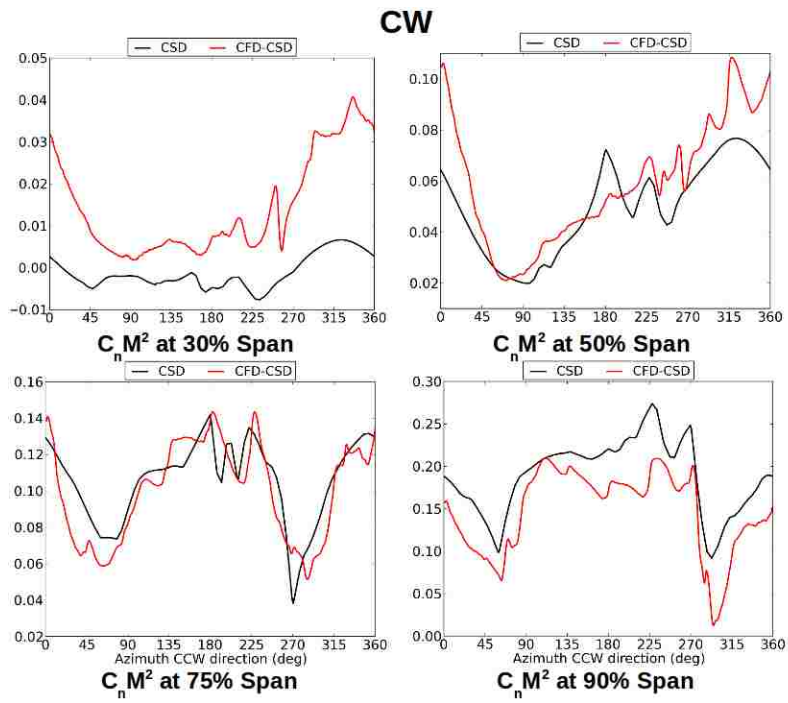
(b) Lower Rotor

Figure 4.9: Line plots of  $C_c M^2$  between initial CSD and final CFD-CSD at 55 knots



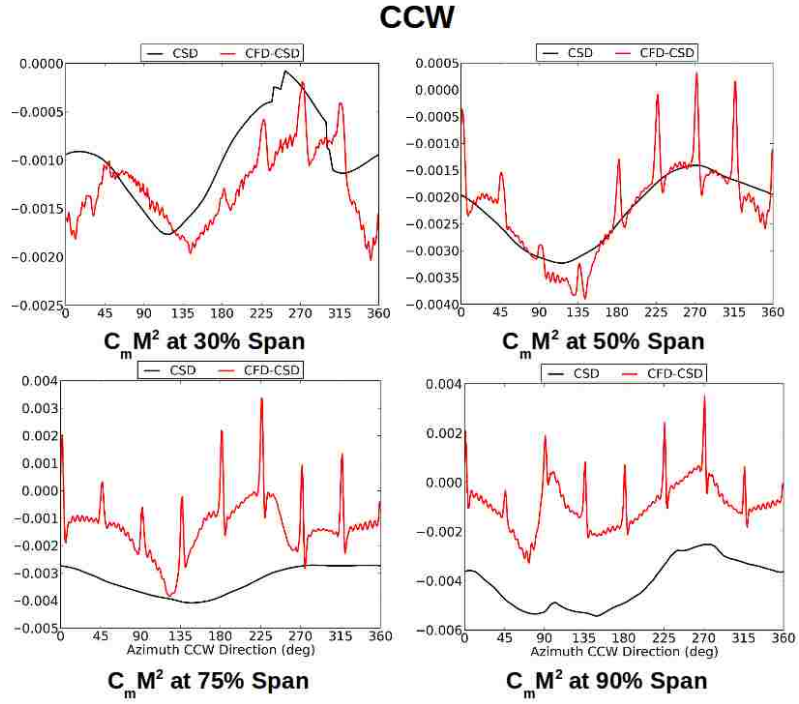


(a) Upper Rotor

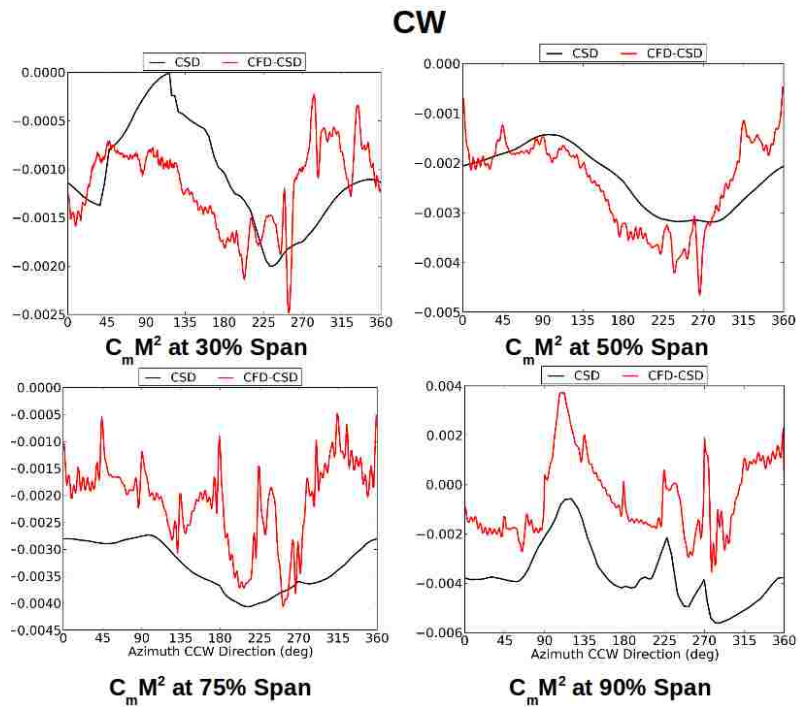


(b) Lower Rotor

Figure 4.10: Line plots of  $C_n M^2$  between initial CSD and final CFD-CSD at 55 knots



(a) Upper Rotor



(b) Lower Rotor

Figure 4.11: Line plots of  $C_m M^2$  between initial CSD and final CFD-CSD at 55 knots

Predictions of the normal force indicate that the 2D airfoil tables/free wake combination under-predict the loads over the inboard stations and over-predict at the outboard stations. The CFD redistributes the normal force towards the inboard sections of the blades and unlike the initial CSD solution, can also capture the negative loading peak on the advancing side of both rotors.

### 4.3 100 Knots

The second coupled forward flight simulation performed was at 100 knots and the advance ratio is 0.272. At this flight speed, the propeller is beginning to play a key role in the vehicle trim solution. The rotor power at this flight condition has decreased by 56% compared to 55 knots. This decrease is due in large part to the increase in propeller thrust which is starting to offload the main rotors. Unlike at 55 knots, the initial predicted power from CSD does not directly match what the final CFD-CSD coupling cycle predicts. The total main rotor thrust, however, remains fairly constant between the initial CSD solution and CFD-CSD. This suggests that the free wake model and 2D aerodynamic look up tables over-predict the rotor system efficiency.

<b>100 Knots</b>	<b>CSD</b>	<b>CFD-CSD</b>
<b>Collective (deg)</b>	5.52( CCW)	6.48 (CCW)
	6.15 (CW)	6.28 (CW)
<b>Cyclic <math>\theta_{1C}</math> (deg)</b>	3.38 (CCW)	1.77 (CCW)
	3.38 (CW)	1.77 (CW)
<b>Cyclic <math>\theta_{1S}</math>(deg)</b>	-4.08 (CCW)	-4.44 (CCW)
	4.50 (CW)	3.77 (CW)
<b>Fuselage Pitch (deg)</b>	2.62	2.43
<b>Total Thrust (lbs)</b>	5675.4	5678.8
<b>Total Power (hp)</b>	160.2	187.7

Table 4.2: Comparison between initial CSD and CFD-CSD trim solutions at 100 knots

Like in the 55 knots case, at 100 knots the use of CFD-CSD coupling brings both rotors closer to the same collective pitch setting compared to the baseline initial CSD with free wake which has more collective pitch on the lower rotor. The predicted cyclic pitch  $\theta_{1C}$  reduces by almost half from the initial CSD value while the lateral pitch  $\theta_{1S}$  only differs slightly for both rotors. The fuselage pitch was reduced by 0.19 degrees; however, it should be noted that the fuselage pitch attitude is now tilted 2 degrees nose up, which is very different from the 55 knots value of -0.4 degrees nose down. This is a direct consequence of the propellers increasing role in providing longitudinal thrust. As the propeller thrust is increased, to maintain moment and force balance, the fuselage will pitch up to give the rotor an aft shaft

tilt to the relative wind as the rotor increasingly needs to provide less propulsive thrust but generate more vertical lift.

### CFD-CSD Convergence

Figure 4.12 shows rotors controls, collective and cyclics, vs. coupling iteration. The lower rotor (CW) sees a smooth reduction in both  $\theta_{1C}$  and  $\theta_{1S}$  over coupling cycles, where as the upper rotor sees a slight reduction in  $\theta_{1C}$  but  $\theta_{1S}$  remains fairly level. Just like 55 knots, there is a relatively smooth transition from initial to final control values during the coupling process.

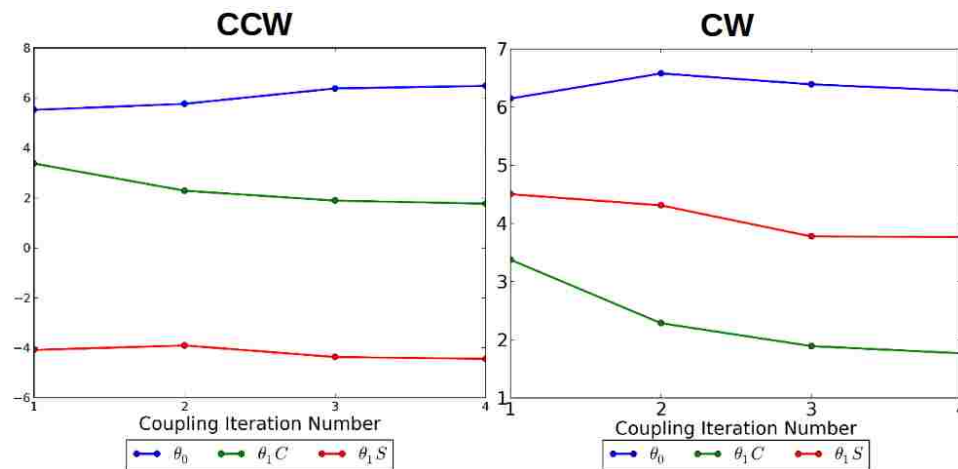
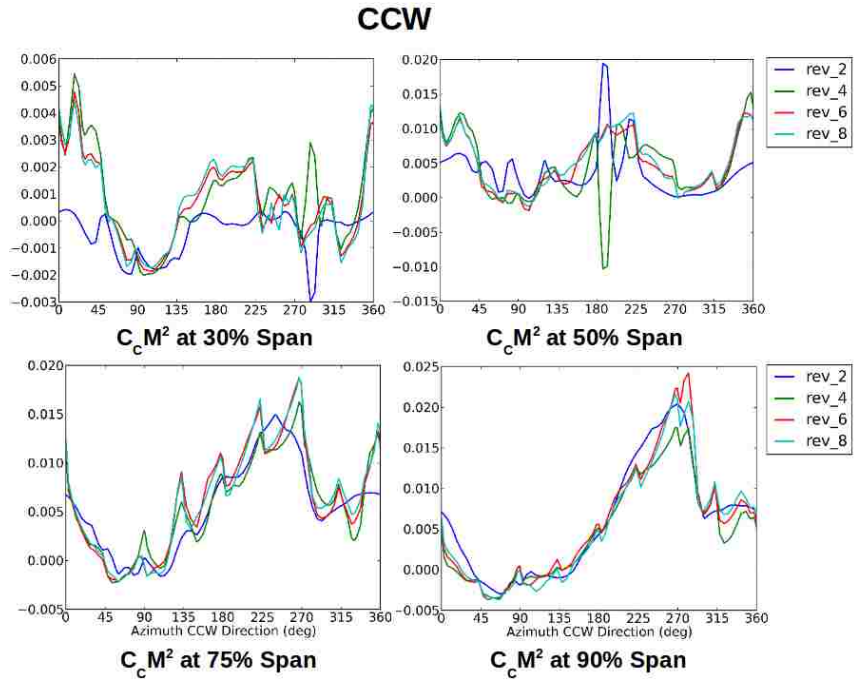
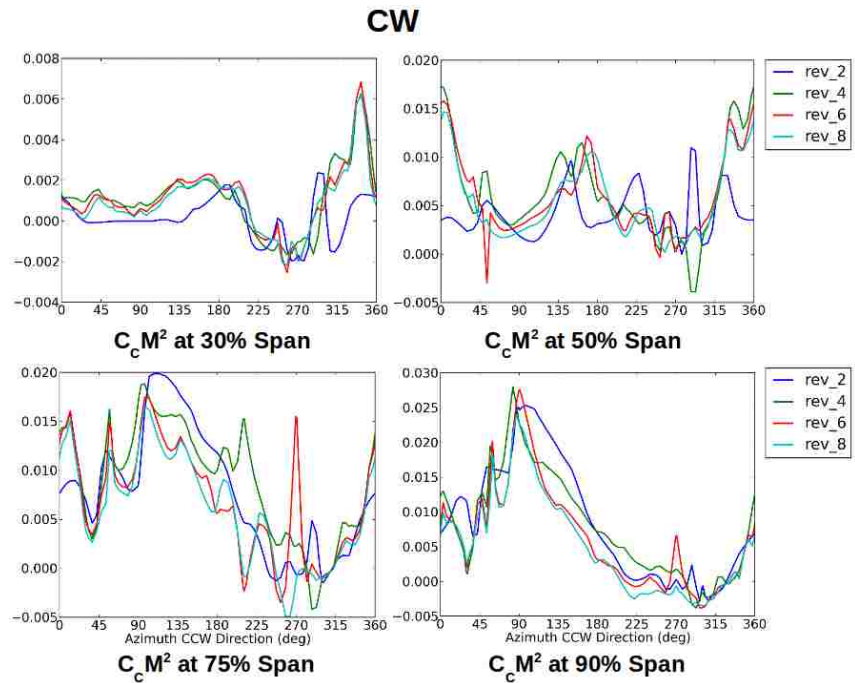


Figure 4.12: Convergence of rotor controls (deg) with CFD-CSD iterations at 100 Knots

Figures 4.13, 4.14, and 4.15 illustrate deformed frame aerodynamic force and moment convergence at 100 knots.

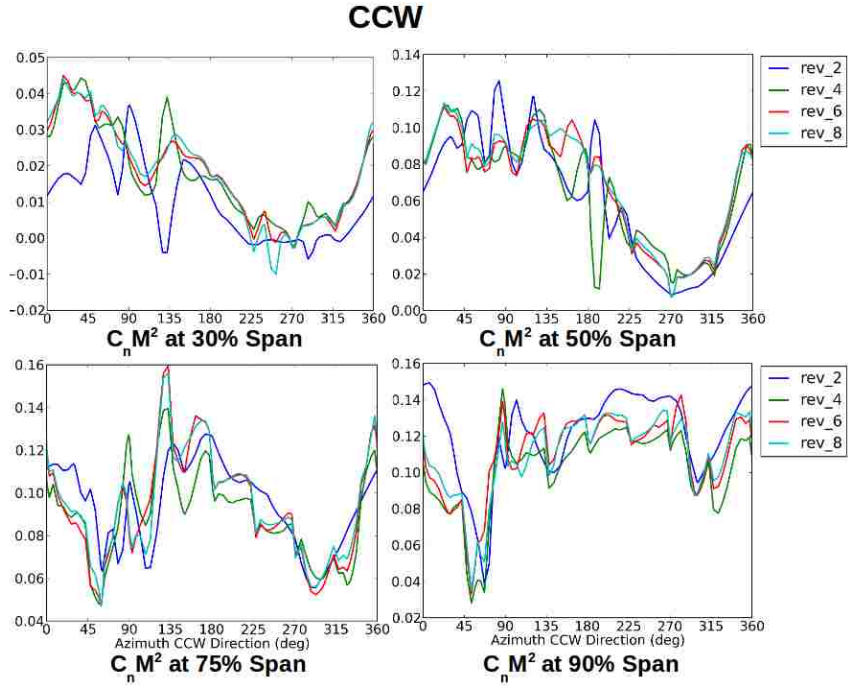


(a) Upper Rotor

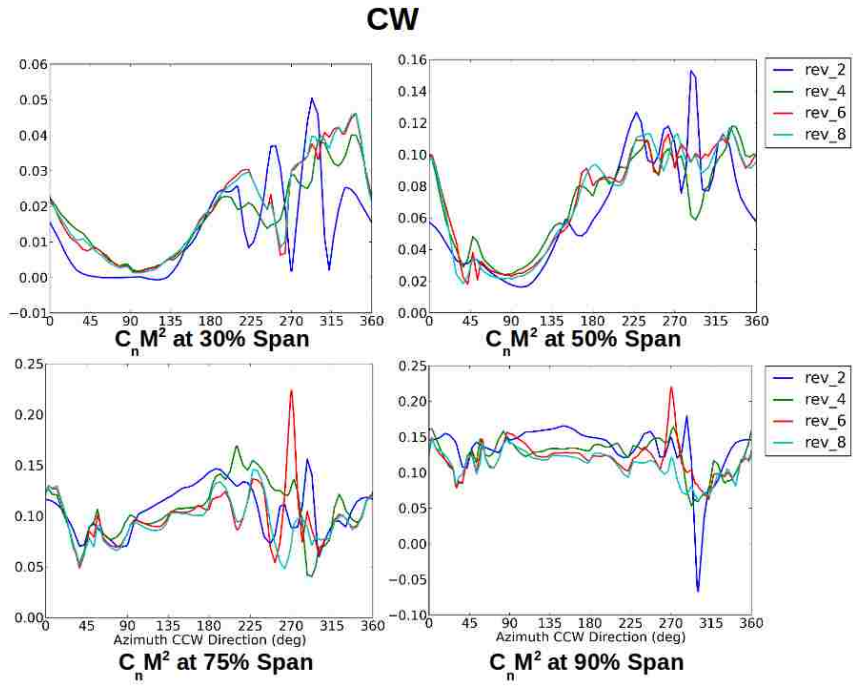


(b) Lower Rotor

Figure 4.13: Convergence of  $C_c M^2$  at 100 knots

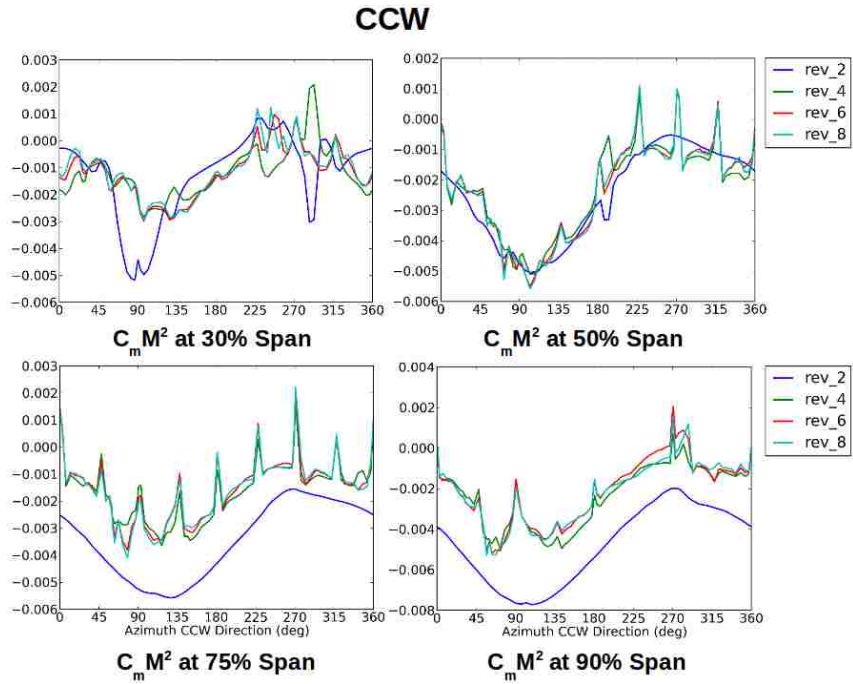


(a) Upper Rotor

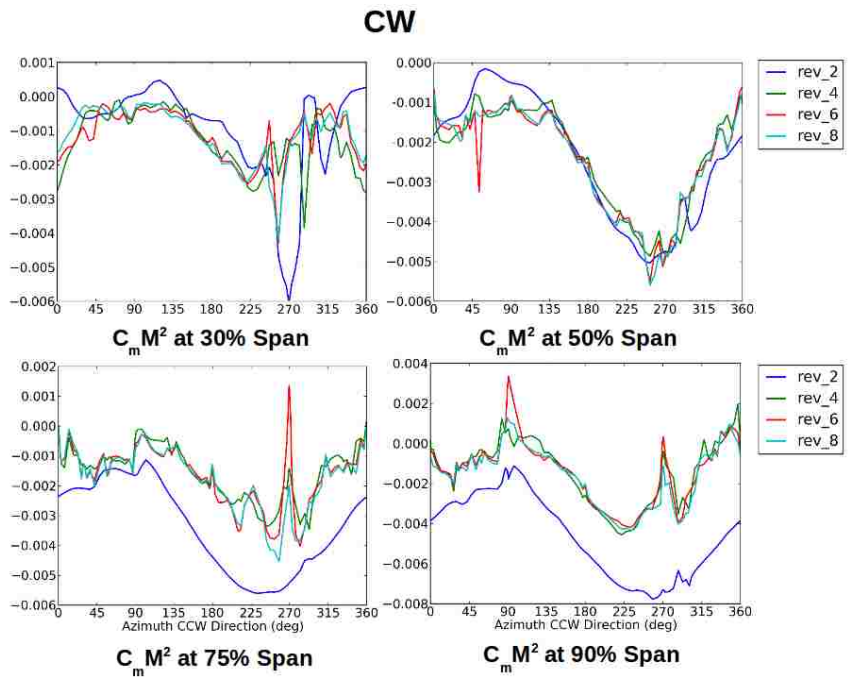


(b) Lower Rotor

Figure 4.14: Convergence of  $C_n M^2$  at 100 knots



(a) Upper Rotor



(b) Lower Rotor

Figure 4.15: Convergence of  $C_m M^2$  at 100 knots



## Initial CSD vs Final CFD-CSD Rotor Aerodynamic Loads

Just like for 55 knots, a comparison was done between the initial CSD predicted airloads using a free wake model and the final converged CFD-CSD predictions. Figures 4.16, 4.17, and 4.18 highlight the global differences between the baseline CSD and final CFD-CSD results. At 100 knots, a small reverse flow region is beginning to form on the inner portions of the blade on the retreating sides. This is most prevalent in the pitching moment contour plots. The reverse flow region is distinct in the initial CSD solution and has high variability in pitching moments dictating presence of dynamic stall events. Free wake models with 2D aerodynamic look up tables do not have the capability to always accurately resolve this flow region. The CFD solution smooths out the reverse flow region and gives a much more reasonable and continuous answer.

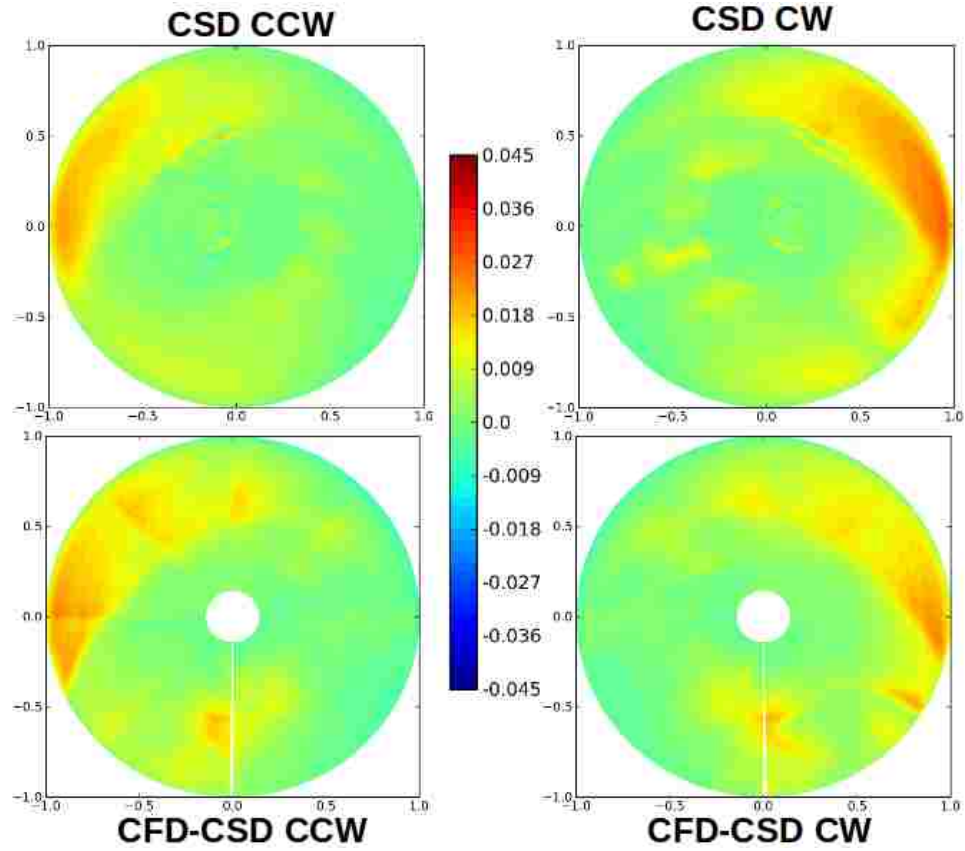


Figure 4.16: Contour plots of  $C_c M^2$  for initial CSD and final CFD-CSD at 100 knots

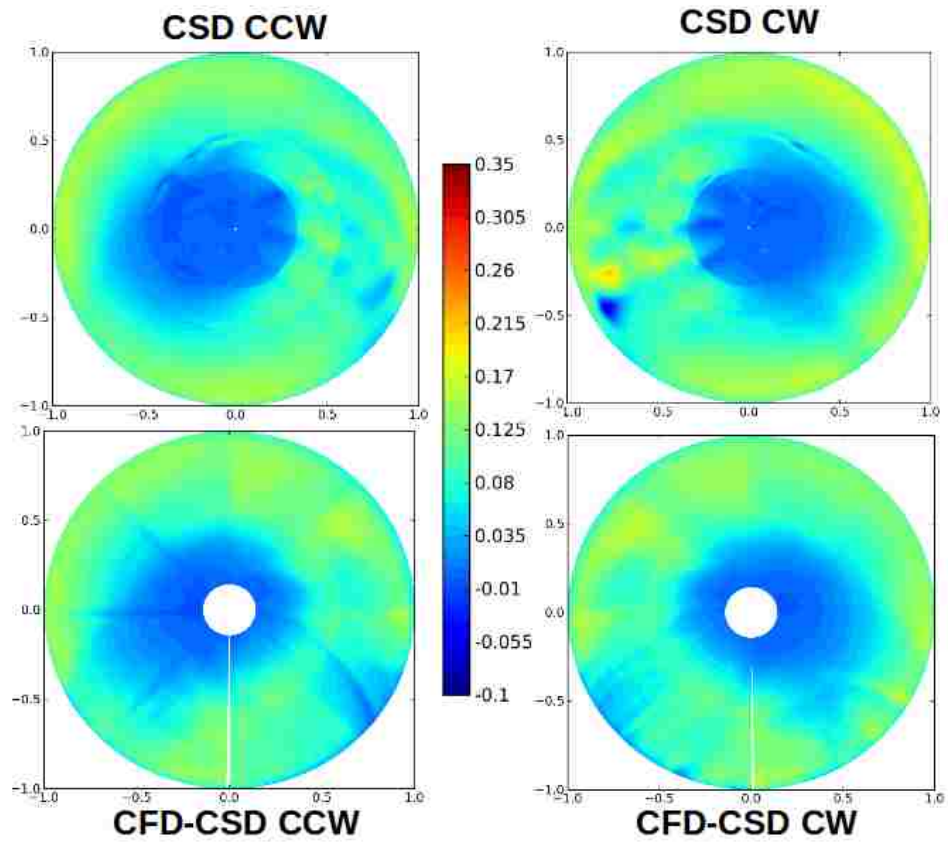


Figure 4.17: Contour plots of  $C_n M^2$  for initial CSD and final CFD-CSD at 100 knots

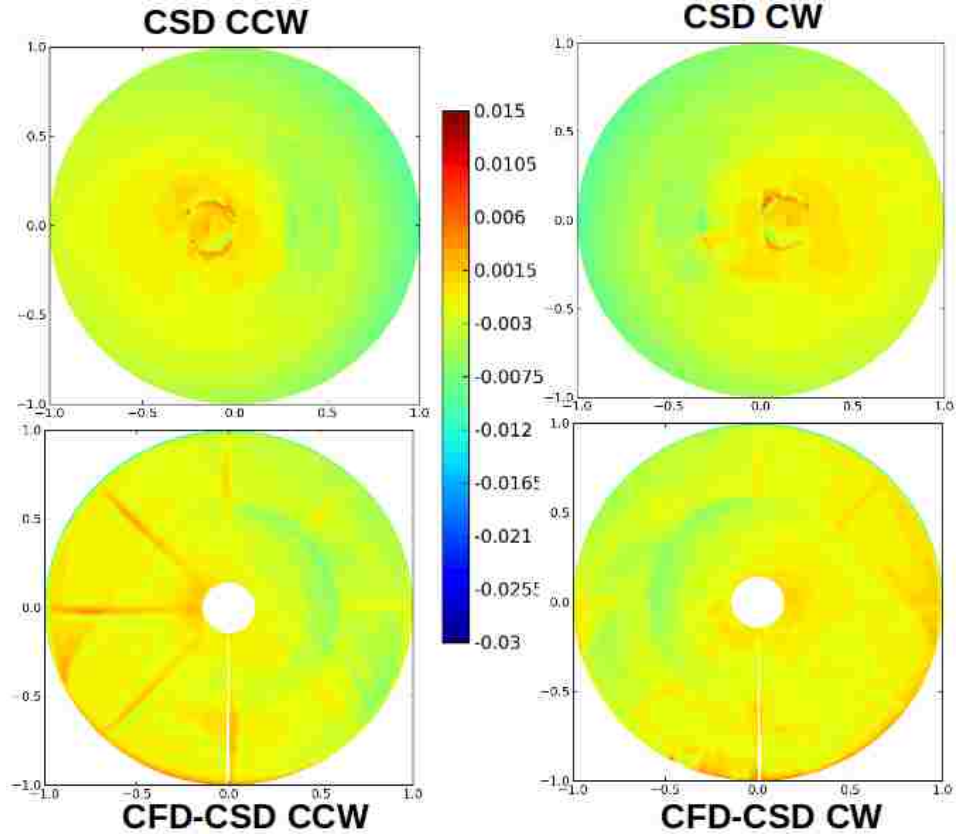
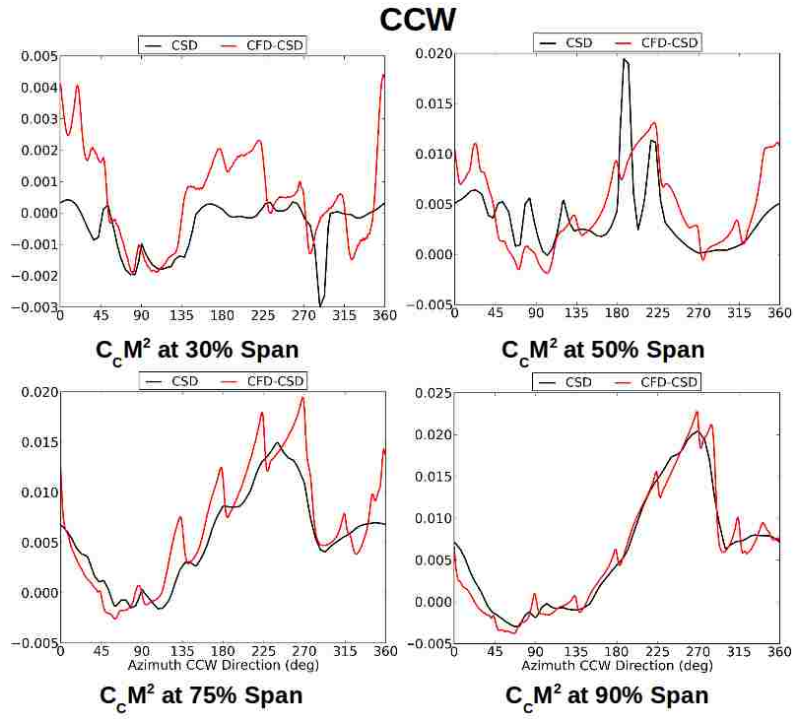


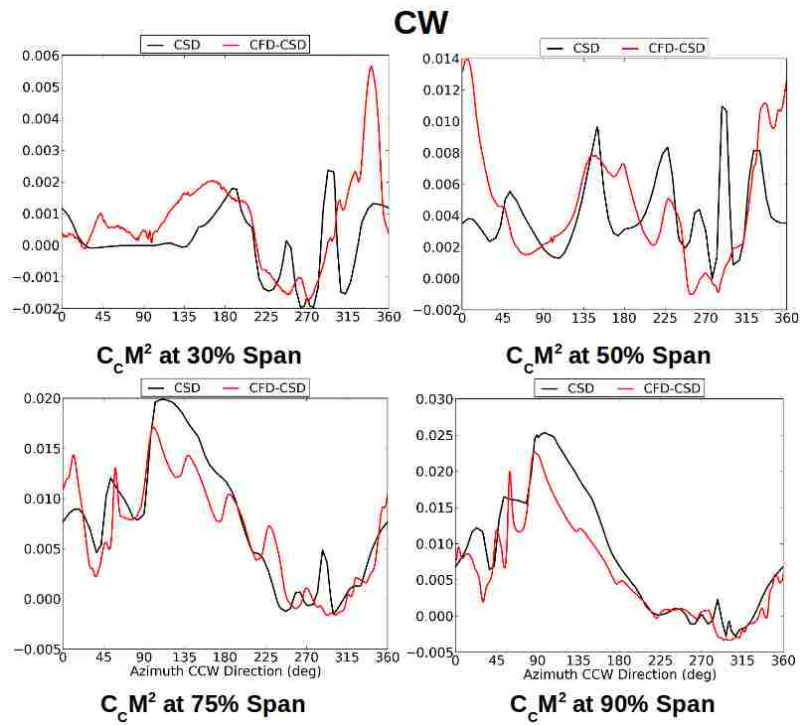
Figure 4.18: Contour plots of  $C_m M^2$  for initial CSD and final CFD-CSD at 100 knots

Line plot comparisons of unsteady airloads at 100 knots mirror the same general trends found at the 55 knots flight condition. At 100 knots there is a small reverse flow region beginning to form on the retreating sides, not seen at 55 knots. This is most prevalent in the pitching moments. At the 30% span location, it is apparent that CSD with free wake predicts a dynamic stall event on the upper rotor (CCW) retreating side that the CFD solution smooths out and predicts it does not occur. As previously seen at 55 knots, the higher harmonic content corresponding to blade passage events is totally missed by the free wake model and this will be the

case for all three flight regimes evaluated.

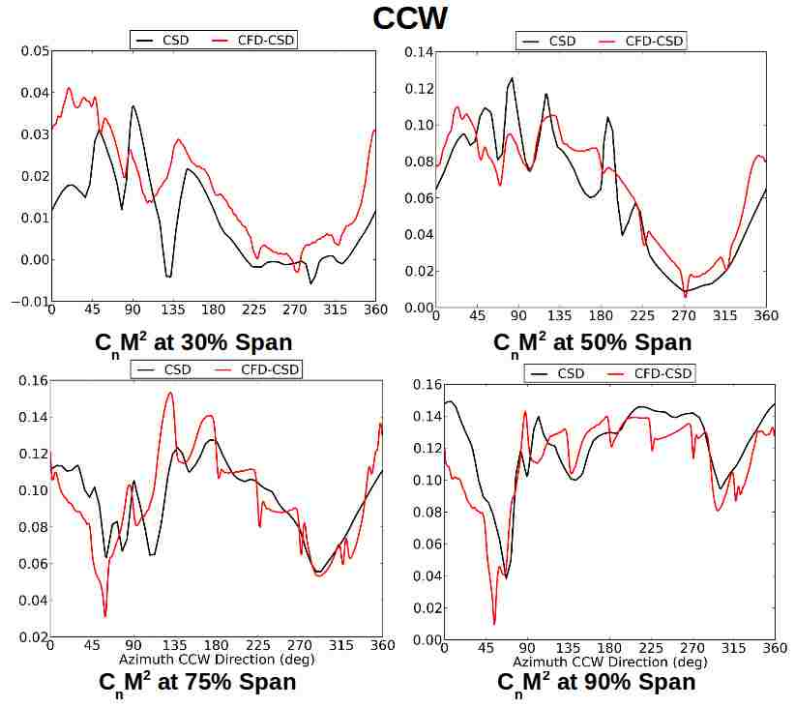


(a) Upper Rotor

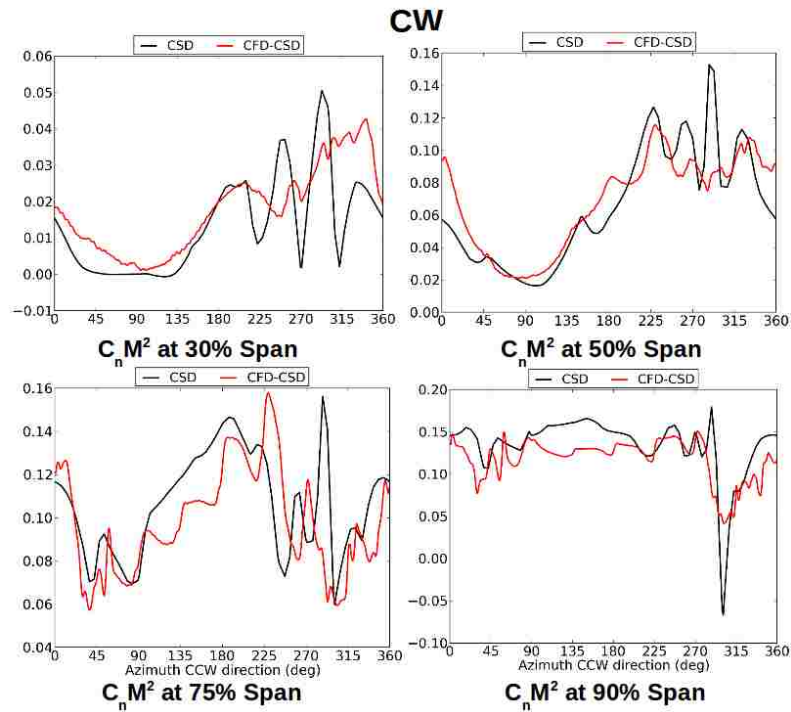


(b) Lower Rotor

Figure 4.19: Line plots of  $C_c M^2$  between initial CSD and final CFD-CSD at 100 knots



(a) Upper Rotor



(b) Lower Rotor

Figure 4.20: Line plots of  $C_n M^2$  between initial CSD and final CFD-CSD at 100 knots

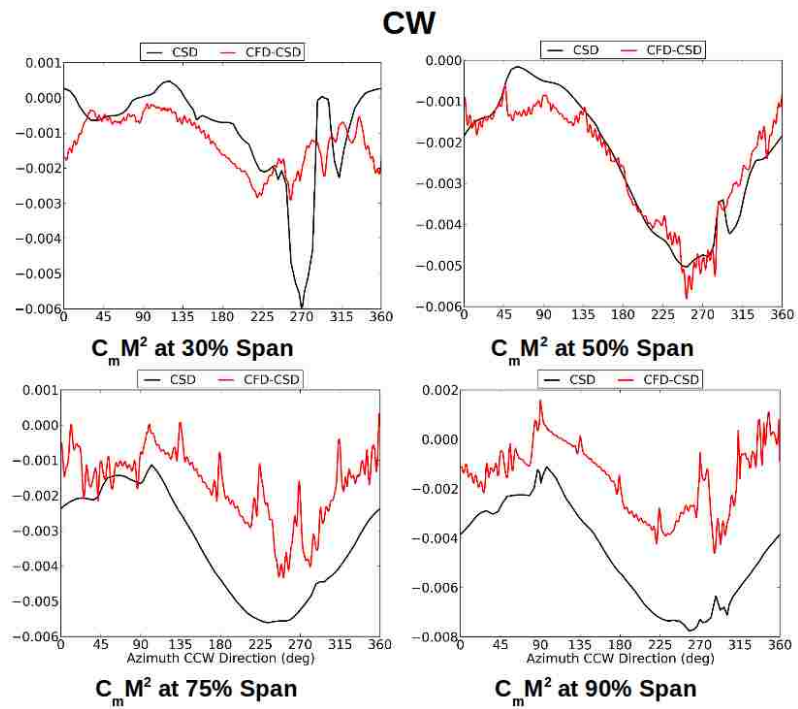
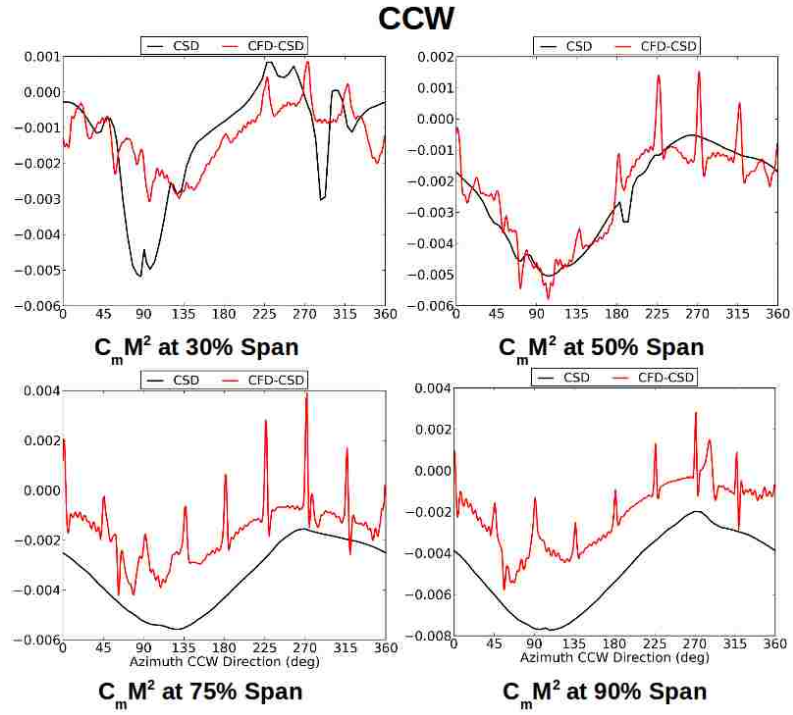


Figure 4.21: Line plots of  $C_m M^2$  between initial CSD and final CFD-CSD at 100 knots



#### 4.4 150 Knots

The third coupled forward flight simulation performed was at 150 knots where the advance ratio is 0.408. At this flight speed, the propeller is now a dominant factor in the vehicle trim process and slight changes in its propulsive thrust value has a large impact on the rotor controls and integrated forces. This flight condition is also the least correlated to test data of the three flight speeds. The total predicted rotor power difference between the baseline analysis and CFD-CSD increases 2.5 times from 48.6 hp to 122.5 hp. The high sensitivity to propeller thrust is most likely the cause for this discrepancy and for these cases remained constant during CFD-CSD coupling iterations.

<b>150 Knots</b>	<b>CSD</b>	<b>CFD-CSD</b>
<b>Collective (deg)</b>	4.29( CCW)	5.95 (CCW)
	5.21 (CW)	6.08 (CW)
<b>Cyclic <math>\theta_{1C}</math> (deg)</b>	1.65 (CCW)	0.28 (CCW)
	1.65 (CW)	0.28 (CW)
<b>Cyclic <math>\theta_{1S}</math> (deg)</b>	-4.87 (CCW)	-5.90 (CCW)
	5.98 (CW)	5.93 (CW)
<b>Fuselage Pitch (deg)</b>	2.43	2.10
<b>Total Thrust (lbs)</b>	5340.1	5020.4
<b>Total Power (hp)</b>	48.6	122.5

Table 4.3: Comparison Between Initial CSD And CFD-CSD Trim Solutions At 150 Knots

The fuselage pitch attitude decreases from an initial value of 2.4 degrees to 2.10 degrees. Like the 55 and 150 knots cases, at 150 knots, the rotor collective pitch for both upper and lower rotors becomes nearly identical after the CFD-CSD coupling and a reduction in  $\theta_{1C}$  is also observed. The total rotor thrust only differs by around 300 lbs between initial CSD and final CFD-CSD coupled solution.

### CFD-CSD Convergence

Figure 4.22 shows rotors controls, collective and cyclics, vs. coupling iteration. Similar to the previous flight conditions, there is a relatively smooth transition from initial to final control values.

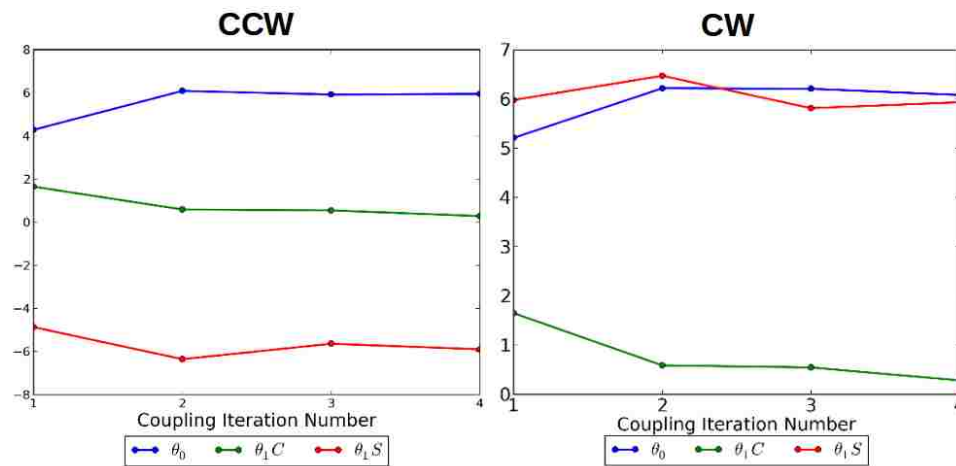
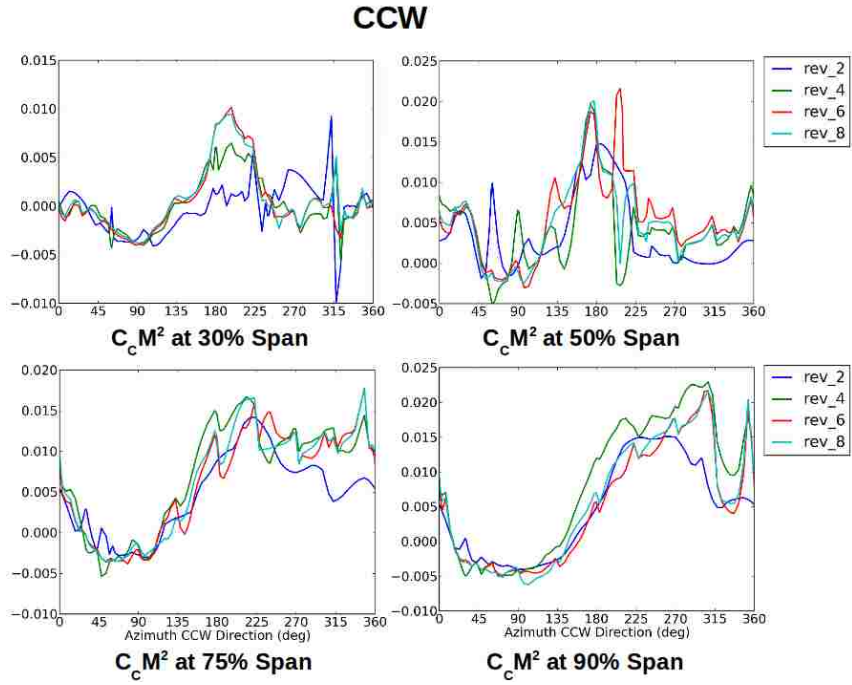
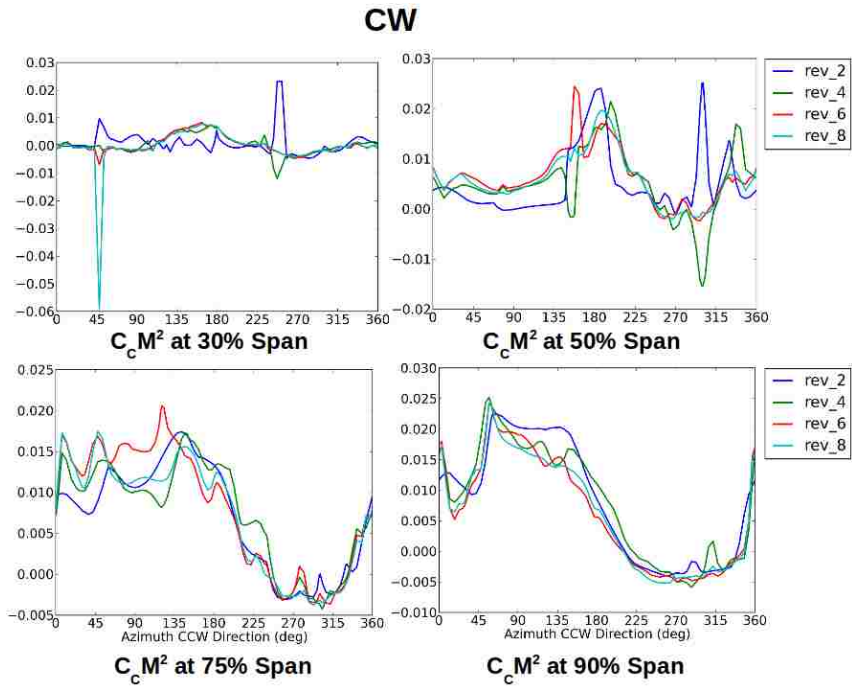


Figure 4.22: Convergence Of Rotor Controls (deg) With CFD-CSD Iterations At 100 Knots

Figures 4.23, 4.24, and 4.25 illustrate deformed frame aerodynamic force and pitching moment time history convergence at 150 knots.

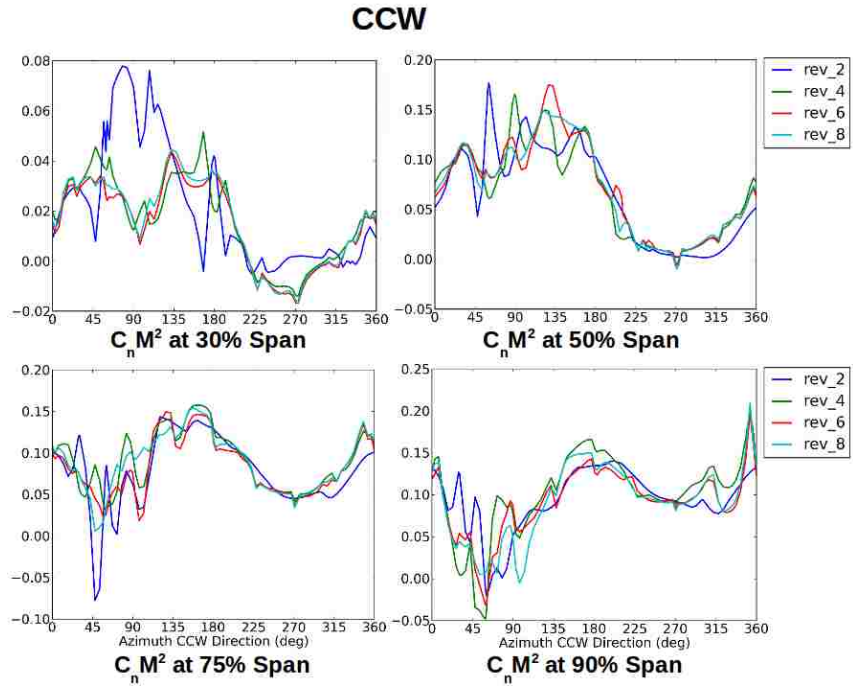


(a) Upper Rotor

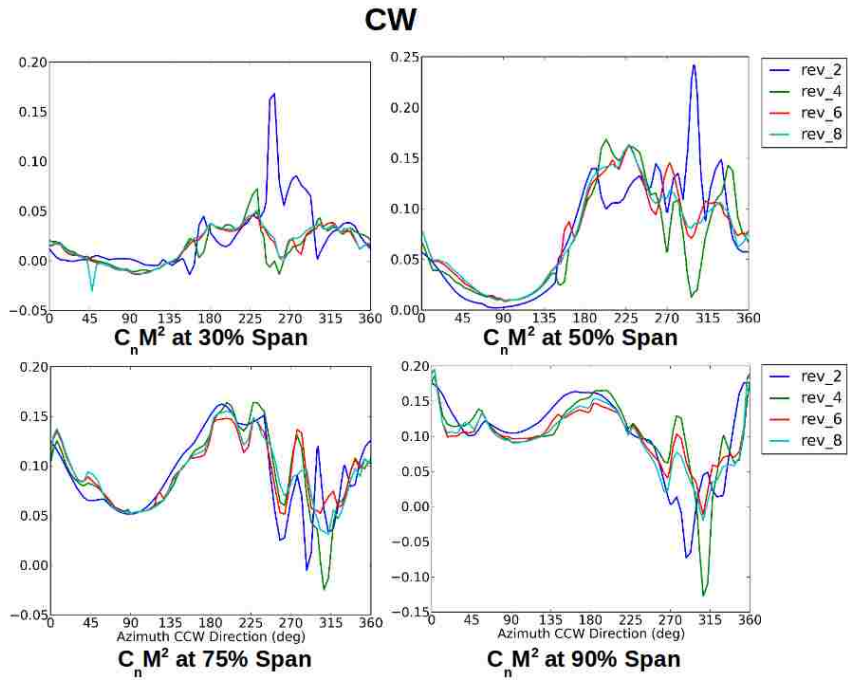


(b) Lower Rotor

Figure 4.23: Convergence of  $C_c M^2$  at 150 Knots

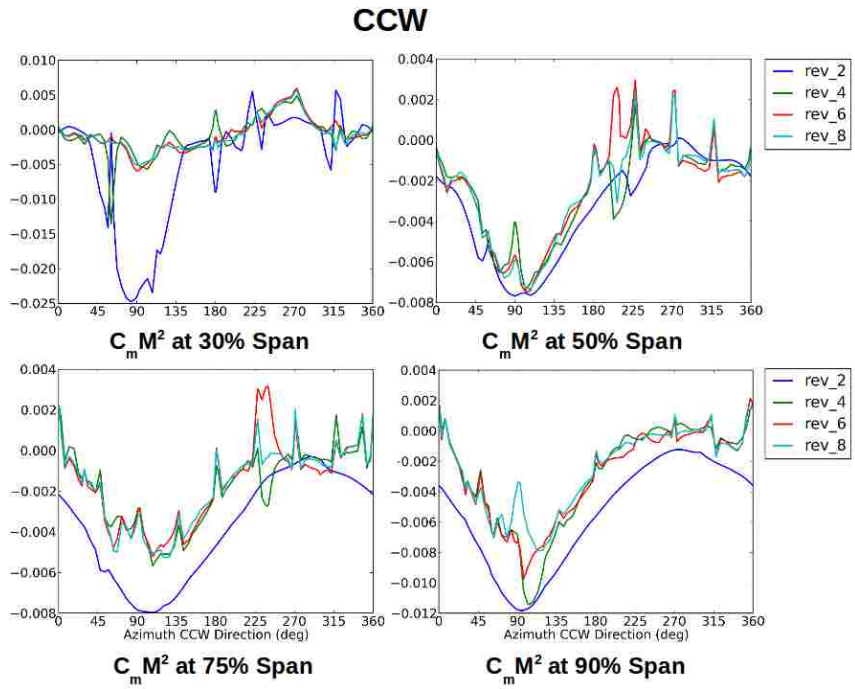


(a) Upper Rotor

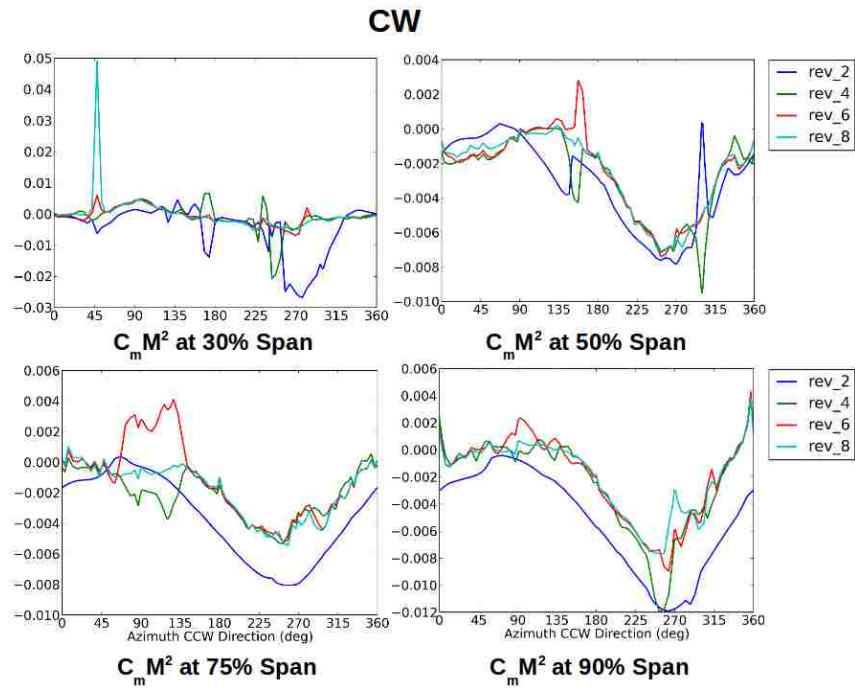


(b) Lower Rotor

Figure 4.24: Convergence of  $C_n M^2$  at 150 Knots



(a) Upper Rotor



(b) Lower Rotor

Figure 4.25: Convergence of  $C_m M^2$  at 150 Knots

## Initial CSD vs Final CFD-CSD Rotor Aerodynamic Loads

150 knots is approaching the limiting speed envelope for conventional single main rotor helicopters. At this speed, the reverse flow region is clearly defined as a circle on the retreating sides. The target lift offset is 0.11 at this flight speed; this is now beginning to offload the retreating sides of the blades. The inability of reduced order models to properly capture viscous blade-wake interactions causes a disagreement between the initial CSD with free wake and the CFD-CSD solution in the retreating flow region. Outside of this region, there is good agreement between the free wake/tables and CFD-CSD for blade airloads. The contour plots from Figures 4.26, 4.27, and 4.28 highlight the key refinements CFD brings. The CFD captures the impulsive normal force and pitching moment on the advancing side of the upper rotor (also seen by CFD at lower flight speeds) and has greater resolution of the pitching moments in the reverse flow bubble. CFD also has a smooth and more realistic resolution of the normal force at the transition points between airfoil sections. This smooth transition was also seen at the lower flight speeds; however, with increases in free stream speed and increase in the relative local angle of attack they are much more pronounced.

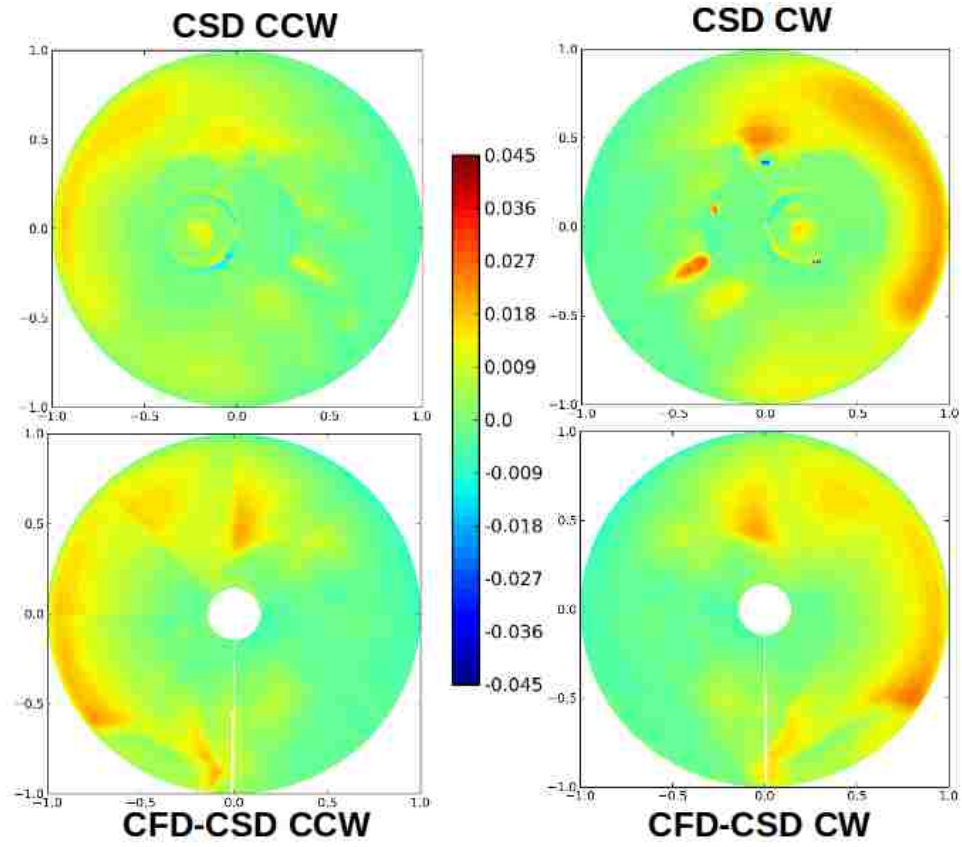


Figure 4.26: Contour plots of  $C_c M^2$  for initial CSD and final CFD-CSD at 150 knots

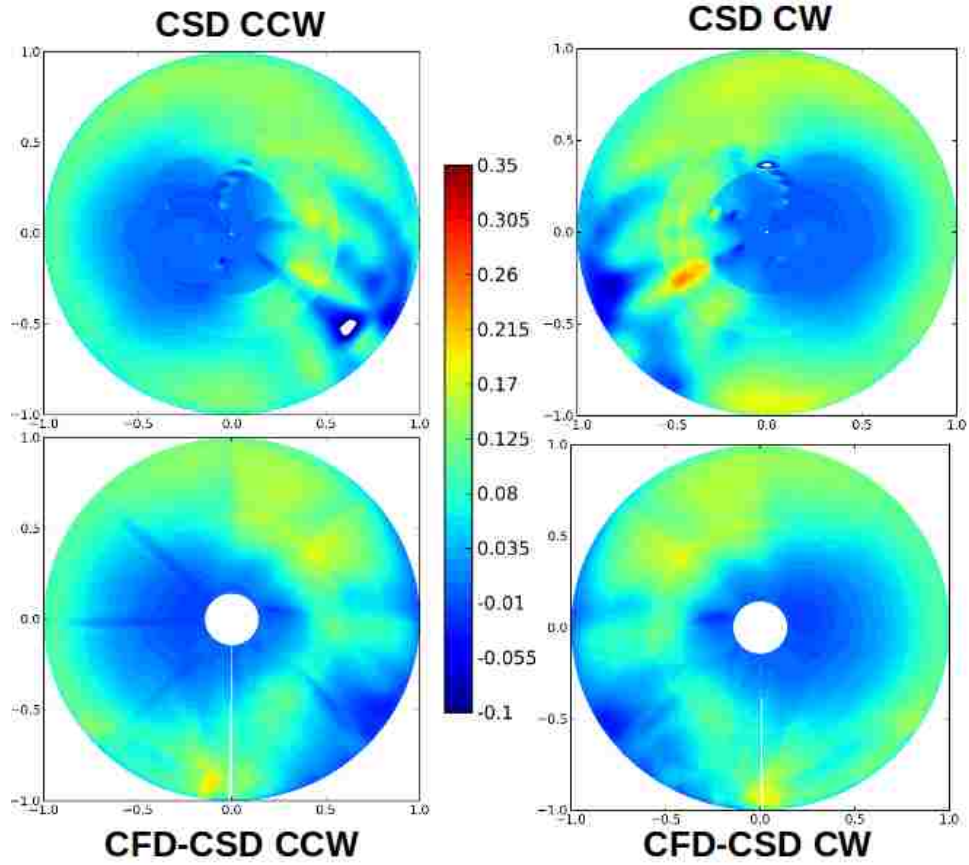


Figure 4.27: Contour plots of  $C_n M^2$  for initial CSD and final CFD-CSD at 150 knots



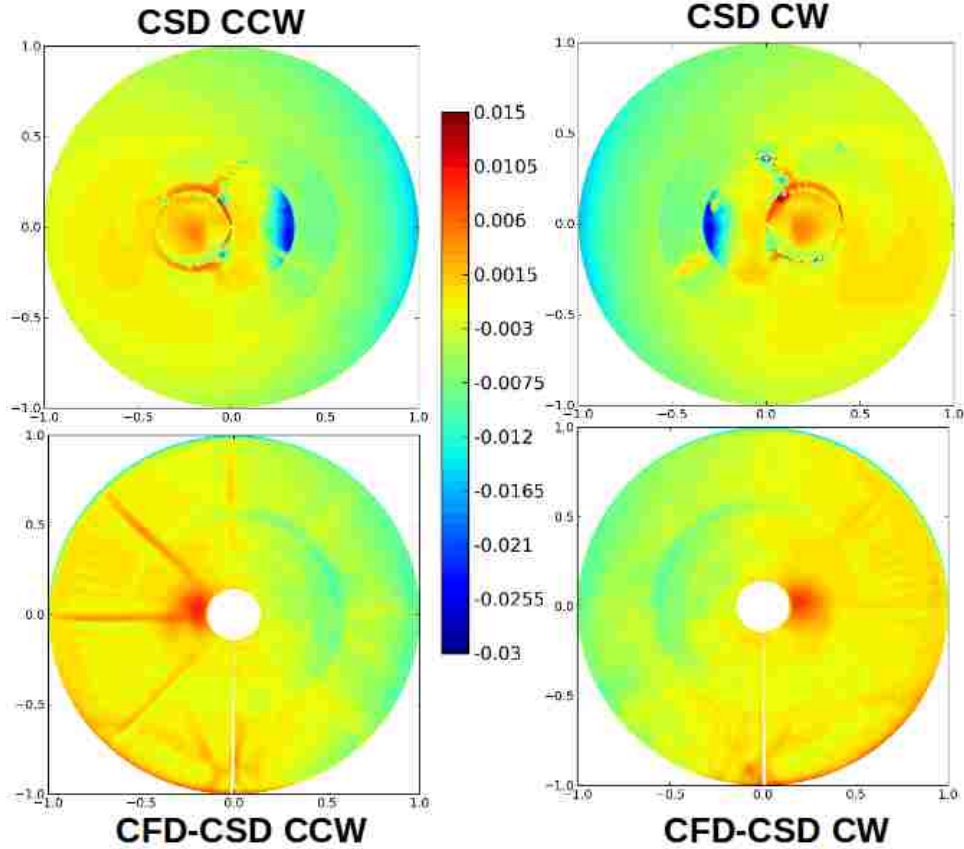


Figure 4.28: Contour plots of  $C_m M^2$  for initial CSD and final CFD-CSD at 150 knots

Line plot comparisons of unsteady time histories of forces and moments at various span-wise stations at 150 knots can be seen in Figures 4.29, 4.30, and 4.31. The time varying angles of attack and flow velocity at  $\mu = 0.41$  set up significant unsteadiness and shed wake elements which undergo viscous interactions with multiple blades. As previously mentioned, the reduced-order models do not natively capture any of this, where as the CFD solution can. This leads to discontinuous pitching moments on the retreating sides and large nose down pitching moments on the advancing sides predicted by CSD with free wake. In contrast, the CFD has

relatively smooth pitching moments.

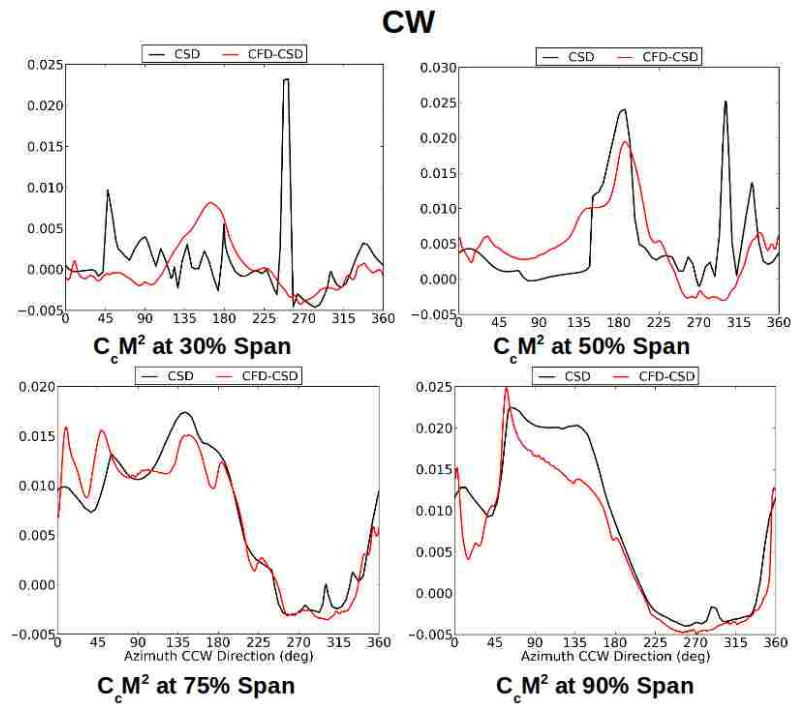
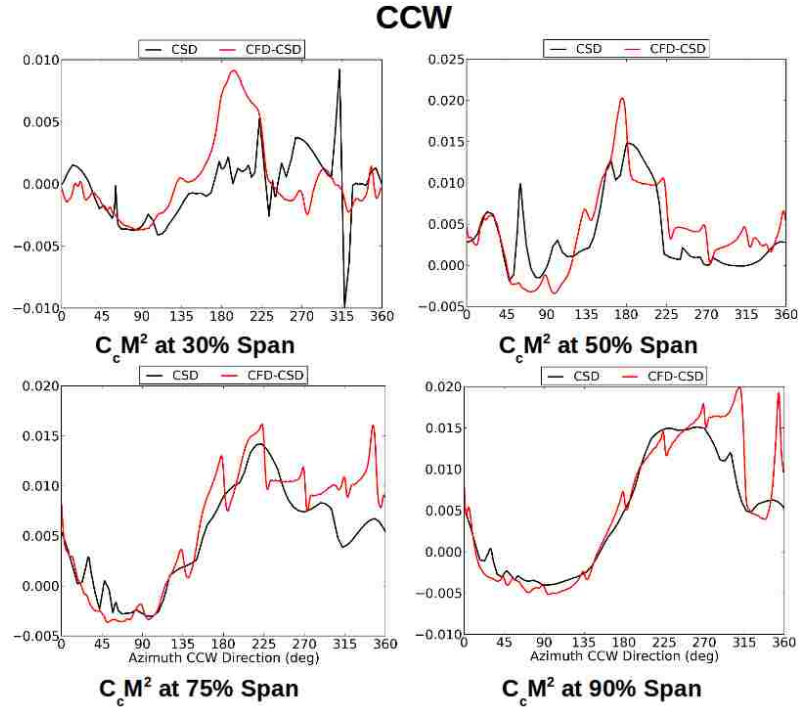


Figure 4.29: Line plots of  $C_c M^2$  between initial CSD and final CFD-CSD at 150 knots

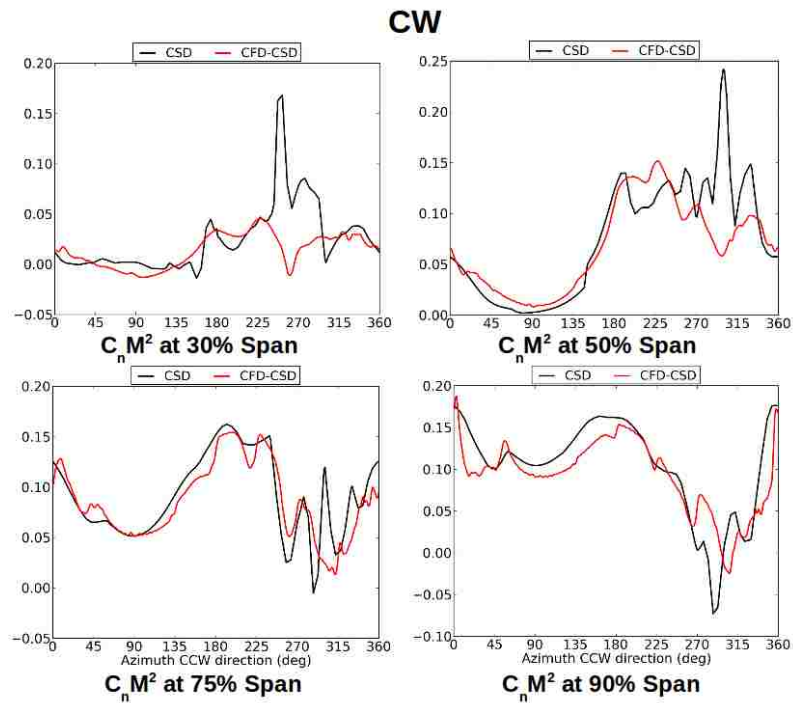
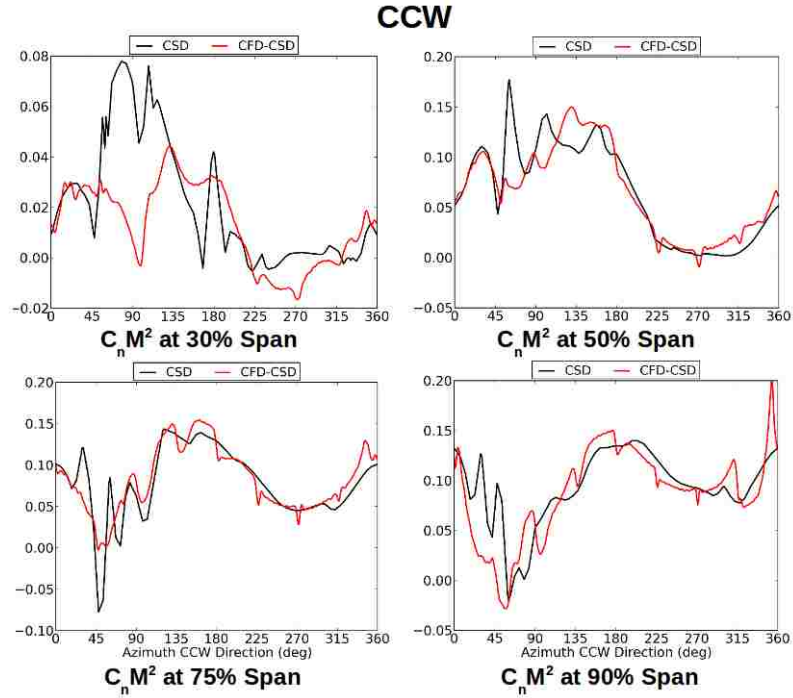


Figure 4.30: Line plots of  $C_n M^2$  between initial CSD and final CFD-CSD at 150 knots

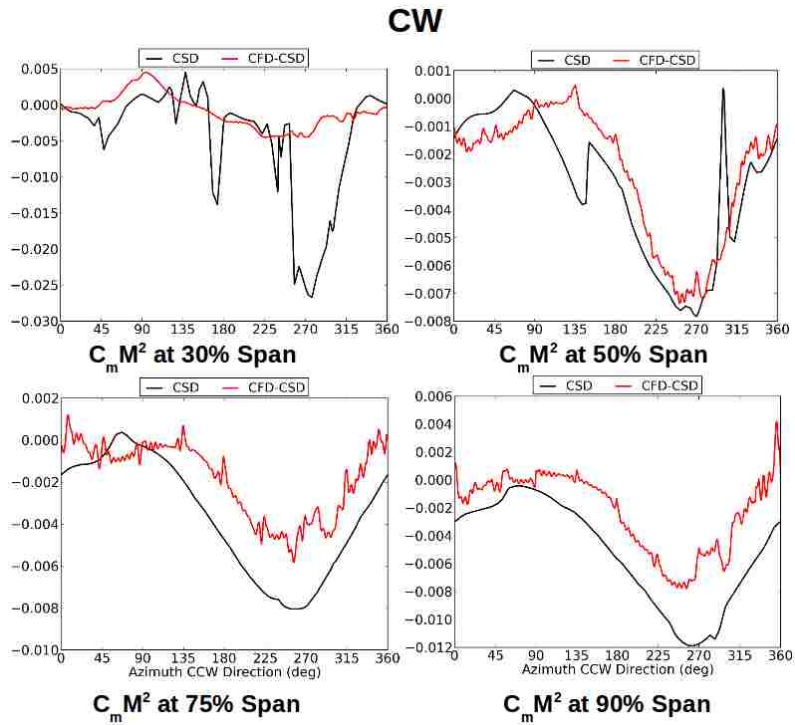
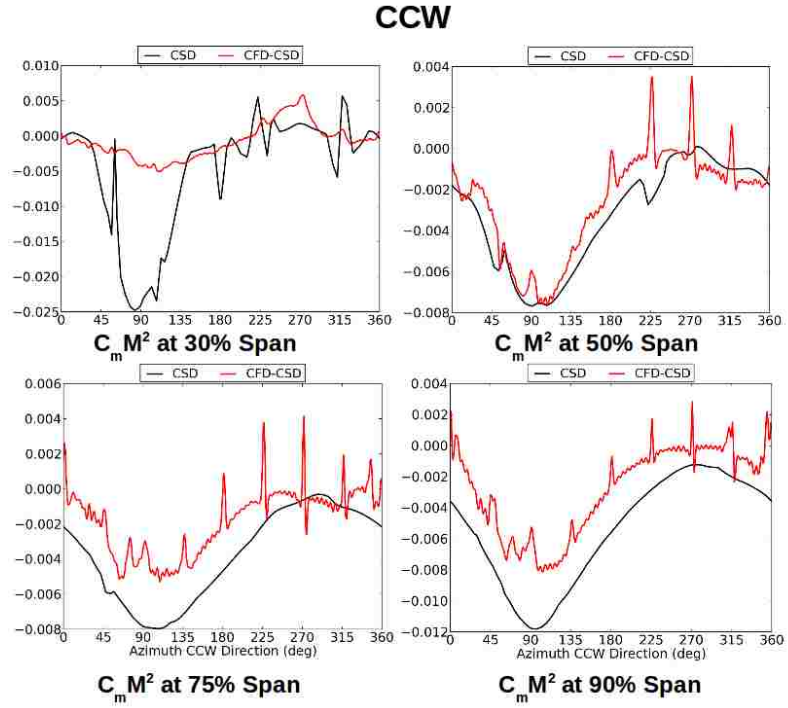


Figure 4.31: Line plots of  $C_m M^2$  between initial CSD and final CFD-CSD at 150

knots

## 4.5 Airspeed Trends

The following results are obtained directly from CFD at the end of the last CFD-CSD convergence cycle. Azimuthal variations of the converged deformed-frame normal force at 30%, 50%, 75% and 85% span are shown in Fig. 4.32 for the counter-clockwise (upper) rotor, and in Fig. 4.33 for the clockwise (lower) rotor. At all three forward flight speeds, an 8/rev signal is apparent in both the normal force and pitching moment on both rotors. Not shown, but observed, is a similar signal in the chordwise force as well. This high-frequency excitation is the direct outcome of interaction between blades of the upper and lower rotor as they cross each other (and their rolled-up wakes) every 45 degrees. The effect of this interaction is stronger on the upper rotor normal force outboard of 75% span on the retreating side, while the impulse is less pronounced on corresponding locations of the lower rotor.

The corresponding pitching moments for the counter-clockwise (upper) rotor are shown in Fig. 4.34, and in Fig. 4.35 for the clockwise (lower) rotor. The impulsive aerodynamic pitching moment due to blade passage is not captured by the simplified aerodynamic model, and the effects are stronger on the upper rotor outboard of 75% span. At the inboard locations, these interactions are less pronounced on both rotors.

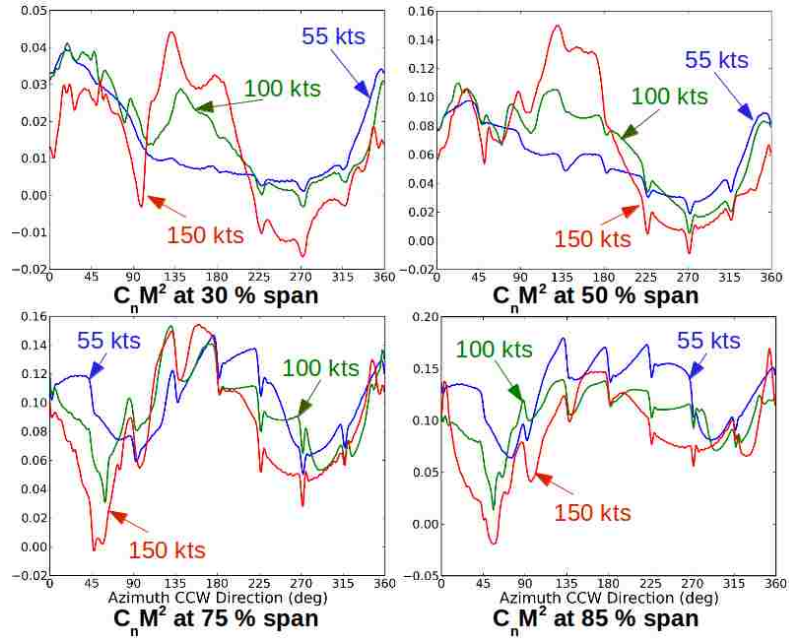


Figure 4.32:  $C_n M^2$  for upper rotor (CCW) at advance ratios of  $\mu = 0.15, 0.27,$  and  $0.41$

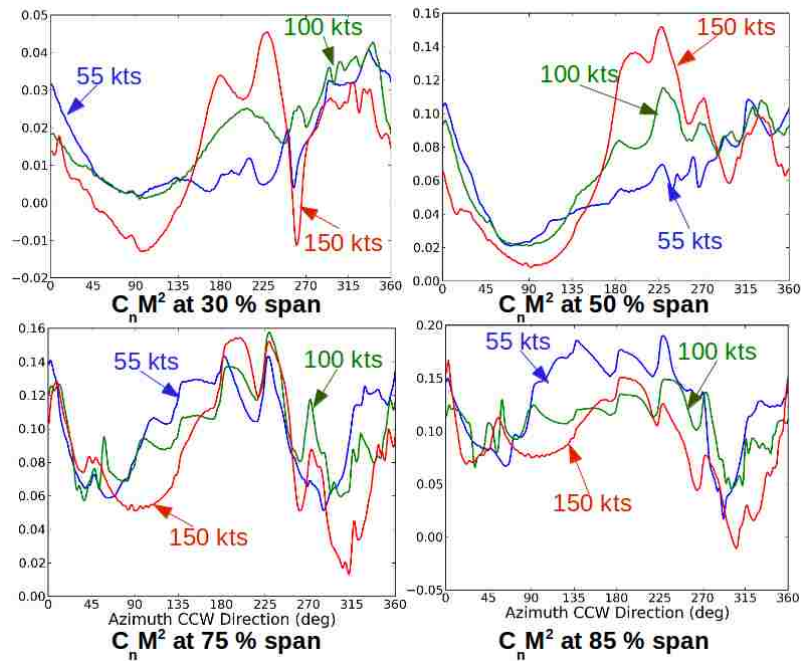


Figure 4.33:  $C_n M^2$  for lower rotor (CW) at advance ratios of  $\mu = 0.15, 0.27,$  and  $0.41$

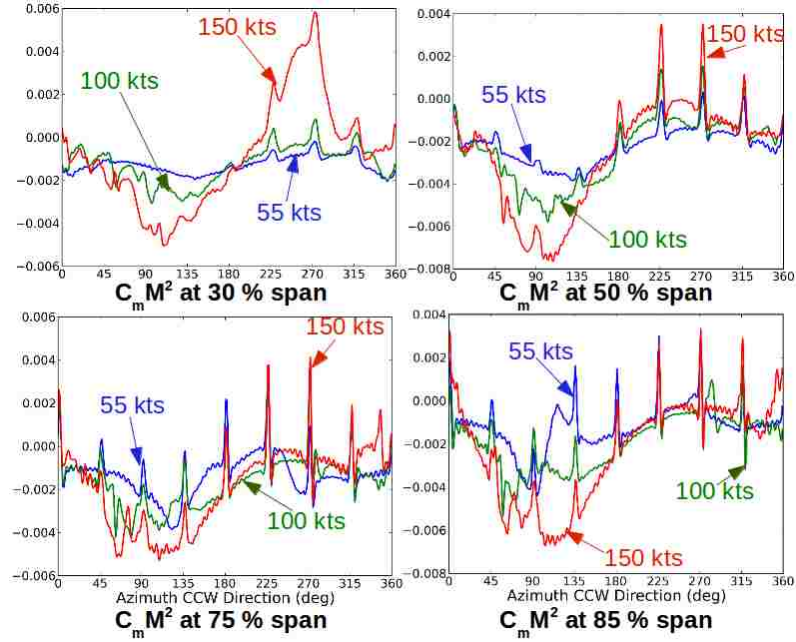


Figure 4.34:  $C_m M^2$  for upper rotor (CCW) at advance ratios of  $\mu = 0.15, 0.27,$  and  $0.41$

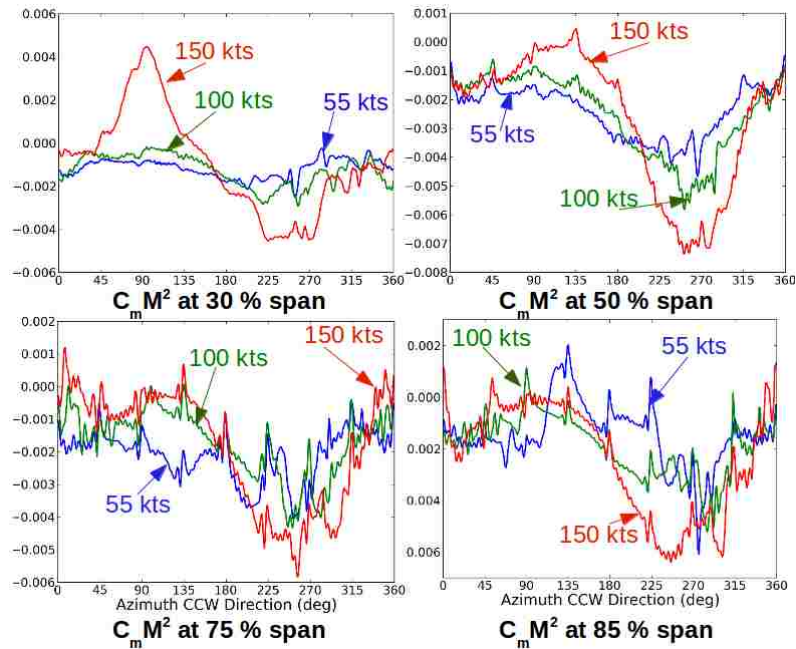


Figure 4.35:  $C_m M^2$  for lower rotor (CW) for advance ratios  $\mu = 0.15, 0.27,$  and  $0.41$



Another global trend was noted for the three flight speeds investigated. Most of the aerodynamic thrust was generated over the front of the rotor disk, and the lift is slightly biased towards the advancing side. The lateral bias is a direct outcome of trimming to a prescribed lateral lift offset for both rotors. As the forward flight speed increases, the propulsive trim solutions (without lift offset regulation) naturally produce lift offsets of the order of the advance ratio [27]. To regulate the blade flap bending moments and minimize chances of structural failure, the trim targets are set to smaller lift offset values. A direct consequence of these trim settings is that the blade pitch angle is set to increasingly nose-down values on the advancing side (negative  $\Delta\theta_{1c}$ ) producing negative lift at the outboard stations, as shown in Figs. 4.32 and 4.33.

As forward speed increases, the propeller thrust increases and the vehicle trims to a nose-up pitch attitude, resulting in a net upwash over the nose and larger effective angles of attack and increased thrust. Over the tail ( $\psi=180$  deg), interplay between this upwash and the effects of rotor wake from the blade over the nose result in a non-uniform trend, especially for the lower rotor. Finally, the impulsive pitching moment increases in strength with increasing forward speed on the retreating side of the upper (CCW) rotor.

## 4.6 Rotor-Rotor Interference: Single vs Coaxial

The blade motions from the final CFD-CSD forward flight coaxial run was applied to CFD as prescribed deflections for two independent single-rotor CFD

simulations. This study directly removes the rotor-rotor interference effects while preserving blade motions, controls, and free stream conditions. This was done for both the upper and lower rotor at two different flight speeds, 55 knots and 150 knots.

## 55 Knots

At 55 knots, the coaxial configuration experiences a reduction in airloads over the rear of the disk compared to the isolated rotors as shown in Figures 4.36, 4.37, and 4.38. The reduction in the normal force indicates increased induced inflow due to rotor-rotor interference. The pitching moments do not show as much affect due to the change in inflow since they are not as sensitive to effective angle of attack. The single rotor result does not exhibit the impulsive 8/rev content, a signature of blade passage.

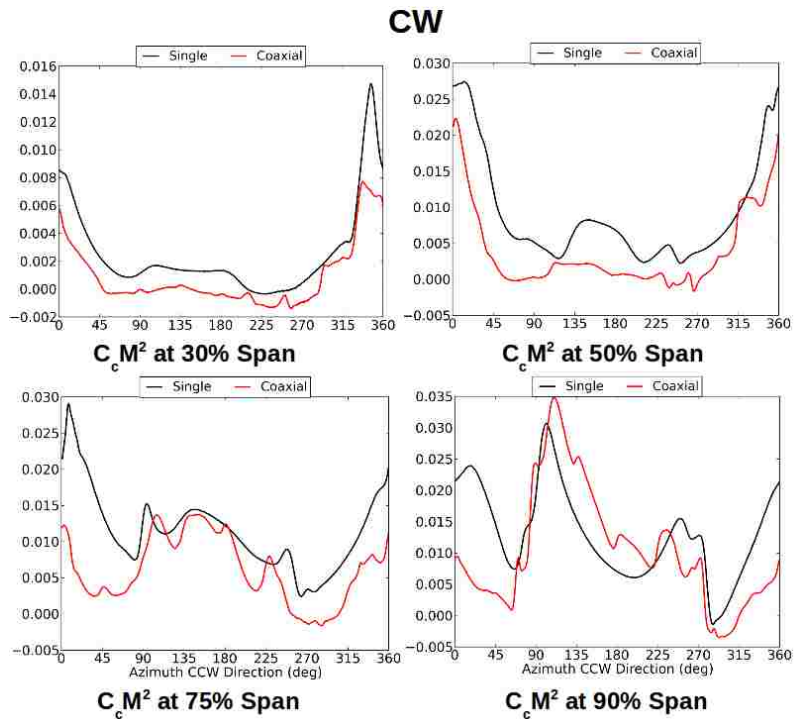
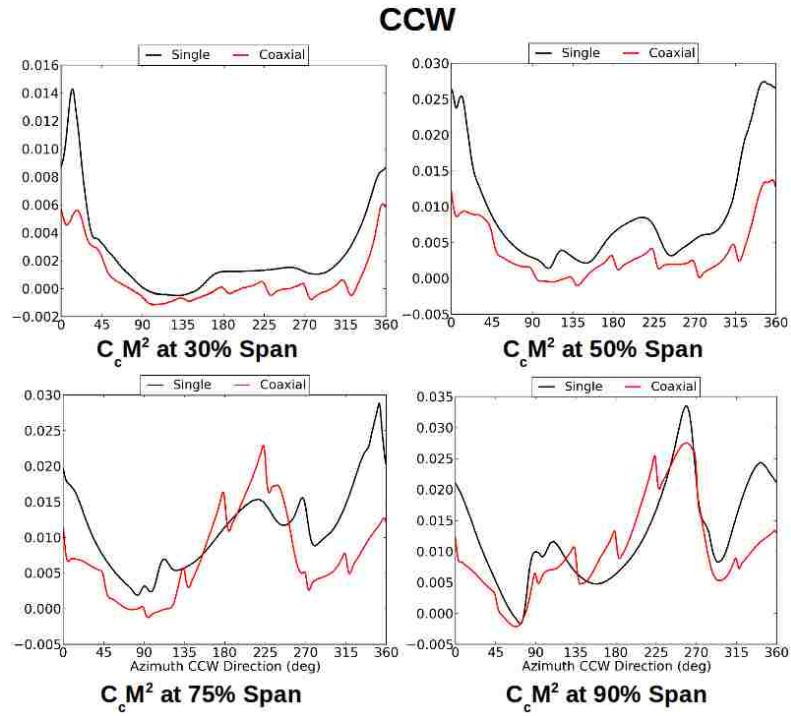
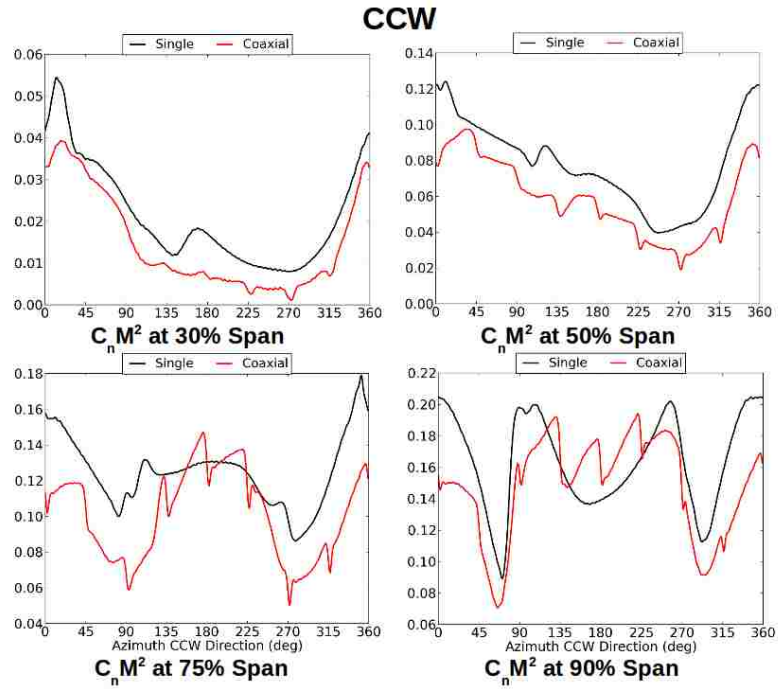
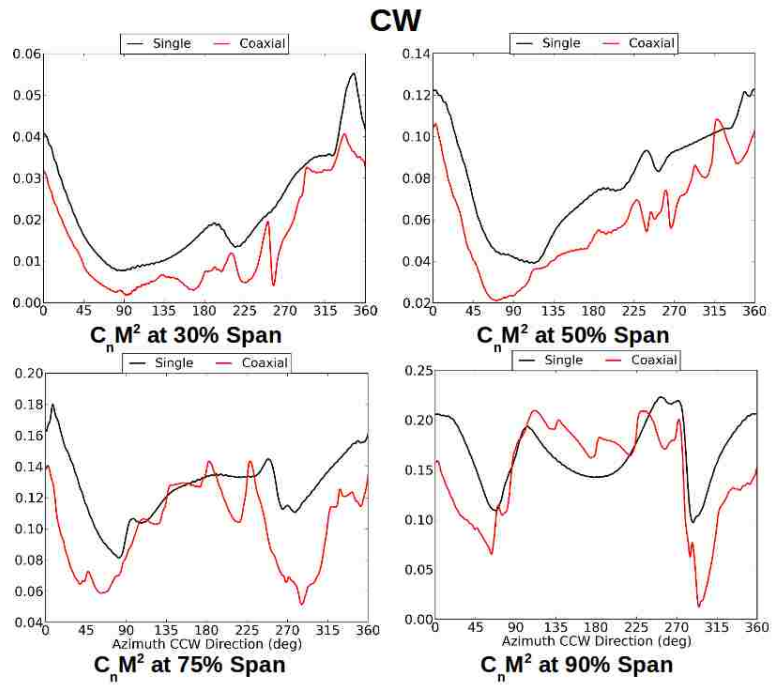


Figure 4.36: Isolated rotors vs. coaxial: comparison of  $C_c M^2$  at 55 knots



(a) Upper Rotor



(b) Lower Rotor

Figure 4.37: Isolated rotors vs. coaxial: comparison of  $C_n M^2$  at 55 knots

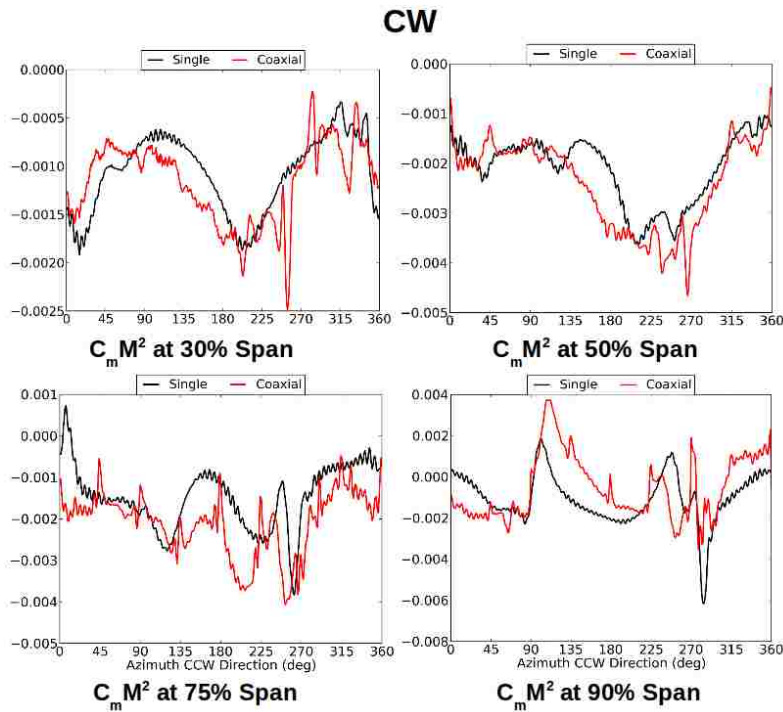
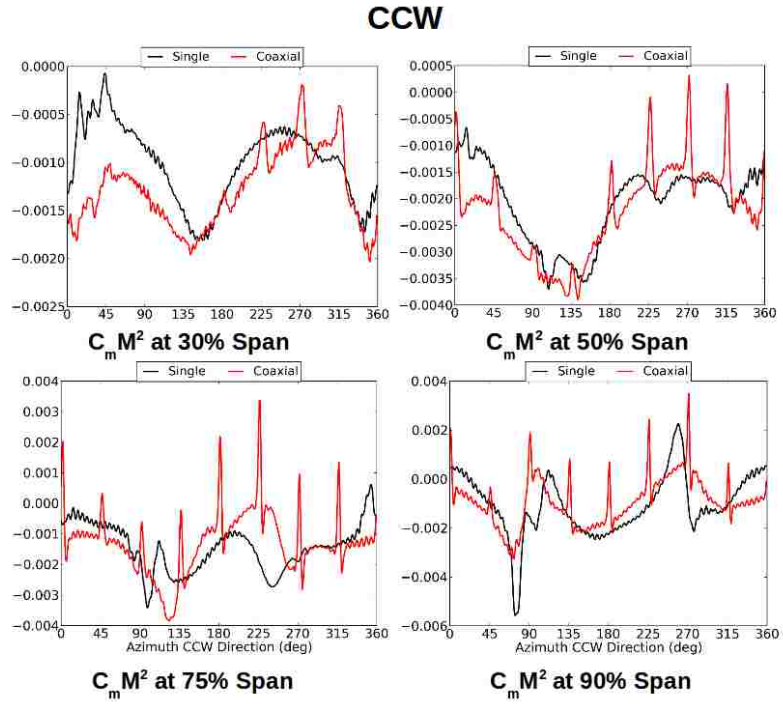
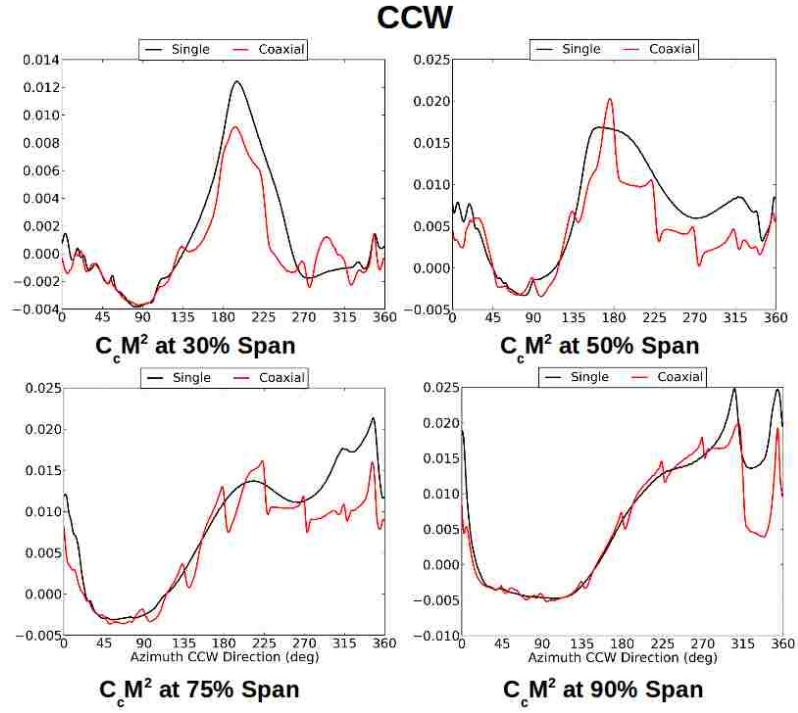


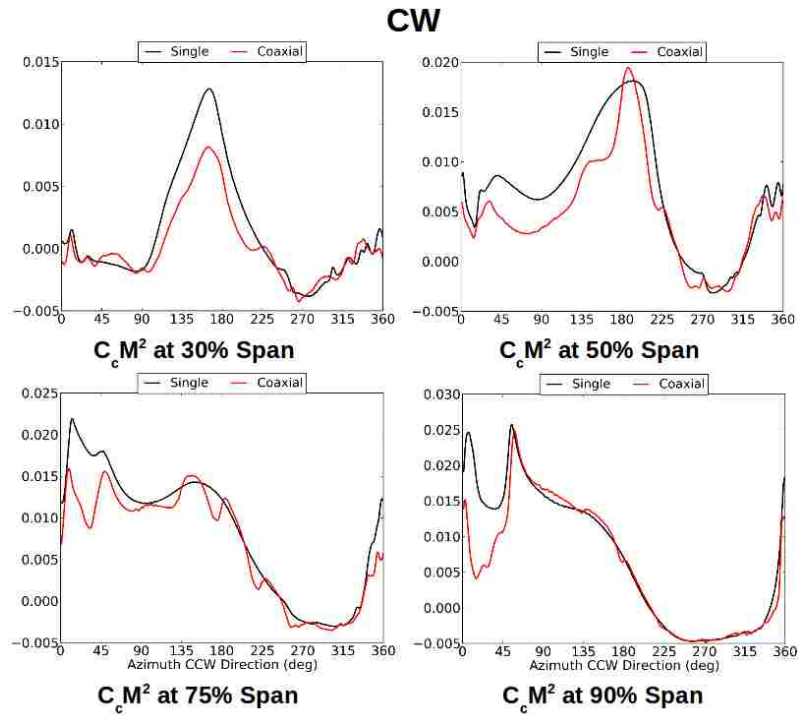
Figure 4.38: Isolated rotors vs. coaxial: comparison of  $C_m M^2$  at 55 knots

## 150 Knots

At 150 knots, rotor-rotor interference is significantly reduced, as shown in Figures 4.39, 4.40, and 4.41. While the isolated rotor no longer contains the 8/rev content, the low-frequency (steady and up to 3/rev) airloads are essentially identical between coaxial vs. isolated configurations.

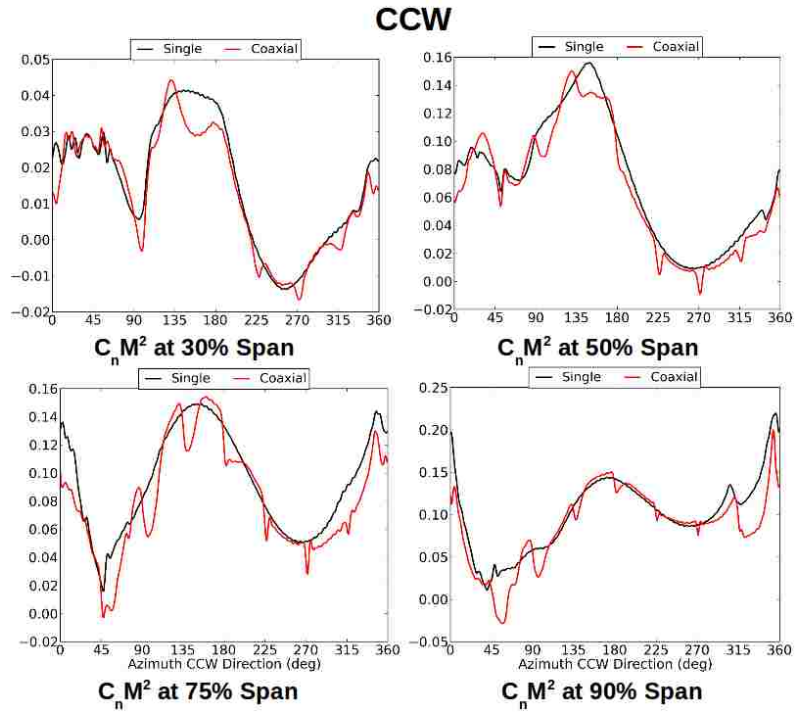


(a) Upper Rotor

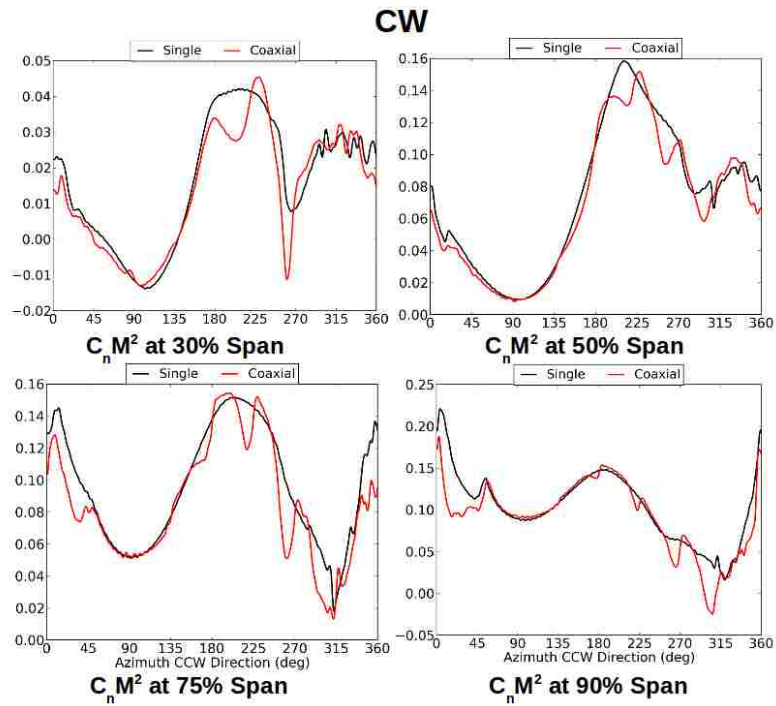


(b) Lower Rotor

Figure 4.39: Isolated rotors vs. coaxial: comparison of  $C_c M^2$  at 150 knots



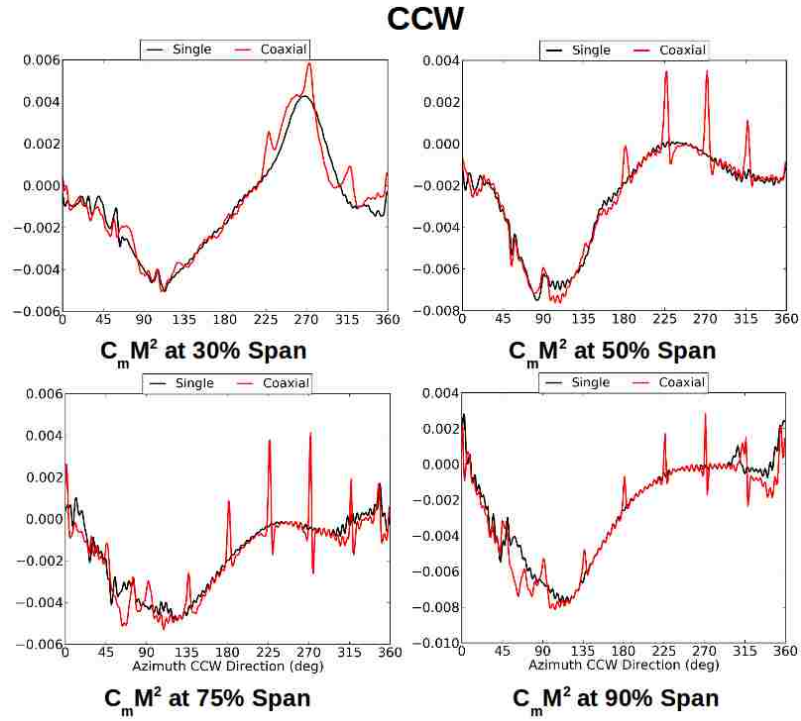
(a) Upper Rotor



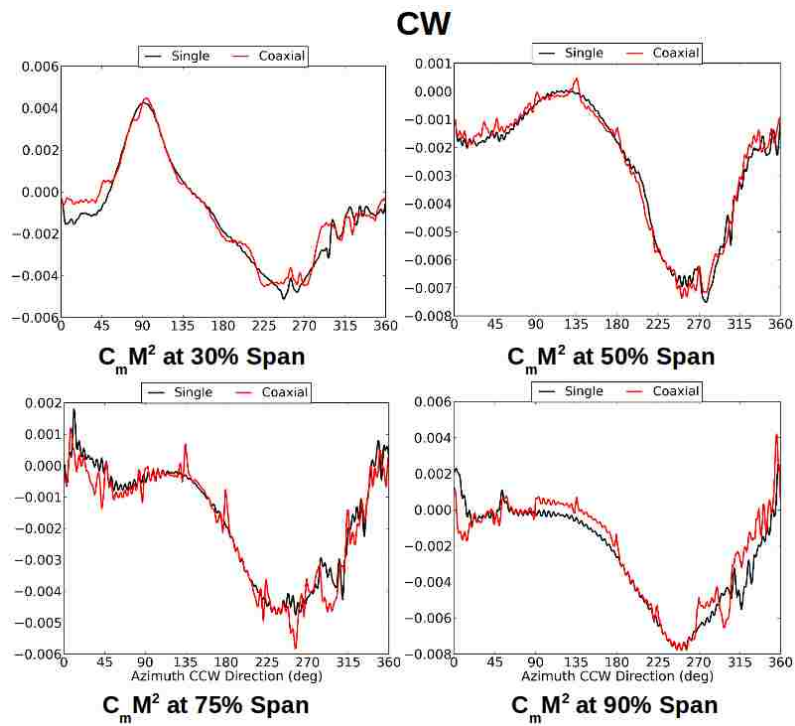
(b) Lower Rotor

Figure 4.40: Isolated rotors vs. coaxial: comparison of  $C_n M^2$  at 150 knots





(a) Upper Rotor



(b) Lower Rotor

Figure 4.41: Isolated rotors vs. coaxial: comparison of  $C_m M^2$  at 150 knots

The reason for reduced interference at higher advance ratios may lie in the wake trajectory. Figure 4.42 shows a contour plot of the vehicle centerline plane colored by vorticity magnitude at 55 knots and 150 knots. At 55 knots, the upper rotor wake structure impinges on the lower rotor. At 150 knots, the rotor wakes are almost parallel to their corresponding tip-path-planes. At sufficiently high advance ratios, rotor-rotor interference may be negligible for flight dynamic considerations, but still plays a role in aeromechanics and vibrations.

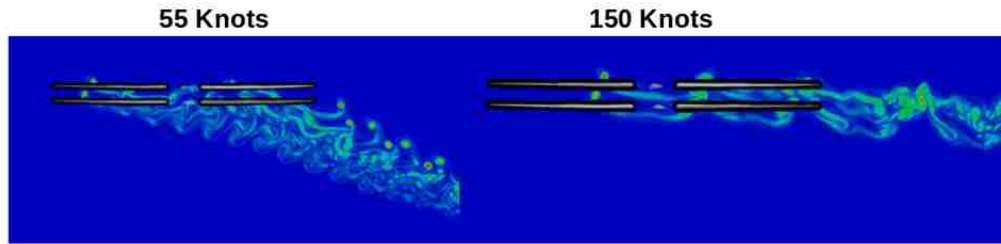


Figure 4.42: Centerline vorticity magnitude and wake structure at  $\mu = 0.15$  (left) and  $\mu = 0.41$  (right)

## 4.7 Hubloads

Lastly, a comparison of the predicted vibratory hub loads between initial CSD and CFD-CSD is shown in Figures 4.43 and 4.44 for all three flight speeds. The 4/rev and 8/rev in-plane hub force ( $\sqrt{F_x^2 + F_y^2}$ ), in-plane hub moment ( $\sqrt{M_x^2 + M_y^2}$ ) and the vertical hub force ( $F_z$ ) were computed for both the upper and lower rotors.

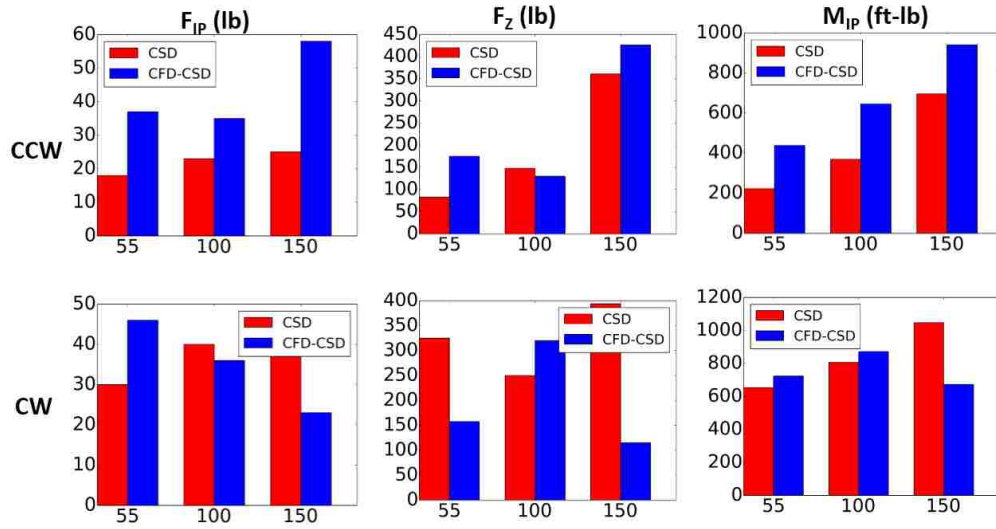


Figure 4.43: Comparison of 4/rev hub loads (lb, ft-lb) : initial CSD vs. CFD-CSD

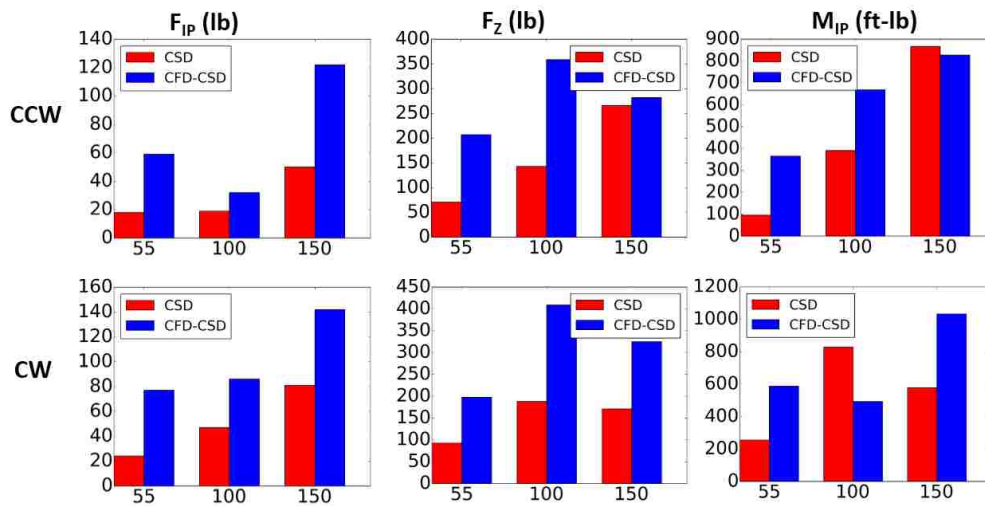


Figure 4.44: Comparison of 8/rev hub loads (lb, ft-lb) : initial CSD vs. CFD-CSD

## Upper Rotor

At all flight speeds investigated, CSD under-predicts both 4P and 8P in-plane shear by almost 50%. The magnitudes of this vibratory force are small, however, in comparison to the vertical shear and in-plane moment. As the speed and advance ratio increase, prediction accuracy from the CSD/free wake model improves for the vibratory in-plane moment. An improvement in CSD predictions is apparent for the upper rotor loads with increasing flight speed. This improvement might stem from reduced inter-rotor interference at higher advance ratios.

## Lower Rotor

The 4P in-plane shear shows under-prediction at 55 knots, good correlation at 100 knots and over-prediction at 150 knots. The 4P vertical shear demonstrates over-prediction at 55 knots, good correlation at 100 knots and significant over-prediction (200%) at 150 knots. The in-plane moment shows good correlation at 55 and 100 knots, and 30% over-prediction at 150 knots.

The 8P in-plane and vertical shear are consistently under-predicted by the free wake model in comparison to the CFD-coupled solution. The vibratory in-plane moment is over-predicted at 100 knots and under-predicted at the other speeds, with at least 50% error margin for most cases. The physical origin of this prediction error lies in the unmodeled wake interactions (intersection of vortices with blade boundary layers) that are inherently captured by CFD solvers from a first-principles based approach.

## Chapter 5: Forward Flight Results: Rotor System And Fuselage

### 5.1 Overview

To examine rotor-fuselage interactional aerodynamics three separate fuselage models were overset with the isolated coaxial rotor CFD meshes. The fuselages were modeled with near-body unstructured grids and rotor + fuselage CFD cases retained the same blade and background grids as the isolated coaxial rotor cases. Aside from obtaining the global impact of a fuselage body on the rotor system, it was also desirable to quantify changes in rotor blade aerodynamic loads with increasingly more complex and realistic fuselage models. The simple fuselage case was used to illustrate the global impact of a simple cigar shape fuselage that retains the same shape as the X2 but only includes the main airframe. Then, two more fuselage models, complex fuselage, and complex fuselage with mast were also studied where the lower hub fairing between the fuselage and the lower rotor was modeled along with the empennage behind the rotor, and where the inclusion of a rotor mast between both rotors was also modeled respectively.

All three fuselage designs were run at both 55 Knots and 150 Knots forward flight speed. These cases used both the OVERFLOW and NSU3D near-body CFD solvers for the blades and fuselage grids respectively. These cases took anywhere

from 8 to 13 hours per rotor revolution on the AFRL and ARL HPC clusters using 240 processors per case. The unstructured fuselage grids caused an increase in compute time per rotor revolution compared to the isolated coaxial rotor cases for two reasons. The first being that adding more grid points and keeping the same number of processors will increase runtime and the second being that the fuselage grids are unstructured grids and require more compute time than an equivalent structured grid. At both the 55 Knots and 150 Knots flight conditions, the three fuselage model cases blade airloads were compared to the baseline isolated coaxial rotor system to quantify rotor-fuselage interactional influence on main rotor sectional loads, and integrated metrics.

It must be noted that while the fuselage and empennage geometry were included in the CFD, during CFD-CSD coupling only the rotor airloads were updated to the CSD solver, the empennage and fuselage aerodynamic forces from CFD were not used to update the fuselage or empennage aerodynamic models that are inside the CSD solver during trim. Therefore, these studies solely focus on how having these bodies in the CFD flow domain impact induced velocities at the main rotor disks. The calculation of the fuselage and empennage airloads for coupling back to the CSD solver are left for future work.

## 5.2 55 Knots Comparison

Looking at the wake trajectory of the isolated coaxial rotor 55 and 150 knots forward flight cases it was apparent that at low speeds, the blade vortices have time

to convect downward and will interact and/or be impinged by the presence of a fuselage or rotor mast. This could have an impact on the blade aerodynamic loads. A comparison of the three fuselage models and isolated coaxial rotor system CFD-CSD coupling rotor controls and fuselage attitude at 55 knots is shown in Table 5.1 for comparison to predictions with the three included fuselage models.

<b>55 Knots</b>	<b>Isolated</b>	<b>Simple</b>	<b>Complex</b>	<b>Complex w/ Mast</b>
<b>Collective <math>\theta_0</math> (deg)</b>	9.45 (CCW)	9.28 (CCW)	9.38 (CCW)	9.23 (CCW)
	9.39 (CW)	9.23 (CW)	9.31 (CW)	9.29 (CW)
<b>Cyclic <math>\theta_{1C}</math> (deg)</b>	3.29 (CCW)	3.48 (CCW)	3.40 (CCW)	3.40 (CCW)
	3.29 (CW)	3.48 (CW)	3.40 (CW)	3.40 (CW)
<b>Cyclic <math>\theta_{1S}</math> (deg)</b>	-3.65 (CCW)	-3.57 (CCW)	-3.65 (CCW)	-3.53 (CCW)
	3.16 (CW)	3.13 (CW)	3.01 (CW)	3.23 (CW)
<b>Fuselage Pitch (deg)</b>	-0.44	-0.46	-0.46	-0.40

Table 5.1: Comparison of trim controls between isolated coaxial rotor and rotor + fuselage cases at 55 knots

Comparing the isolated coaxial rotor system to the rotor + fuselage cases, there are distinct changes in rotor controls. The collective of both the upper and lower rotor is slightly decreased for the rotor + fuselage cases. The cyclic  $\theta_{1C}$  for both rotors increases for the fuselage cases compared to the isolated coaxial rotor system, with the simple fuselage case causing the largest increase. The differential cyclic  $\theta_{1S}$  also changes between the isolated coaxial rotor and the rotor + fuselage cases. The pitch attitude of the fuselage remains nearly constant and only varies by

a couple hundredths of a degree.

Looking at the integrated quantities between the three fuselage cases and the isolated coaxial rotor case there is not much difference in thrust or power. In all four cases, the lower rotor produces slightly more thrust than the upper rotor. The deviation in total rotor power and total rotor thrust is less than 1% between all four cases. This means that all three fuselage models exhibit near identical behaviour to that of the isolated coaxial rotor system for integrated quantities and rotor performance metrics. This information is summarized in Table 5.2.

<b>55 Knots</b>	<b>Isolated</b>	<b>Simple</b>	<b>Complex</b>	<b>Complex w/ Mast</b>
<b>Thrust Upper Rotor (lbs)</b>	2944.24	2933.74	2961.84	2917.84
<b>Thrust Lower Rotor (lbs)</b>	2968.95	2970.34	3005.44	2990.64
<b>Total Thrust (lbs)</b>	5913.35	5904.08	5967.28	5908.48
<b>Total Power (hp)</b>	429.9	426.0	431.7	425.9

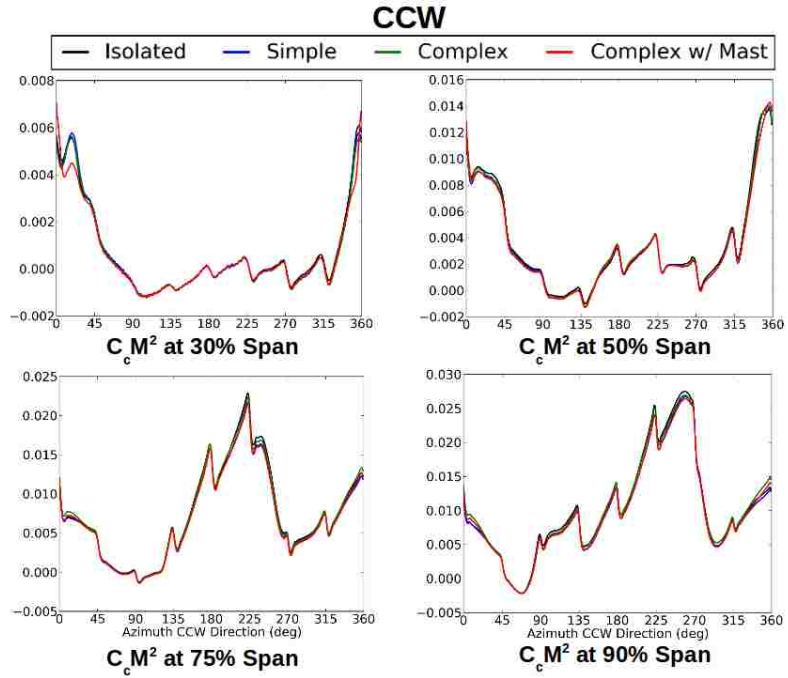
Table 5.2: Comparison of integrated quantities between isolated coaxial rotor and rotor + fuselage cases At 55 knots

Figures, 5.1, 5.2, and 5.3 compare deformed frame time histories of forces and moments ( $C_c M^2$ ,  $C_n M^2$ ,  $C_m M^2$ ) at radial stations of 30, 50, 75, and 90 percent span predicted by the three fuselage cases as well as for the isolated coaxial rotor case for both the upper rotor (CCW) and the lower rotor (CW) at 55 knots. Looking at the chordwise force and normal force, it is apparent that the fuselage models have a slight change in magnitude over the tail (Azimuth: 345-15 deg). The vast majority of the rotor disk for both rotors give nearly identical force magnitudes and phase

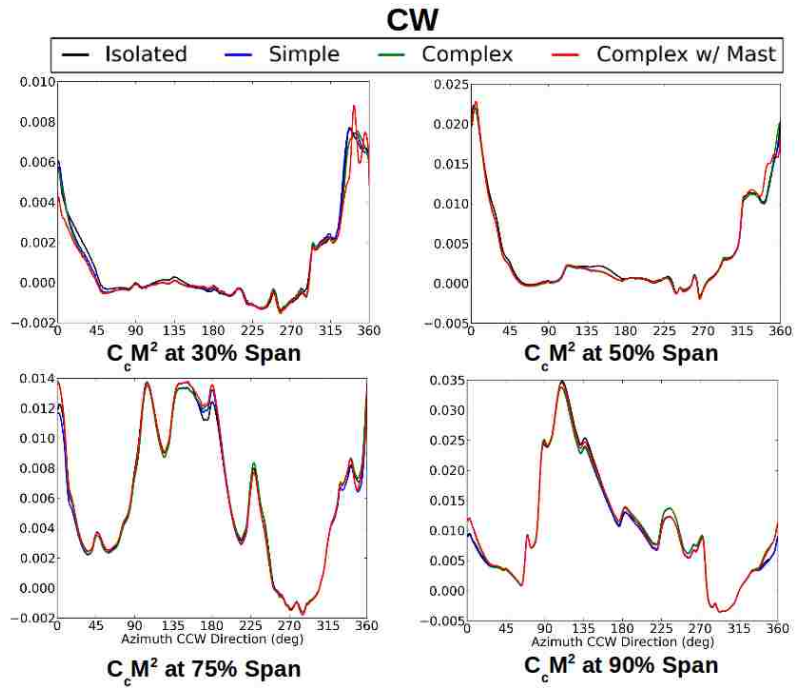


between the rotor + fuselage cases and isolated coaxial rotor case. The interference over the tail is seen most prominently at the inboard stations and is greatest in the fuselage model that contains the rotor mast. The rotor mast also has more of an effect over the tail of the lower rotor disk compared to the upper rotor which is expected.

For deformed frame normal force, both rotors see a slight increase over the nose and regions of the rotor disk in all three fuselage cases. Overall, the three fuselage models exhibit the exact same behaviour relative to each other. Only the complex fuselage with rotor mast seems to slightly deviate at the inboard stations. The pitching moments show much more variation between the fuselage models and the isolated coaxial rotor case compared to the other two forces. Over both rotors and radial stations there is a global trend of slight reduction in nose down pitching moments. The peak to peak magnitude of the  $8 / \text{rev}$  is the same for the rotor + fuselage cases and the isolated coaxial rotor, however in between these impulsive spikes the fuselage cases see a slight reduction. For all three rotor + fuselage cases, the peak to peak magnitude and waveform phase of all the forces remains very close to the isolated coaxial rotor case over the majority of the rotor disks azimuth. Since the integrated quantities had less than 1% variation it was expected that the sectional loads might exhibit the same phenomena.



(a) Upper Rotor



(b) Lower Rotor

Figure 5.1: Line plots of  $C_c M^2$  between isolated coaxial rotor and rotor + fuselage cases at 55 knots

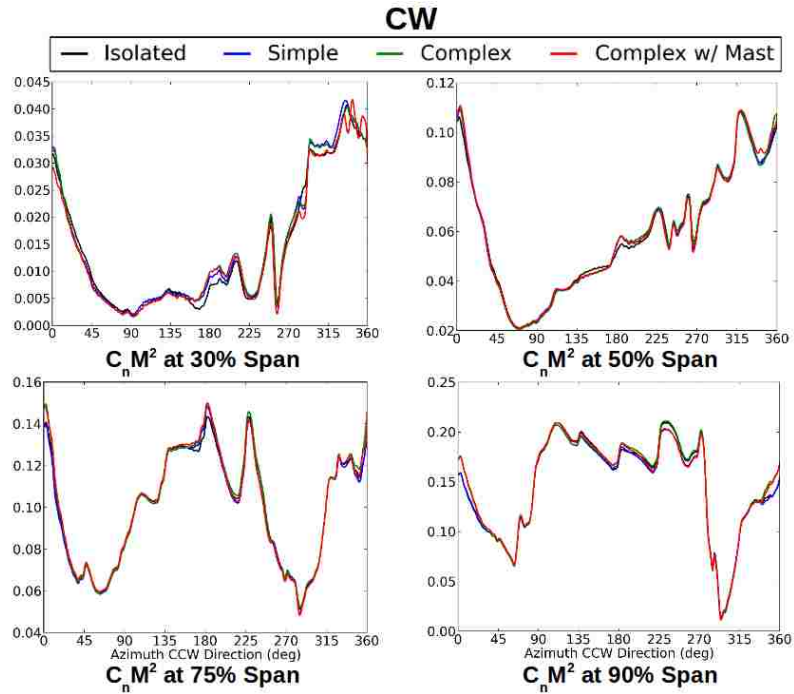
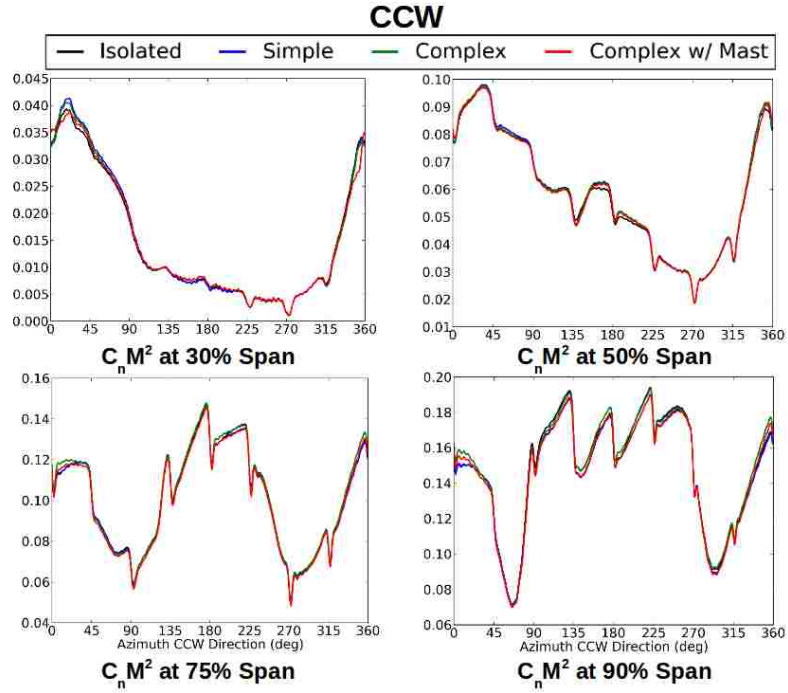
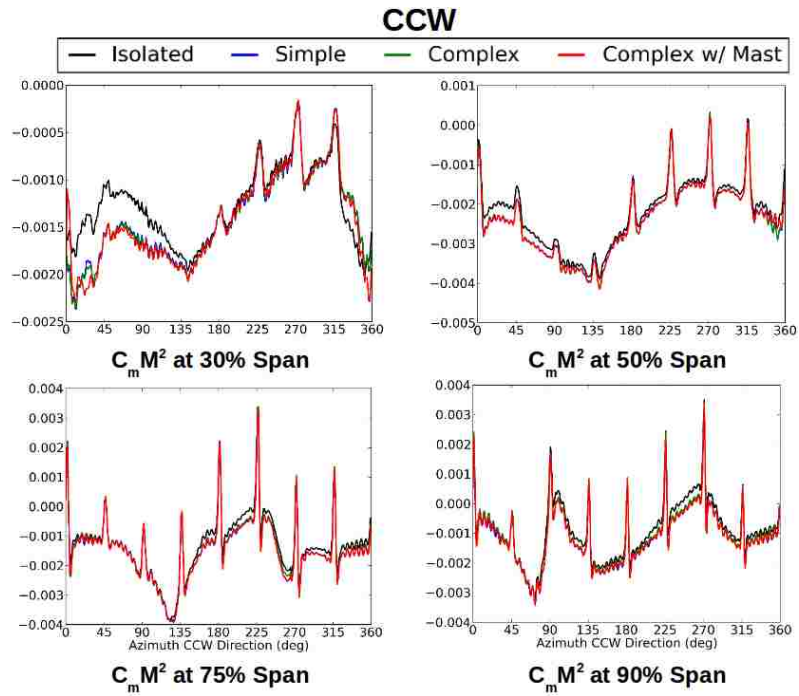
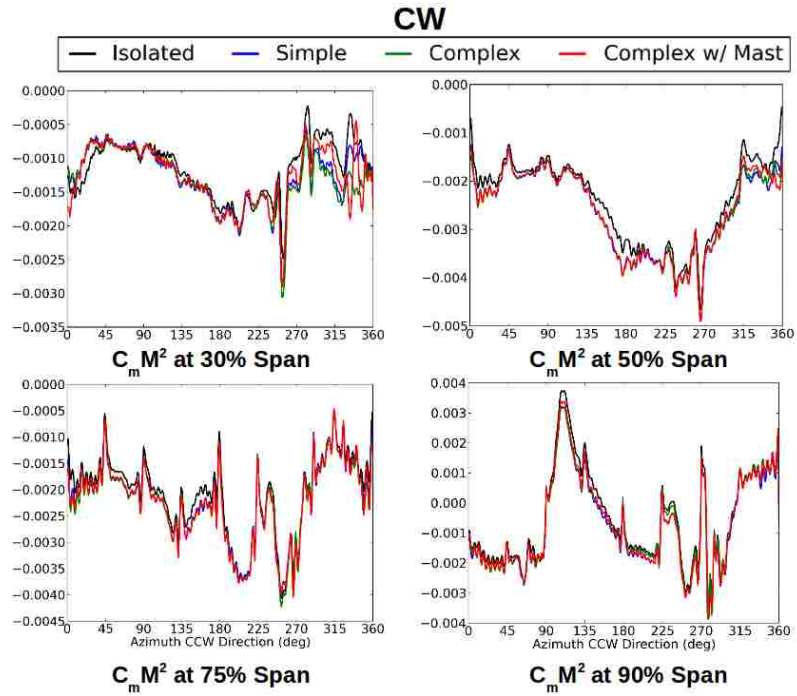


Figure 5.2: Line plots of  $C_n M^2$  between isolated coaxial rotor and rotor + fuselage cases at 55 knots



(a) Upper Rotor



(b) Lower Rotor

Figure 5.3: Line plots of  $C_m M^2$  between isolated coaxial rotor and rotor + fuselage cases at 55 knots

### 5.3 150 Knots Comparison

While there was some slight variation in rotor airloads between the rotor + fuselage cases and the isolated coaxial rotor case at 55 knots, it was not as much as anticipated. These cases were then re run for a forward flight speed of 150 knots. This was done to see changes in rotor-fuselage interactional aerodynamics with increasing forward flight speed. A comparison of the three fuselage models and isolated coaxial rotor system CFD-CSD coupling rotor controls and fuselage attitude at 150 knots is shown in Table 5.3 for comparison to predictions with the three included fuselage models..

<b>150 Knots</b>	<b>Isolated</b>	<b>Simple</b>	<b>Complex</b>	<b>Complex w/ Mast</b>
<b>Collective <math>\theta_0</math> (deg)</b>	5.94 (CCW)	5.86 (CCW)	5.86 (CCW)	5.93 (CCW)
	6.08 (CW)	6.21 (CW)	6.20 (CW)	6.23 (CW)
<b>Cyclic <math>\theta_{1C}</math> (deg)</b>	2.82 (CCW)	0.96 (CCW)	0.95 (CCW)	0.99 (CCW)
	2.82 (CW)	0.96 (CW)	0.95 (CW)	0.99 (CW)
<b>Cyclic <math>\theta_{1S}</math> (deg)</b>	-5.90 (CCW)	-5.84 (CCW)	-5.90 (CCW)	-5.88 (CCW)
	5.93 (CW)	6.08 (CW)	6.06 (CW)	6.08 (CW)
<b>Fuselage Pitch (deg)</b>	2.10	2.10	2.10	2.07

Table 5.3: Comparison of trim controls between isolated coaxial rotor and rotor + fuselage cases at 150 knots

The fuselage pitch attitude remains nearly constant between the isolated coaxial rotor case and all three rotor + fuselage cases, an observation also noticed at 55 knots. The cyclic  $\theta_{1C}$  decreases by more than half from the isolated coaxial rotor

case for all three fuselage cases. This is contrast to what was seen at 55 knots. The differential cyclic  $\theta_{1S}$  however remains fairly steady.

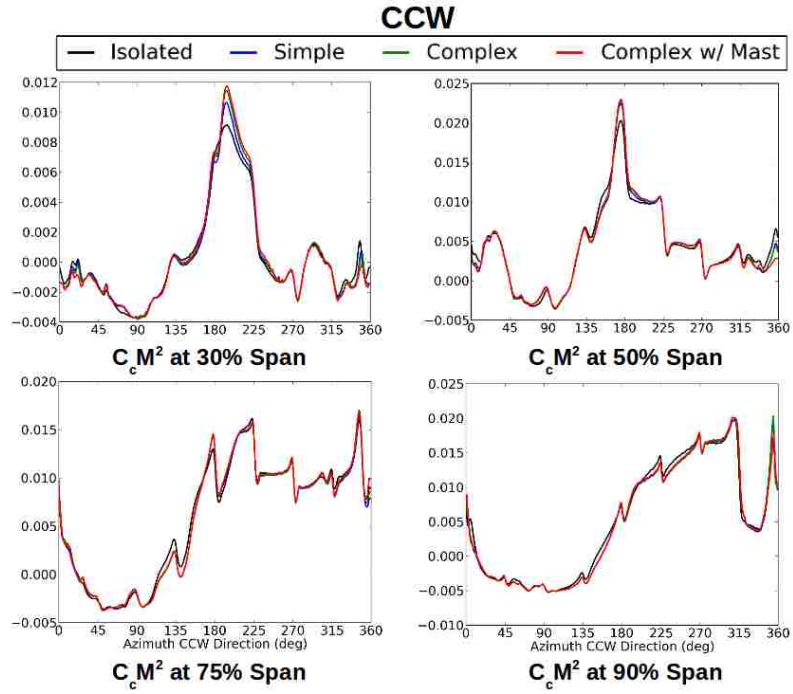
Looking at the predicted integrated quantities between the three rotor + fuselage cases and the isolated coaxial rotor case there is not much difference in thrust or power. In all 4 cases, the lower rotor produces slightly more thrust than the upper rotor. The deviation in total rotor power and total rotor thrust is less than 6% between all four cases. This means that all three fuselage models exhibit nearly identical behaviour to that of the isolated coaxial rotor system for integrated quantities and rotor performance metrics. This information is summarized in Table 5.4.

<b>150 Knots</b>	<b>Isolated</b>	<b>Simple</b>	<b>Complex</b>	<b>Complex w/ Mast</b>
<b>Thrust Upper Rotor (lbs)</b>	2448.8	2462.5	2462.0	2487.0
<b>Thrust Lower Rotor (lbs)</b>	2571.5	2650.3	2653.9	2648.4
<b>Total Thrust (lbs)</b>	5020.3	5112.8	5115.9	5135.4
<b>Total Power (hp)</b>	122.5	116.2	115.2	117.2

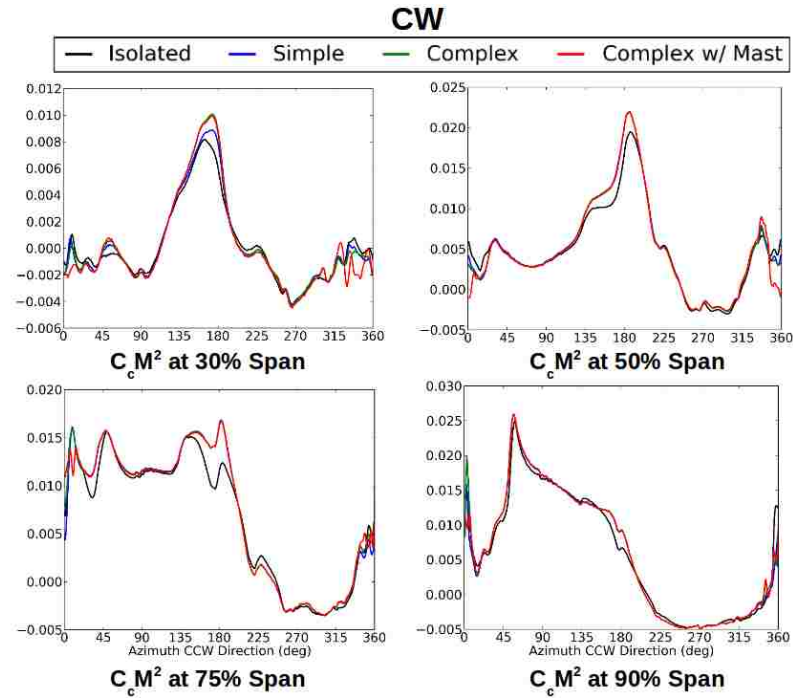
Table 5.4: Comparison of integrated quantities between isolated coaxial rotor and rotor + fuselage cases at 150 knots

Figures, 5.4, 5.5, and 5.6 compare deformed frame time histories of forces and moments ( $C_c M^2$ ,  $C_n M^2$ ,  $C_m M^2$ ) at radial stations of 30, 50, 75, and 90 percent span between the three rotor + fuselage cases and the isolated coaxial rotor case for both the upper rotor (CCW) and the lower rotor (CW) at 150 knots. Compared to 55 knots, the 150 knots fuselage cases see larger deviation from the isolated coaxial rotor case over the nose and tail sections of the rotor disks. Also similar to what was

observed at 55 knots, the pitching moments are slightly reduced on all three rotor + fuselage runs. The normal force for both the upper and lower rotors increases over the nose for all three rotor + fuselage cases. The difference between the complex and complex with mast fuselage cases compared to the isolated coaxial rotor case and simple fuselage case are most prominent only on the inboard sections (30% span).



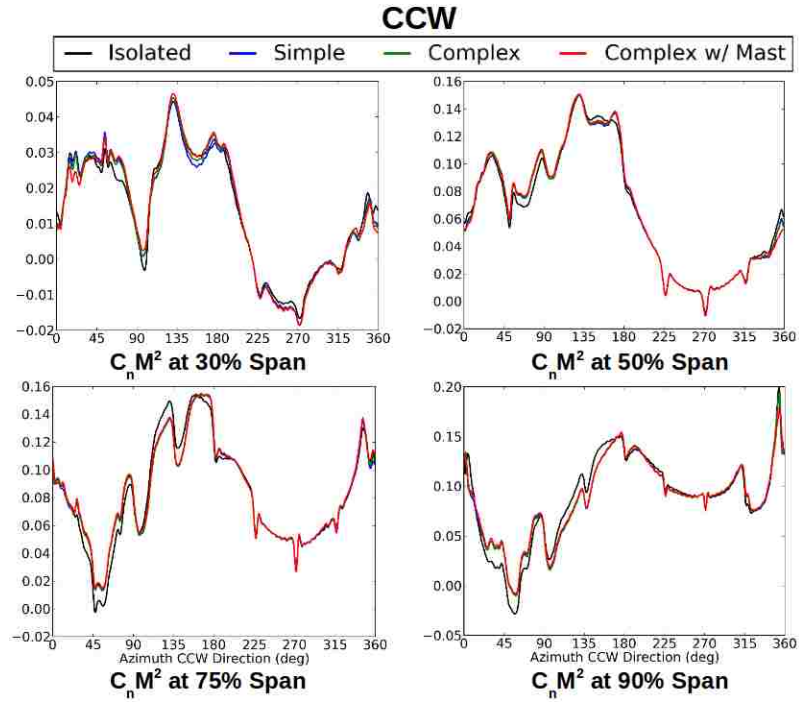
(a) Upper Rotor



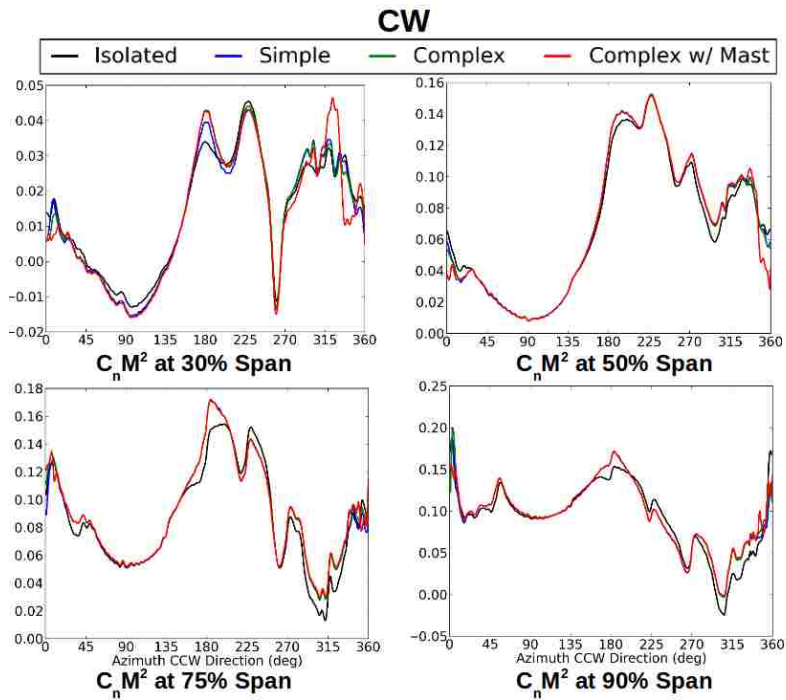
(b) Lower Rotor

Figure 5.4: Line plots of  $C_c M^2$  between isolated coaxial rotor and rotor + fuselage cases at 150 knots



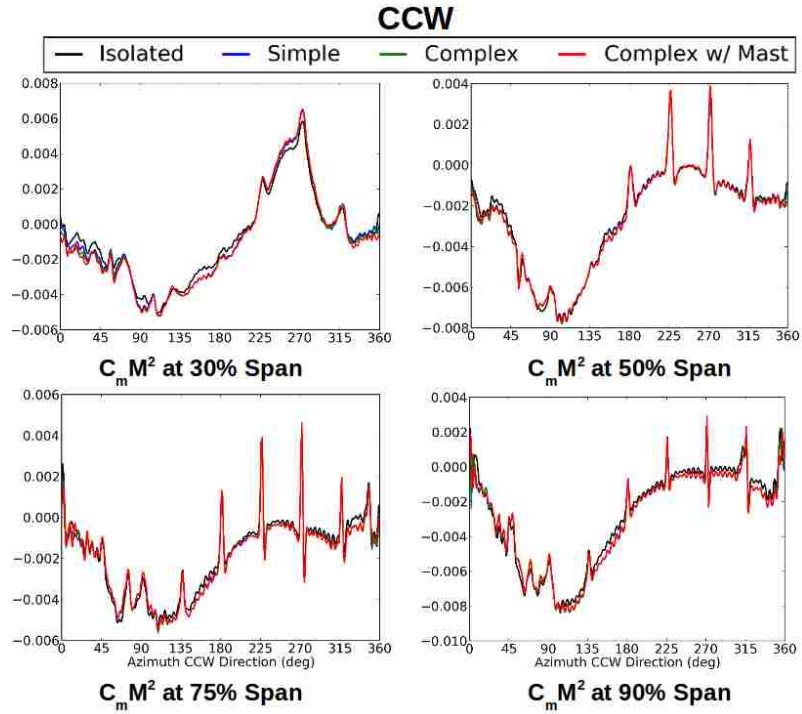


(a) Upper Rotor

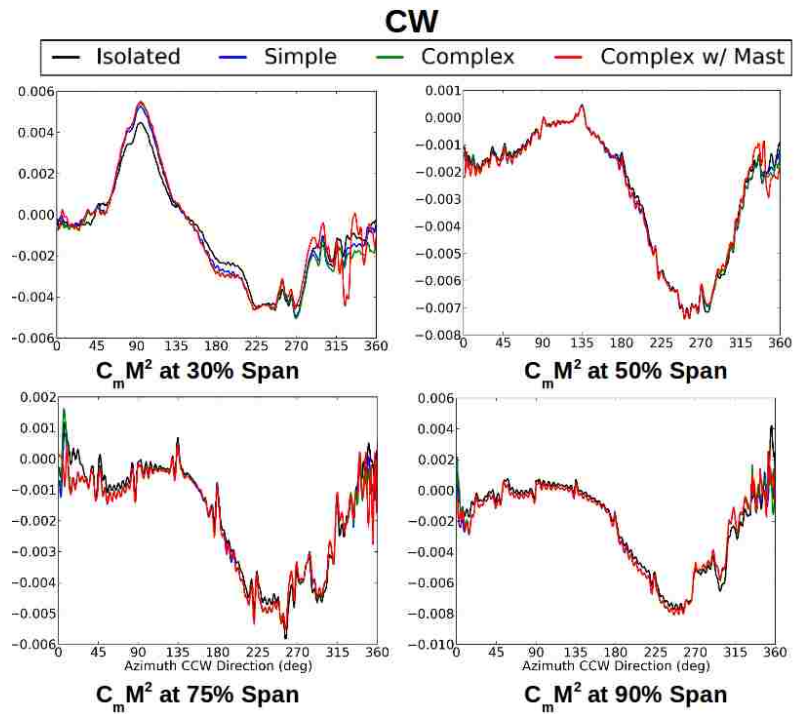


(b) Lower Rotor

Figure 5.5: Line plots of  $C_n M^2$  between isolated coaxial rotor and rotor + fuselage cases at 150 knots



(a) Upper Rotor



(b) Lower Rotor

Figure 5.6: Line plots of  $C_m M^2$  between isolated coaxial rotor and rotor + fuselage cases at 150 knots

## Chapter 6: Conclusion

### 6.1 Summary

This thesis presented the application of a CFD-CSD coupling framework for a notional X2 coaxial helicopter model to quantify interactional aerodynamics; specifically focusing on rotor-rotor and rotor-fuselage interactions at various forward flight speeds.

The first chapter went through previous work on the ABC rotor design of compound coaxial vehicles detailing design, flight test, and comprehensive analysis results. This chapter highlighted specifically the first USA compound coaxial helicopter, the XH-59A, and the design lessons Sikorsky learned from this proof of concept aircraft. The ABC methodology was revisited with the X2TD in the early 2000's, again by Sikorsky, and this modern compound coaxial configuration formed the basis for the notional model studied in this thesis. The design considerations, flight test lessons, and engineering objectives of these previous aircraft was heavily incorporated into building a notional compound coaxial helicopter design.

The second chapter highlights in detail the computational methodology and strategy this work used to evaluate interactional aerodynamics and blade airloads of a notional X2 vehicle. The well proven method of loose CFD-CSD coupling was

applied to this vehicle for three forward flight speeds of 55, 100, and 150 knots. The in house CSD solver, PRASADUM, was used with free wake and 2D aerodynamic look up tables for a baseline solution. The blade deflections and vehicle attitude were then sent to CFD which would run for 2 rotor revolutions before sending back blade sectional airloads. This coupling process was completed until a fully converged trim solution was obtained. This occurred over 4 coupling cycles or a total of 8 rotor revolutions. The details of the CSD solver and chosen reduced order aerodynamic methods coupled with it were highlighted in this section of the thesis. For CFD, the CREATE-AV Helios framework was used. This framework used OVERFLOW as a near-body solver for the structured blade grids and NSU3D as a near-body solver for the fuselage meshes in the rotor + fuselage cases. the off-body solver was SAMARC for all cases. The numerical methods, approximations, and options used in the CFD solvers are explained in detail in this chapter.

The third chapter details the construction of the notional X2 model in both the CSD and CFD solvers. The notional X2 model was built off of publicly available knowledge of the X2TD flight test program, combined with prudent engineering assumptions about the vehicle when no data was provided. The construction of the main rotor blade geometry, airfoil cross section selection, and 2D aerodynamic look up tables for the CSD solver are detailed. The structural properties of the notional X2 model were derived off of the XH-59A blade properties and scaled to match the X2TD blade frequencies. The initial benchmark of the CSD solver against flight test data and a CAMRAD II model is shown. The predicted results show excellent agreement of the notional X2 model with flight test data for integrated rotor power

and propeller power.

The fourth chapter contains the predicted isolated coaxial rotor system forward flight results for three forward flight speeds: 55, 100 , and 150 knots. Iterative convergence of rotor controls and aerodynamic blade loads were shown for the CFD-CSD coupling process. A comparison between initial CSD predictions with free wake and the final CFD-CSD coupling solution predictions were conducted to quantify what CFD brings to the analysis and where reduced order models might become grossly inaccurate. Lastly, to understand rotor-rotor interference, at 55 and 150 knots, isolated rotor cases were conducted for an isolated upper and isolated lower rotor. The single rotor cases maintained the same blade deflections and rotor controls as the coaxial rotor case. By doing this, and running the rotors in isolation, a comparison between the isolated rotor predictions and the baseline coaxial rotor system predictions could be obtained to see the rotor-rotor interactional aerodynamics effects on blade airloads.

Lastly, the fifth chapter conducted a fuselage model comparison study at 55 and 150 knots to assess rotor-fuselage interactional aerodynamics. Three fuselage models were tested with the coaxial rotor system at these flight speeds: a simple fuselage, complex fuselage containing lower rotor hub fairing and empennage, and finally a complex fuselage that included the rotor mast between the upper and lower rotors. The fuselage cases were then compared to the baseline isolated coaxial rotor system cases seen in chapter 4. Rotor-Fuselage trends were observed both with forward flight speed as well as with increasing complexity of fuselage modeling.

## 6.2 Observations

This section lists the key observations and conclusions from the isolated coaxial rotor cases as well as the rotor + fuselage cases. This section is broken up into 4 key sections: Coupling methodology and solution obtainment, CSD with free wake vs CFD, Rotor-rotor interactions, Rotor-fuselage interactions.

### **Coupling methodology and obtaining solutions**

- Coupling CFD and CSD every rotor revolution was not sufficient to dampen out the convergence transients. To convect the shed wake effects associated with abrupt deflection changes across iterations, two CFD revolutions are necessary to guarantee convergence.
- Propeller thrust and horizontal tail incidence angle play a key role in determining the vehicle and rotor trim condition. Estimation errors for these parameters may be responsible for the over prediction of power at 150 knots. Further sensitivity studies or experimental measurements are needed to resolve this discrepancy, since certain design parameters were assumed due to lack of data availability.

### **CSD with free wake vs CFD**

- Chordwise force predictions from 2D tables and free wake show excellent agreement with the 3D CFD solution on the outboard sections. This force component is dominated by viscous contributions. On the inboard stations, 2D

tables do not predict the 3D solution exactly, especially over the nose and tail. This selective correlation between the aerodynamic models at specific combinations of spanwise and azimuthal locations is indicative of spanwise flow contributions to airfoil drag.

- For pitching moments, the 2D tables predict low-frequency content well, but completely miss the impulsive 8/rev content at the blade passage frequency. CFD captures the impulsive 8/rev normal force and pitching moment, strongest on the advancing side of the lower rotor. For the present rotor, the pitching moment is expected to not excite significant elastic torsion response. For future rotors with lightweight blades, these loads may play crucial roles in the design of structurally efficient pitch control systems.
- CFD and free wake methods predict similar azimuthal variations of normal force for the inboard location (30%) on both rotors. At the outboard station (85% span), the largest discrepancies occur over the rear of the disk (315 deg to 45 deg) where the wake passes in close proximity to both tip-path-planes.
- CFD provides more realistic resolution of rotor loads in the reverse flow region. This part of the rotor disk is characterized by significant unsteadiness and flow reversals, where the assumptions used to construct reduced order unsteady aerodynamic models break down.
- While free wake solutions obtain estimates of the same order of magnitude for the 4P and 8P vibratory loads, prediction errors relative to CFD-coupled

solutions are significant for the cases investigated. Accurate vibratory load predictions tend to require the use of high fidelity aerodynamic models, while free wake methods may only provide accurate performance estimates.

### **Rotor-rotor interactions**

- Inter-rotor interference effects may be divided into two distinct time scales.
- Low frequency effects, of interest to flight dynamics, diminish with increasing advance ratio as the wake is convected away from the rotors.
- High frequency effects, (impulsive 8/rev airloads corresponding to blade passage) of interest to vibrations persist even at  $\mu = 0.41$ .

### **Rotor-fuselage interactions**

- Rotor-fuselage interference was observed at both low and moderately high speed.
- Rotor + fuselage model cases had very little blade aerodynamic loading differences compared to the isolated coaxial rotor run for both flight conditions over the vast majority of the rotor disks.
- Rotor + fuselage model cases only had slight magnitude variation of rotor blade aerodynamic loads which occurred when crossing over the nose and tail of the aircraft. These became more pronounced at higher advance ratio.



- Rotor + fuselage model cases maintained nearly identical rotor thrust sharing and total integrated rotor thrust and power predictions as the isolated coaxial rotor run and was always within 6% for both flight speeds.
- Rotor + fuselage model cases saw a slight change in rotor controls and these controls changed differently between the two flight speeds evaluated; however, in both cases these had no major effect on sectional aerodynamic loads or performance metrics.
- The comparisons between the simple fuselage shape and the complex fuselage had very little differences and the only real major component that caused a change in rotor airloads was the inclusion of the rotor mast between the rotor hubs. In terms of rotor airloads and integrated quantities, increasing complexity of the fuselage was found to have little to no effect over more than 95% of the rotor disk.

### 6.3 Contributions

With the Future Vertical Lift and Joint Multi-Role VTOL programs performance and range requirements for next generation helicopters exceeding the capability of conventional helicopter designs, there has been a renewed interest by industry, government, and academia into the compound coaxial configuration. Advanced rotorcraft designs are required to simultaneously demonstrate VTOL capabilities and cruise at speeds in excess of 220 knots. The aerodynamic environment of these types of vehicles is very complex and little to no work has been conducted evaluating the

interactional aerodynamics of such vehicles. Being able to quantify and accurately predict blade aerodynamic loads of these designs before flight testing is a critical step in breaking the classic and often costly fly-fix-fly cycle that has plagued previous generation aircraft.

The creation of a standardized public domain and open source compound coaxial configuration is a major contribution to the rotorcraft field. It provides a singular baseline to use for future validation and prediction capabilities for next generation rotorcraft using the compound coaxial design principals. Design principals, analysis, and numerical methods can all be tested on a common architecture for true benchmark comparisons of improvement in performance, fidelity, and prediction. The second major contribution of this work is establishing a loose CFD-CSD coupled framework for compound coaxial vehicles. This has never been published before in the public domain. The ability to use high fidelity CFD-CSD for complex future rotorcraft configurations with the same order of runtime as conventional helicopter models will greatly aid the design process. The XH-59A and X2TD were designed without using these high fidelity tools and did not account for interactional aerodynamics. Being able to incorporate this into the preliminary design stage can save both time and money for future flight programs.

Lastly, the wealth of data and analysis from the forward flight CFD-CSD coupling cases presented in this thesis provides great insight into the complex aerodynamic environment of these kinds of vehicles. It is the only work of its kind in the public domain and distinctly is able to quantify key aspects of rotor-rotor interference and rotor-fuselage interference which can be used as aids during the design

process and vehicle layout/configuration stage.

## 6.4 Recommendations

The body of this work dealt with rotor-rotor interactions and rotor-fuselage interactions at low and moderate speed. A natural progression of this work is to continue to apply this for faster flight conditions that lie outside the conventional helicopters flight regime, namely at 200, 220, and 250 knots. Aside from examining faster forward flight speeds, this study currently omits the auxiliary propeller from the CFD analysis. This is another major area of improvement. A list of various improvements and future studies to be conducted for other researchers is itemized below:

### **Improvements in Modeling**

- Improvements in the reduced order aerodynamic models in the CSD solver are needed to simulate the rotor-rotor interactions of coaxial main rotors as currently the models completely miss the  $8/\text{rev}$  signal.
- As higher advance ratios are achieved, corrections may need to be made to the reduced order aerodynamic models in the CSD solver to ensure convergence in the CFD-CSD coupling process.
- Likewise, improvements in modeling the reverse flow region for the reduced order aerodynamic models in the CSD solver will insure better convergence in CFD-CSD coupling as well as higher fidelity initial solutions sent to CFD.

- Currently only the main rotor blade aerodynamic tables are updated with CFD. Since the fuselage is modeled in the CFD, updating the aerodynamic tables for the fuselage and empennage can also be conducted. This has the potential to have a significant impact on the trim solution.
- Addition of a auxilliary propeller model into the CFD solution. Since the propeller spins at a much faster rpm relative to the main rotor, fully incorporating propeller blades into the CFD will cause a massive increase in computational cost. However doing so will enable the ability to quantify rotor-propeller, and fuselage-propeller interactions which are hypothesized to be more critical than rotor-rotor and rotor-fuselage interactions, especially at high speeds.
- In the CFD solution, adaptive mesh refinement was turned off for the background grids. Enabling this feature may lead to better resolution of the blade airloads and will certainly increase visualization of the rotor wake.

### **Future Flight Studies**

- Re running low and moderate speed flight cases with a CFD auxilliary propeller model included could change blade airloads prediction and allow for quantification of the full configuration.
- Running higher advance ratio flight cases beyond  $\mu = 0.41$  into the cruise regime of FVL and JMR designs will be necessary to evaluate the abilities of compound coaxial helicopters in this new flight envelope. The effects of fuselage-rotor interactions may be different. Also, with increasing forward

speed, the rotor lift offset will increase and the rotor rpm will decrease which can also cause changes in blade airloads , structural responses, and interactional aerodynamics.

- Parametric studies can be conducted and comparisons against the baseline configuration tested. This could be anything from changing the thrust sharing of the auxiliary propeller to changing the rotor spacing, lift offset control, or rotor shaft tilt for optimization and improvements in blade airloads or performance metrics.
- Using the current blade loads data, acoustic studies could be conducted to examine the acoustic signature of compound coaxial helicopters at various flight conditions. Further, the variation in acoustic signature based upon what components are included or not included in the aircraft simulation can be determined.

## Bibliography

- [1] Amiraux, M., “Numerical Simulation and Validation of Helicopter Blade-Vortex Interaction Using Coupled CFD/CSD and Three Levels of Aerodynamic Modeling,” Ph.D. Dissertation, Department of Aerospace Engineering, University of Maryland at College Park, 2014.
- [2] Ananthan, S., “Analysis of Rotor Wake Aerodynamics during Maneuvering Flight using a Free-Vortex Wake Methodology”, Ph.D. Dissertation, Department of Aerospace Engineering, University of Maryland at College Park, 2006.
- [3] Anderson Jr., John “Fundamentals of Aerodynamics,” Fifth Edition. McGraw-Hill publishing, 2011.
- [4] Bagai, A., “Aerodynamic Design of the X2 Technology Demonstrator™ Main Rotor Blade,” Presented at the 64th Annual Forum of the American Helicopter Society, International, Montreal Canada, April 29-May 1, 2008.
- [5] Blackwell, R., Millott, T., “Dynamics Design Characteristics of the Sikorsky X2 Technology™ Demonstrator Aircraft ,” Presented at the 64th Annual Forum of the American Helicopter Society, International, Montreal Canada, April 29-May 1, 2008.
- [6] Buning, P.G., et al., “OVERFLOW User’s Manual, Version 1.8,” NASA Langley Research Center, 1998.
- [7] Burgess, R. K., “Development of the ABC rotor,” Proceedings of the 27th American Helicopter Society Forum, Washington, D.C., May 1971.
- [8] Cheney, Jr., M.C., “The ABC Helicopter,” AIAA/AHS VTOL Research Design, and Operations Meeting, AIAA Paper 69-127, Georgia Institute of Technology, Atlanta, GA, February 17-12, 1969.

- [9] Coleman, T.P., "A Survey of Theoretical and Experimental Coaxial Rotor Aerodynamic Research," NASA TP-3675, National Aeronautics and Space Administration, Ames Research Center, Moffett Field, CA, March, 1997.
- [10] Datta, A., Sitaraman, J., Baeder, J., Chopra, I., "Analysis Refinements For Prediction of Rotor Vibratory Loads in High-Speed Forward Flight," American Helicopter Society 60th Annual Forum, Baltimore, MD 2004.
- [11] Govindarajan, B., and Leishman, J. G., "Predictions of Rotor and Rotor/Airframe Configurational Effects on Brownout Dust Clouds," Proceedings of the 70th American Helicopter Society, Montreal, Quebec, May 20-22, 2014.
- [12] Hirsch, C., "Numerical Computation Of Internal And External Flows," Volumes 1 and 2, Wiley Publishers, 1988.
- [13] Hornung, R. D., and S. R. Kohn, "Managing Application Complexity in the SAMRAI object-oriented framework," *Concurrency and Computation: Practise and Experience*, Vol. 14, 2002, pp. 347-368
- [14] J. Alfred, "Rotorcraft Brownout Mitigation through Flight Path Optimization using a High-Fidelity Rotorcraft Simulation Model," Masters Thesis, Department of Aerospace Engineering, University of Maryland at College Park, 2012.
- [15] Johnson, W. "CAMRAD II, Comprehensive Analytical Model of Rotorcraft Aerodynamics and Dynamics." Johnson Aeronautics, 1992.
- [16] Johnson W., "Lift-Offset Compound Design Background, X2TD, JMR ME1A Status and Plans," Presentation at Aeromechanics Branch of NASA Ames Research Center. August 2011.
- [17] Kim, H.W., Kenyon, A.R., Brown, R.E, Duraisamy, K., "Interactional Aerodynamics And Acoustics Of A Hingeless Coaxial Helicopter With An Auxiliary Propeller In Forward Flight," *The Aeronautical Journal*, Volume 113, No. 1140, February 2009.
- [18] Lakshminarayan, V.K., Baeder, J., "High Resolution Computational Investigation Of Trimmed Coaxial Rotor Aerodynamics in Hover," Presented at the 64th Annual Forum of the American Helicopter Society, International, Montreal, Canada, April 29-May 1, 2008.
- [19] M. J. Bhagwat, "Mathematical Modeling of the Transient Dynamics of Helicopter Rotor Wakes Using a Time-Accurate Free-Vortex Method," PhD Thesis, Department of Aerospace Engineering, University of Maryland at College Park, 2001.

- [20] Mavriplis, D.J., "NSU3D (Version 3.4)," Scientific Simulations, Yorktown, VA 23692.
- [21] Norman, T. R., Shinoda, P. M., Peterson, R. L., and Datta, A., "Full-scale Wind Tunnel Test of the UH-60A Airloads Rotor," American Helicopter Society 67th Annual Forum, Virginia Beach, VA, May 3-5, 2011.
- [22] Paglino, V. M., "Forward flight performance of a coaxial rigid rotor," Proceedings of the 27th American Helicopter Society Forum, Washington, D.C., May 1971.
- [23] Potsdam, M., Yeo H., and Johnson W., "Rotor Airloads Prediction using Loose Aerodynamic/Structural Coupling," American Helicopter Society 60th Annual Forum Proceedings, Baltimore, MD 2004.
- [24] Pulliam, T. H., "Euler and Thin-Layer Navier-Stokes Codes: ARC2D, and ARC3D," Computational Fluid Dynamics Users Workshop, The University of Tennessee Space Institute, Tullahoma TN, March 1984.
- [25] Roger Strawn, "High-Performance Computing for Rotorcraft Modeling and Simulation," *Computing in Science and Engineering*, vol.12, no. 5, pp. 27-35, September/October 2010, doi 10.1109/MCSE.2010.110.
- [26] Ruddell, A. J., "Advancing Blade Concept (ABC) Development," Proceedings of the 32nd Annual National Forum of the American Helicopter Society , Washington, D.C., May 1976.
- [27] Schmaus, J.H. and Chopra, I., "Aeromechanics for a High Advance Ratio Coaxial Helicopter", 71<sup>st</sup> Annual Forum of the American Helicopter Society International, Virginia Beach, VA, May 5-7 2015.
- [28] Sitaraman, J., Baeder, J., and Chopra, I., "Validation of UH-60 Rotor Blade Aerodynamic Characteristics Using CFD," Presented at the 59th Annual Forum of the American Helicopter Society International, Phoenix, AZ, USA, May 2003.
- [29] Spalart, P. R., and S. R. Allmaras, "A One-equation Turbulence Model for Aerodynamic Flows," *La Recherche Aerospatiale*, Vol. 1, 1994, pp. 521.
- [30] Sridharan, A., "Simulation Modeling of Flight Dynamics, Control and Trajectory Optimization of Rotorcraft Towing Submerged Loads," Ph.D. Dissertation, Department of Aerospace Engineering, University of Maryland at College Park, 2014.



- [31] Venkateswaran Sankaran, Jayanarayanan Sitaraman, Andrew Wissink, Anubhav Datta, Buvana Jayaraman, Mark Postdam, Dimitri Mavriplis, Zhi Yang, David O'Brien, Hossein Saberi, Rui Cheng, Nathan Hariharan and Roger Strawn, "Application of the Helios Computational Platform to Rotorcraft Flowfields," AIAA- 2010-1230, 48th AIAA Aerospace Science Meeting, Orlando FL, Jan 2010.
- [32] Walsh, D., Weiner, S., Arifian, K., Lawrence, T., Wilson, M., Millott, W. and Blackwell, R., "High Airspeed Testing of the Sikorsky X2 Technology™ Demonstrator," American Helicopter Society 67th Annual Forum, Virginia Beach, VA, May 2011.
- [33] Walsh, D., Weiner, S., Arifian, K., Bagai, A., Lawrence, T., and Blackwell, R., "Development Testing of the Sikorsky X2 Technology™ Demonstrator," American Helicopter Society 65th Annual Forum, Grapevine TX, May 2009.
- [34] Wissink, A., Sitaraman, J., Sankaran, V., Mavriplis, D., Pulliam, T., "A Multi-Code Python-Based Infrastructure for Overset CFD with Adaptive Cartesian Grids," Presented at AIAA 2008.
- [35] Wissink, A. M., R. D. Hornung, S. Kohn, S. Smith, and N. Elliott, "Large-Scale Parallel Structured AMR Calculations using the SAMRAI Framework," Proceedings of Supercomputing 2001 (SC01), Denver CO, Nov 2001.
- [36] Yeo, H. and Johnson, W., "Investigation of Maximum Blade Loading Capability of Lift-Offset Rotors," American Helicopter Society 69th Annual National Forum, Phoenix, AZ, May 21-23, 2013.